Fabrication of high aspect ratio (HAR) atomic force microscopy (AFM) probes by one step e-beam lithography and AFM cantilever patterning using grafted monolayer brushes

by

Ferhat Aydinoglu

A thesis
presented to the University of Waterloo
in fulfillment of the
thesis requirement for the degree of
Doctor of Philosophy
in
Electrical and Computer Engineering (Nanotechnology)

Waterloo, Ontario, Canada, 2018

Examining Committee Membership

The following served on the Examining Committee for this thesis. The decision of the Examining Committee is by majority vote.

Supervisor	Bo Cui Associate Professor, Electrical and Computer Engineering, University of Waterloo
Internal Member	Karim Karim Professor, Electrical and Computer Engineering, University of Waterloo
Internal Member	Guo-Xing Miao Assistant Professor, Electrical and Computer Engineering, University of Waterloo
Internal-external Member	Zhongwei Chen Professor, Chemical Engineering, University of Waterloo
External Examiner	Xiaogan Liang Assistant Professor, Mechanical Engineering, University of Michigan

Author's Declaration

I hereby declare that I am the sole author of this thesis. This is a true copy of the thesis, including any required final revisions, as accepted by my examiners.

I understand that my thesis may be made electronically available to the public.

Statement of Contributions

A part of this thesis is based on a combination of published works. Several sections were adapted from the following list of published work, with specific reference to the published work provided within the chapter.

Chapter 4, Section 4.1.3

Ayari-Kanoun, A., Aydinoglu, F., Cui, B. and Saffih, F., 2016. Silicon nanostructures with very large negatively tapered profile by inductively coupled plasma-RIE. *Journal of Vacuum Science & Technology B, Nanotechnology and Microelectronics: Materials, Processing, Measurement, and Phenomena*, *34*(6), p.06KD01.

> This project is mainly Dr. Ayari's work, and I carried out most of the experiments with several characterizations. Dr Ayari-Kanoun performed etching, SEM imaging and wrote the manuscript. All the authors reviewed the manuscript.

Chapter 5, Section 5.11

Aydinoglu, F., Saffih, F., Dey, R.K. and Cui, B., 2017. Chromium oxide as a hard mask material better than metallic chromium. *Journal of Vacuum Science & Technology B, Nanotechnology and Microelectronics: Materials, Processing, Measurement, and Phenomena*, *35*(6), p.06GB01.

> This project is Dr. Saffih's work; he did preliminary work and left. Dr. Dey helped on experimental part, yet I worked on major part and finalized the work with additional contributions. I wrote the manuscript, and all the authors reviewed it.

Chapter 6

Aydinoglu, F., Yamada, H., Dey, R.K. and Cui, B., 2017. Grafted Polystyrene Monolayer Brush as Both Negative and Positive Tone Electron Beam Resist. *Langmuir*, *33*(20), pp.4981-4985.

> This project is mainly my work, and I carried out all the experiments and characterizations. Mr. Yamada optimized development temperature, and Dr. Rey helped in developing the recipe. I wrote the manuscript, and all the authors reviewed it.

Abstract

Atomic force microscopy (AFM) allows imaging individual atoms where a very sharp tip touches and feels the substrate. Although a regular AFM tip can achieve atomic resolution, it produces false images on substrates with tall and dense features because of the shape and dimensions of the tip. To solve this problem, high aspect ratio (HAR) AFM tips have emerged. However, the HAR AFM tips are often fabricated individually with the need for expensive instruments such as focused ion beam causing low throughput and high cost. In this thesis, several processes are developed for the batch fabrication of HAR AFM tips to reduce the cost and increase the throughput where HAR tips with tip apex diameter down to 9 nm without oxidation sharpening have been obtained by our methods.

Moreover, there are cantilever-based devices demanded in a wide range of applications such as tip-enhanced Raman spectroscopy. Our one-step e-beam lithography technique is capable of forming arbitrary patterns for a variety of applications. Alternatively, a process based on grafting polystyrene monolayer brush has been developed to pattern irregular substrates like cantilevers with e-beam lithography where both negative and positive tone behaviors are obtained under different development conditions. That is, the process enables the fabrication of both recessed and protruded features on both nonflat and very small surfaces. As a result, an AFM cantilever is patterned with high resolution on both top and sidewalls at the same time.

Acknowledgements

“Knowledge is to understand, to understand who you are.
If you know not who you are, what's the use of learning?”
− Yunus Emre

PhD stands for Doctor of Philosophy, and it is a process of carrying out advanced research in a particular subject to contribute academic community, but I believe it is a process to learn persistence, patience, devotion, and dedication. It is a great pleasure to have the opportunity to thank those who made this possible.

I am deeply indebted to my supervisor, Dr. Bo Cui, and feel very lucky to be one of his students because of his encouragement, helpful advice and valuable discussions. He is an enthusiastic and hardworking person with immense knowledge. His door is always open for anyone needs help. He gives useful advices not only for studies but also for real life. We had several trips together for conferences, and I was amazed at how friendly he was with students. I cannot find the right words to thank him for everything he has done.

I would also like to take special time to express my gratitude to group members, Dr. Celal Con, Dr. Ripon Dey, Medhat Samaan, and all others. Dr. Celal Con is my first mentor who has taught me everything in clean room with great patience. I am so grateful to him.

Many thanks to cleanroom and other lab staffs, Richard Barber, Nina Heinig, Czang-Ho Lee, and Nathan Fitzpatrick for their friendly support over the years.

A special thanks to my family. Words cannot express how grateful I am to my mother, my father, my brothers, my sisters and my wife for all the sacrifices that they have made. Their prayers were what sustained me this far.

Lastly and mostly, I thank the Almighty, for giving me the strength and patience to carry on this work and for blessing me with great people who have been my greatest supporter in both my personal and professional life.

Dedication

"… dedicated to

my beloved mother, father, brothers and sisters,

my lovely wife, Meral

and my beloved son Cevdet John …"

Table of Contents

List of Figures

List of Tables

Chapter 1

Introduction to atomic force microscopy (AFM) and its applications

This chapter provides a background for atomic force microscopy (AFM), its working principles, benefits and applications.

1.1 Background and motivation

Microscopy is one of the essential fields for research in the biological, chemical, and physical sciences. Optical, electron and scanning probe microscopy techniques are three main types of microscopy. Optical and electron microscopy techniques have already contributed significantly to scientific knowledge; however, there are still some limitations and disadvantages of these techniques. Scanning probe microscopy (SPM) emerges to overcome some of these limitations and drawbacks of these radiation-based microscopy techniques. Most common scanning probe microscopy techniques are atomic force microscopy (AFM) and scanning tunneling microscopy (STM) that provides atomic resolution which is the order of thousand times better than the optical diffraction limit of the visible light. First STM was invented by Binnig et al. in 1982[1] and is used to generate substrate topology by detecting the tunneling current between the substrate and tip apex. The substrate should be conductive for STM to be operational that leads Binning et al. to discover AFM in 1986[2] which physically touches and feels the substrate and is suitable for insulating substrates.

AFM is a functional tool that provides three-dimensional computer visualities of surfaces. It is a unique technique because it does not require electrons or light to focus to the substrate as optical and electron microscopes do. While AFM is one of the most popular scanning probe microscopy tools, scanning electron microscopy (SEM), and transmission electron microscopy (TEM) are the most common electron microscopy tools. Depending on the interest, different imaging technique can be preferred such as optical microscopy would be a better tool to analyze samples in a short time while other techniques require scanning process, vacuum environment or sample preparation. However, optical microscopy has a limited resolution of a couple of hundred nanometers. Table 1-1 compares common microscopy techniques and Fig. 1.1 shows the observation range comparison for popular microscopy techniques[3].

	AFM	SEM	TEM
Resolution	1 Å	5 nm	1 Å
Vacuum environment	Not required	Required	Required
Depth of field	Poor	Good	Good
Max. field of view	~100 µm	~5 mm	~100 nm
Cost	Low	Medium	High
Sample preparation	Easy	From easy to difficult	From easy to difficult
Sample type	Conductive/insulator	Conductive	Conductive

Table 1-1: Comparison of AFM, SEM, and TEM.

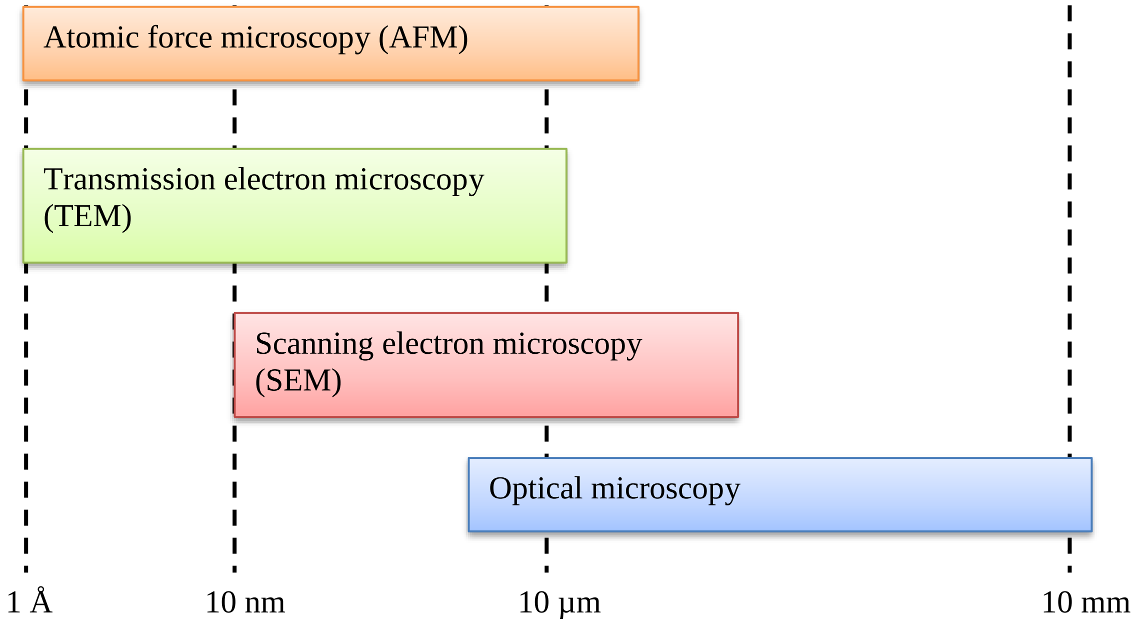

Fig. 1.1: Observation range comparison of common microscopy techniques.

SEM requires an electron beam to focus and scan the substrate to produce images where electrons interact with atoms and generate signals that are collected by detectors to produce an image on the computer. SEM requires a vacuum environment and sample preparation in some cases. For example, a thin layer of metal needs to be coated if the sample is not conductive. Depending on the substrate type, SEM could be destructive generally at high electron beam acceleration voltages, and receiving a good signal is difficult at low electron beam acceleration voltages. Moreover, SEM has a good resolution down to a few nanometers and field of view up to several millimeters. The tool is moderately expensive and commonly available in research labs.

TEM is another common electron microscopy technique that relies on transmission of a beam of electrons through a sample to form an image. In this case, the sample should be ultrathin; usually less than a hundred nanometers. Due to small de Broglie wavelength of the electrons, TEM can achieve extremely high resolution down to atomic level; a TEM image can display single atoms and atomic columns. Similarly, because of the larger wavelength of photons, optical lithography has an order of thousand worse resolution compared to TEM. Furthermore, TEM requires a vacuum environment and is an expensive tool; therefore, it is less commonly available in research labs compared to other microscopy techniques. One of the major drawbacks of TEM is that it generally requires a sample preparation because the sample needs to be very thin; the prepared sample is called lamella. The preparation is usually carried out in focused ion beam (FIB) which is also an expensive and less commonly available tool. Using accelerated ions, a lamella is milled and taken out of the sample; in other words, a part of sample is destroyed. Next, the lamella is transferred to the TEM for imaging which is a painful work compared to other microscopy techniques. Lastly, the sample should be conductive for imaging similar to SEM.

1.2 Working mechanism

An AFM setup mainly consists of a very sharp tip, a flexible cantilever, a sensitive photodetector, a laser beam, feedback control system, and a stage that can move in x-, y-, and z-axis (some cases stage is fixed, but tip scans the sample). A schematic representation of the setup is shown in Fig. 1.2. AFM cantilevers are generally made of silicon or silicon nitride, and a layer of metal (usually gold or aluminum) often needs to be coated to the backside of the cantilever to increase reflectivity to have a decent signal on the photo-detector, especially in liquid environments.

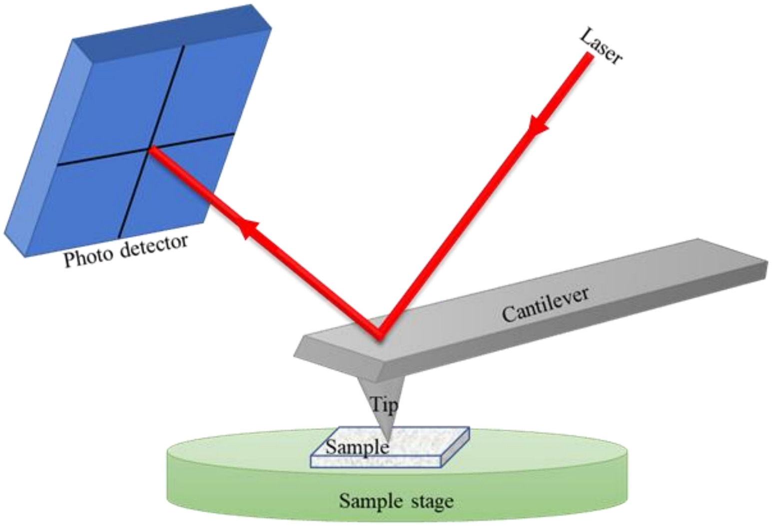

Fig. 1.2: Schematic representation of an AFM setup.

The conventional methods to detect cantilever deflections, which later will be processed to generate the image, are the optical lever method, optical interferometric method, electronic tunneling method, piezoelectric detection method, capacitive detection method, and piezoresistive detection method. The optical lever and electronic tunneling methods are the most common types of cantilever detection methods. In case of electronic tunneling, the substrate should be conductive or needs to be metal coated. The environment is also important in case of electronic tunneling; it does not work in the liquid environment, and there are other possible problems in air environment[4]. In the optical lever method, a laser beam is shone on the backside of the cantilever, and reflected beam is detected by a photo-detector which is usually a quartered photodiode that acts as a position sensor. The cantilever is mounted on a piezoelectric element to move cantilever up and down to approach sample substrate by controlling the applied voltage. Here, the movement is as precise as 1 Å. During the scanning, the cantilever will be bent at different degrees depending on irregularities on the substrate. The bending of the cantilever causes deflection in the laser beam which will be detected by photodiode. The deflections versus position information can be recorded by a feedback control system which can generate a three-dimensional image on the computer.

1.2.1 Scanning modes

An AFM usually operates as one of three modes that are contact, non-contact, and tapping modes. Depending on the need, one of the modes can be preferred to another. A schematic representation of the modes is presented in Fig. 1.3, and each mode will be discussed separately.

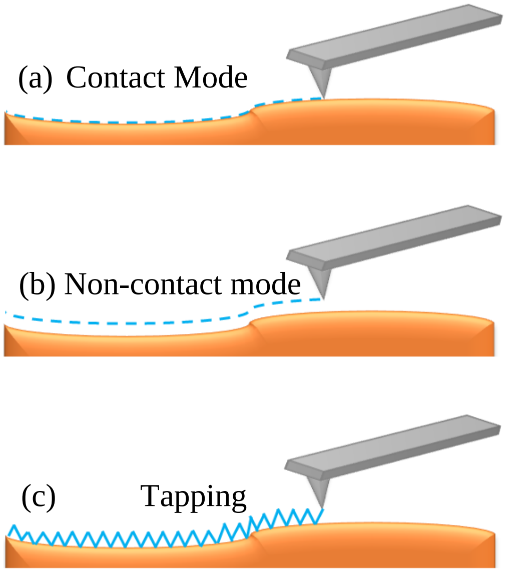

Fig. 1.3: Scanning modes of AFM.

1.2.1.1 Contact mode

In contact mode, the tip physically touches and scans the substrate while it is in contact as represented in Fig. 1.3a. Here, either deflection of the light on cantilever or force required to keep the cantilever at a constant position is collected to generate an image.

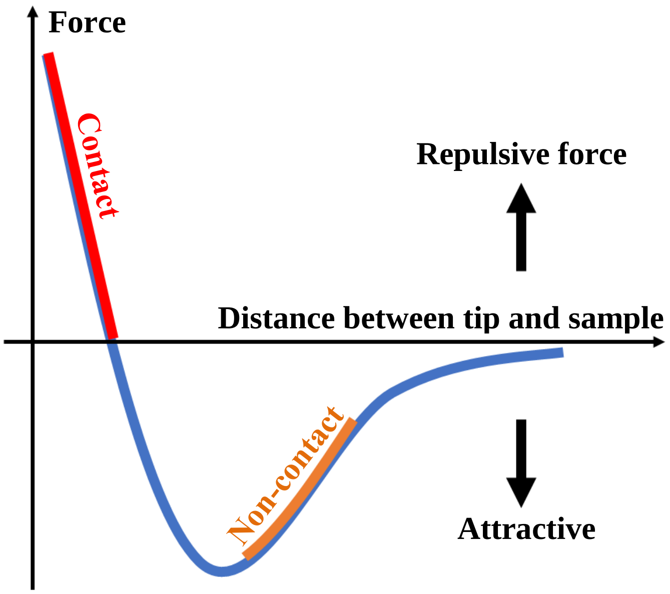

Fig. 1.4: Interatomic force versus distance between AFM tip and sample curve.

As shown in Fig.1.4, when tip approaches the sample, attractive forces are generated which will increase as tip approaches to the sample. As atoms get close enough to each other, electron clouds, start to repel each other electrostatically[5]. When the gap between the tip and the sample gets smaller, repulsive forces will dominate, and it reaches a maximum as soon as the atoms are in contact. That is why this mode is also called repulsive mode. In contact mode, the stiffness of the cantilever is very important to maintain a proper deflection for a clear image that requires cantilevers with low stiffness or spring constant. The major disadvantage of the contact mode is that it usually damages either the sample or the tip itself as it is a kind of dragging motion. Therefore, it is not recommended for polymeric or biological surfaces.

1.2.1.2 Non-contact mode

Unlike the contact mode, in the non-contact mode the tip does not physically touch the substrate. It keeps the distance about 5 to 15 nm above the sample and detects the attractive van der Waals forces[5]. The force versus distance data are collected by a feedback control system and converted in an image as shown in Fig. 1.3b. In Fig. 1.4, non-contact mode regime is highlighted on interatomic force versus distance curve; the force is generally about 10 – 12 pN. This mode is widely used for a range of different materials such as metals, semiconductors, polymers and biological materials[6] due to its non-destructive operation. In other words, the non-contact mode is advantageous since it does not harm and contaminate the sample or tip. However, in case of liquid environment or contaminant, this mode will not operate because the effective range of the van der Waals force is smaller than the thickness of the liquid where the tip may also get trapped in. Even a few nanometers of liquid may cause problems such as it will result in a false image while tip would penetrate through the liquid in contact mode.

1.2.1.3 Tapping mode

Tapping mode is the most commonly preferred mode of AFM due to its advantages. For example, it overcomes friction and adhesion issues associated with AFM, so it can be used for soft materials as it is not as harmful as contact mode. As mentioned above for non-contact mode, there is a chance of liquid contaminant on a variety of substrates that causes false images. The tapping mode was invented to resolve this issue[7] as contact mode is limited to rigid materials. Here, the cantilever is oscillated to near its resonance frequency by a piezoelectric material. The oscillation amplitude generally changes from several nanometers to 100-200 nm. At the beginning of the scanning, the oscillating cantilever is brought close to the substrate until the tip taps to the substrate. Afterwards, the tip is lifted followed by moving to a new location. This event is continuously repeated to generate an image as represented in Fig. 1.3c. The tapping frequency can be set to a desired value depending on the application, and it is in range of 50 to 500 kHz.

1.3 Applications

Due to AFM's unique advantages mentioned earlier, it is a widely used tool in a variety of areas including analyzing nano-/micro-structures, nanofabrication, electrical characterization, crack investigation, studying mechanical properties of the materials such as hardness and elasticity, surface composition analyzes, and biological applications.

It's very sharp tip and precisely controllable motion in three dimensions allows AFM to be used in nanofabrication. Under a bias, AFM can locally oxidize aluminum[8], titanium[9], and niobium[10] metal films that can be used as an etching mask for various device fabrication. Furthermore, because of its mechanical functionalities, AFM tip can penetrate in polymers which can also be used as a mask for pattern transfer. However, AFM is not practical in large-scale fabrication because of its low speed.

Chapter 2

AFM probe and standard AFM probe fabrication techniques

In this chapter different fabrication processes for manufacturing standard silicon and nitride AFM probes at both commercial and research level will be discussed.

An AFM probe is an essential part of the microscopy and consists of three main parts: tip, cantilever, and holder (also called cantilever holder). A schematic representation of the probe is shown in Fig. 2.1.

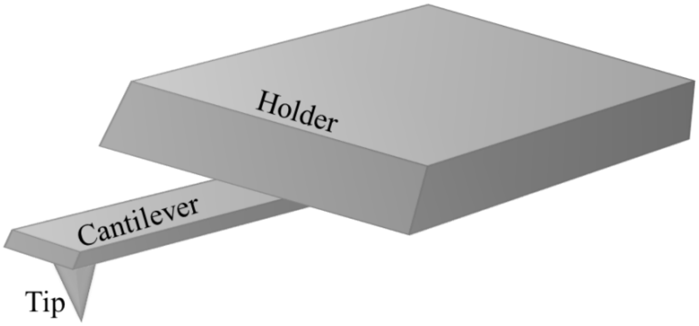

Fig. 2.1: A schematic representation of an AFM probe.

The tip is the part that touches or senses the substrate, and the tip apex should have a radius of curvature of several nanometers for high-resolution imaging. The material choice and tip dimensions are essential for durability and functionality. Moreover, the surface condition of the tip should be considered because the tip might attract contaminations on the substrate that will result in false imaging and poor resolution. A typical height for the tip is in the range of 3 to 20 µm.

The cantilever is as vital as the tip because properties of cantilever affects the whole process. Size, shape and material choice of the cantilever determines its resonant frequency and spring constant which are chosen depending on the application. The resonant frequency is mostly controlled by tuning the length and thickness of the cantilever where longer cantilever size will result in smaller resonant frequency values. Spring constant increases by increasing the thickness or decreasing the length of the cantilever. A typical cantilever is 0.5 to 8 μm thick with various shapes, and commonly, rectangular or triangle shapes are preferred.

The holder part is there for easy handling and mounting into the microscope. Depending on the application it can be functionalized, but generally, it is a large rectangular piece with cantilever attached to it. Typically size of a holder is 1.6 to 3.4 mm.[2]

Silicon is a commonly preferred material for AFM probe fabrication because of its low cost, availability, well-known characteristics, and modifiability. It can be doped to increase the conductivity or oxidized to form an insulating layer. Silicon can also be fabricated as single crystalline or polycrystalline depending on the application. If a well conductive probe is needed, it can be coated with metals like gold because probes of undoped silicon or silicon-nitride have poor electrical conductivity. Silicon nitride is an excellent insulating probe while undoped-silicon and silicon nitride probes are also frequently used for topographical characterizations. Diamond is another ideal material for AFM probe because of its durability and good electrical conductivity.

In general, AFM probes are fabricated by micro/nano processing technology on a whole wafer at a time. For example, about 400 probes can be fabricated on a 4-inch wafer and 1000 probes on a 6-inch wafer. A large number of tips are needed in research and development purposes because tips can be broken, blunt, contaminated, bent, and so on. While there are many tips required overtime, the AFM is still a cost-efficient tool compared to other methods due to high throughput fabrication of tips.

2.1 Fabrication of regular silicon AFM probes

Regular silicon AFM probes can be fabricated by micro/nano processing technology including lithography, dry or wet etching, and deposition. There are many different possible combinations of processing steps that might have a slightly less or more advantage or disadvantages over others. Here, a standard fabricating process of a commercial AFM tip[11] will be discussed, and a schematic representation of fabrication steps are shown in Fig. 2.2.

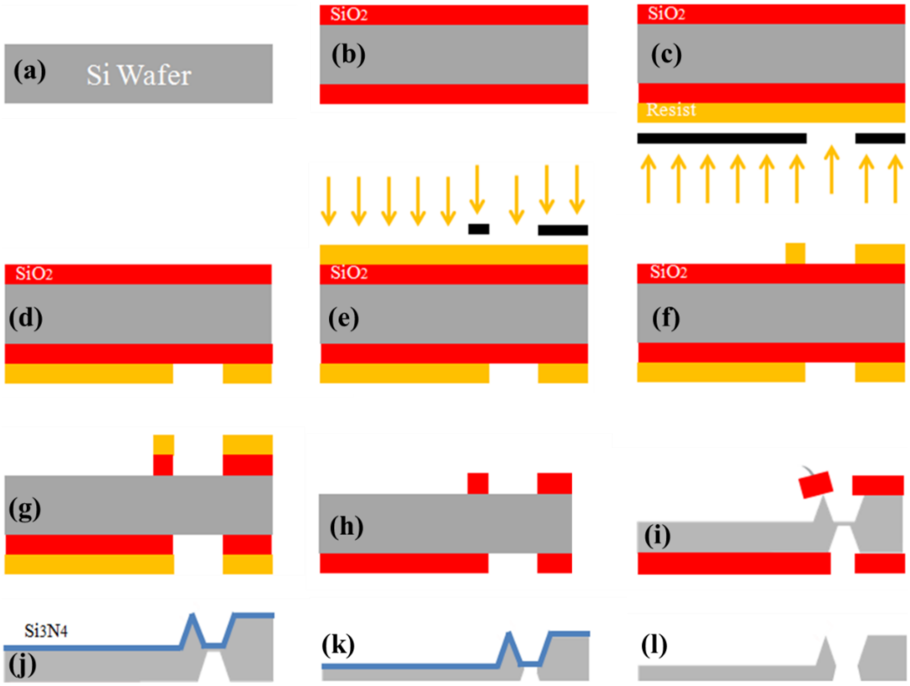

Fig. 2.2: Fabrication steps of a standard silicon AFM probe fabrication (adopted with permission from Ref. [11]).

Starting with a bare <100> silicon wafer (Fig. 2.2a), wafer cleaning processes such as solvent cleaning (acetone, isopropyl alcohol followed by deionized water rinse), oxygen (O_2) plasma treatment or RCA cleaning are generally required before high-temperature processing steps. Here, solvents and O_2 plasma treatment get rid of organic contaminations, and RCA cleaning is performed for organic contaminants removal, thin oxide layer removal, and ionic contamination removal. RCA cleaning is a solution of deionized water, ammonium hydroxide, and hydrogen peroxide which is called RCA 1, and a solution of deionized water, hydrogen chloride, and hydrogen peroxide which is called RCA 2. Next, silicon is oxidized to form etching mask layers on both sides (Fig. 2.2b). The oxide mask is usually coated thermally; however, silicon dioxide (SiO_2) can be coated by plasma-enhanced chemical vapor deposition (PECVD) tool, too. Afterward, a layer of positive photoresist is coated and baked on the backside of the wafer, followed by UV (ultraviolet) exposure through a chromium/quartz photomask (Fig. 2.2c), and the exposed photoresist is developed (Fig. 2.2d). The height of the tip is determined with this lithography step with subsequent KOH etching. Next, similar steps are applied to the front side with a different photomask pattern, yet similar spin-coating, baking, UV exposure, and development (Fig. 2.2e-f). The dimensions and shape of the cantilever is defined with the photomask pattern which is designed for target application. To transfer the photoresist pattern into the SiO_2 layer, the sample is immersed into an etching solution (generally hydrofluoric acid (HF) or buffered hydrofluoric acid (BHF) solutions). Once all the oxide is etched at unmasked areas, the sample is rinsed by deionized water to stop etching (Fig. 2.2g). After that, the photoresist is dissolved in a stripper (Fig. 2.2h); this is required because photoresist is not stable in potassium hydroxide (KOH) solution, which will be subsequently used, and photoresist can leave traces on the sample during the etching. Next, anisotropic etching of silicon is done by KOH until the oxide mask at the top of the inverse pyramid falls off (Fig. 2.2i). Here, an inverse pyramid is formed because KOH etches silicon anisotropically depending on crystalline orientation. There is a difference between etching directions due to the tetrahedron structure of the silicon. Afterward, a layer of a silicon nitride (Si_3N_4) is deposited to the front side of the wafer (Fig. 2.2j) to protect the tip from subsequent KOH etching which is performed to determine the cantilever thickness (Fig. 2.2l). Once the desired thickness is reached, the sample can be taken out of the solution and rinsed to stop the etching. Finally, remained Si_3N_4 is etched in an HF or BHF solution to finalize the fabrication. It should be noted that the holder part is not shown in the fabrication steps for simplicity.

2.2 Fabrication of regular nitride AFM probes

Similar to silicon probes, there are different ways to fabricate a nitride AFM probe. Here, fabrication process of a commercial nitride probes[11] will be introduced.

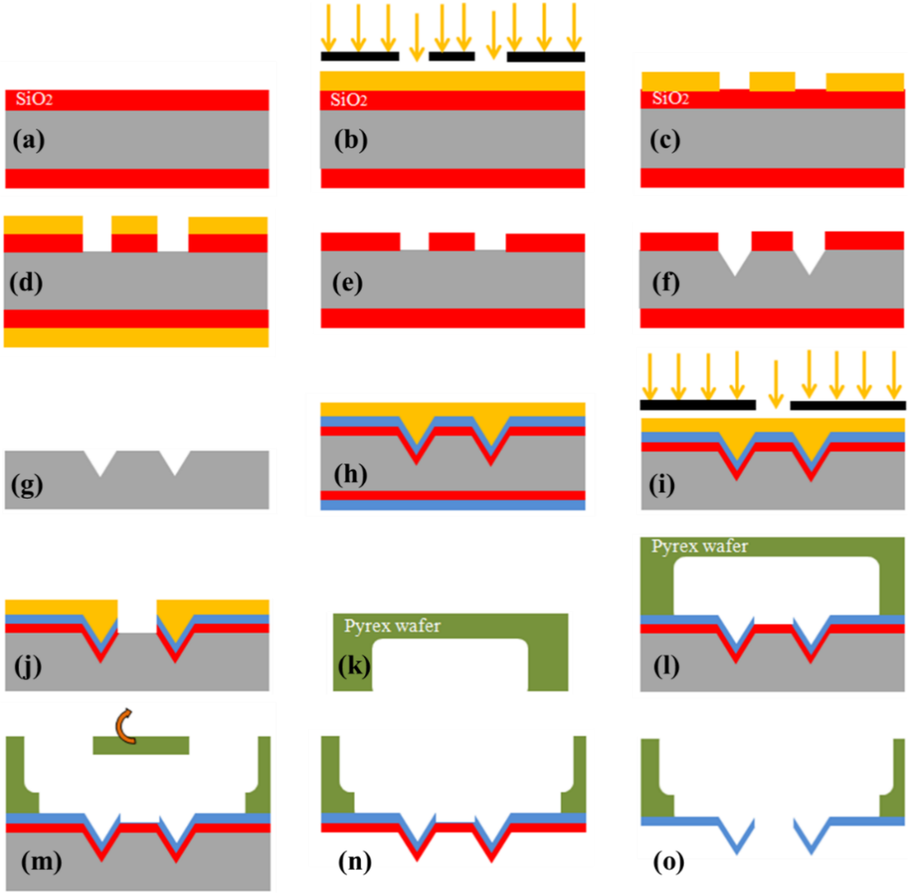

Fig. 2.3: Fabrication steps for a silicon AFM probe fabrication (adopted with permission from Ref. [11]).

The fabrication of a nitride AFM probe starts with a <100> bare silicon wafer, followed by its oxidation similar to silicon probes (Fig. 2.3a). Next, photolithography is carried out with spin-coating a photoresist, baking and exposure it (Fig. 2.3b), followed by developing the photoresist (Fig. 2.3c). The photoresist pattern will be transferred to the oxide layer which is etched by the BHF solution that will also attack the oxide layer on the backside. Therefore, a layer of protective resist is spin-coated and baked on the backside (Fig. 2.3d), and front side oxide is etched in BHF (Fig. 2.3e). After that, photoresist is stripped in acetone/isopropanol

(Fig. 2.3f), and silicon is etched in KOH solution to form inverse pyramid gap to be filled by nitride later (Fig. 2.3g). Next, the oxide layer on both sides are etched in the BHF solution (Fig. 2.3g). Afterward, the sample is oxidized again, and a layer of nitride is deposited by low-pressure chemical vapor deposition (LPCVD). Next, a layer of protective resist is coated on the front side for subsequent steps (Fig. 2.3h), followed by etching of oxide and nitride layers on the back side by BHF. Here, the protective resist is removed, and photosensitive resist is coated and baked; followed by UV exposure (Fig. 2.3i). Afterward, the sample is developed, and nitride layer is etched by dry etching (Fig. 2.3j) which is carried out to separate probes from each other. The remaining photoresist is stripped away in acetone/isopropanol. After that, a Pyrex wafer is diced to serve as a handle (Fig. 2.3k) followed by an anodic bonding between sample and Pyrex wafer (Fig. 2.3l). Next, Pyrex wafer is diced away where it covers the part of cantilever and the tip (Fig. 2.3m). Finally, remaining silicon is etched in KOH (Fig. 2.3n), and oxide layer in BHF (Fig. 2.3o). Here, a layer of gold or aluminum can be coated to the backside of the sample for laser reflection.

The nitride layer is coated by thin film technology (by LPCVD) that gives full control on the cantilever thickness. In case of silicon probe, the thickness is less controllable due to the wet etching. Also, the nitride is harder than silicon, so it offers better durability which makes it a good choice for contact mode measurements. However, silicon probes can be made sharper compared to nitride probes which means less resolution in the latter case.

2.3 Masked-maskless combined anisotropic etching technique for AFM probe fabrication

There are several different approaches to fabricate an AFM probe, and masked-maskless combined anisotropic etching is one of the suitable methods for fabricating high-yield AFM probes in single crystalline silicon[12]. The main idea is taking advantage of anisotropic behavior of the KOH etching for shaping conical tip which is formed from a circular shape to octagon until the tip is sharp enough. Detailed fabrication steps is discussed below and illustrated in Fig. 2.4.

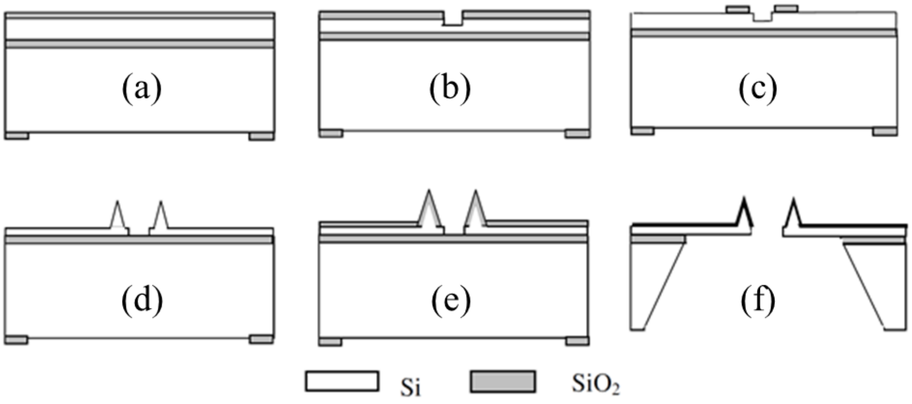

Fig. 2.4: AFM probe fabrication steps for the masked-maskless process (adopted with permission from Ref. [12]).

The fabrication starts with an SOI (Silicon on Insulator) wafer, followed by thermal oxidation to form an oxide mask layer on both sides of the wafer. Next, the backside oxide mask is patterned for releasing cantilever in subsequent steps (Fig. 2.4a). Another lithography step is carried out to pattern front side, and the mask pattern was transferred into silicon oxide followed by silicon etching in KOH (Fig. 2.4b). This step is performed to separate the cantilevers from each other in later steps. Afterward, second lithography step was carried out to define circular or rectangular oxide mask (Fig. 2.4c) that will turn into octagon and finally a sharp conical tip by a KOH etching. At the same time, the cantilevers will be separated from each other at the pit etched in previous steps which are carried out without additional masking process (Fig. 2.4d). Here the tip apex diameter is about 500 nm which is not ideal for AFM scanning. Therefore, a sharpening step is required which can be carried out by oxidizing and oxide removal steps (Fig. 2.4e). A layer of 400 nm oxide will be enough to get a sharp tip in nanoscale. Finally, the backside silicon is etched by KOH etching followed by etch stop layer removal which is the oxide layer in the SOI wafer (Fig. 2.4f). Before this step, a thick protective resist should be coated to protect AFM probes against KOH etching. There are two main advantages of this step. First, the tips and cantilevers can be fabricated at the same time with a combination of masked-maskless etching processes and involve standard low-cost processing tools. Second, the process applies to wafer scale production that makes it a high throughput process for fabricating AFM probes.

2.4 Aligned mask method for self-sharpening AFM probe fabrication

KOH is one of the most popular silicon etching chemical used in micro/nano fabrication for various applications due to its unique anisotropic behavior. It is also commonly employed in AFM tip fabrication; however, a subsequent oxidation sharpening is required after KOH etching since the tips are not self-sharpening after the mask is released. A self-sharpening process was developed by Burt et al.[13] to eliminate the oxidation sharpening step. They found that aligning a triangular mask to <310> direction forms self-sharpening tip under KOH etching with a 100% yield at large scale. The tip apex diameter can be as small as 5 nm and can be further decreased to 2 nm by oxidation sharpening if needed[13]. Li et al. take advantage of the self-sharpening process to develop fabrication steps for AFM probes[14]. Here, only tip fabrication is going to be presented; a detailed fabrication process steps for self-sharpening AFM probe is discussed in Ref. [14].

Self-sharpening occurs when the etching mask is aligned to <310> directions which can be achieved by rotating a square shape 63.4° from <110> direction in (100) plane. A similar result can be expected in the triangular mask with all edges aligned to <310> direction. Designs for square and triangular masks and optical micrograph results for under-etched Si structures are given in Fig. 2.5.

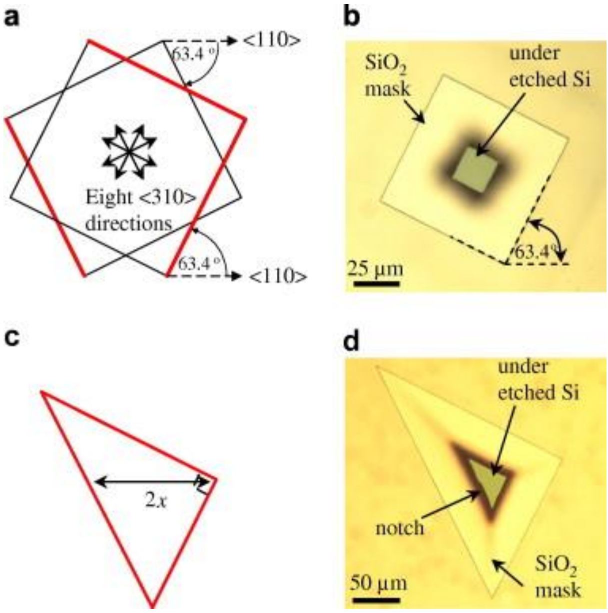

Fig. 2.5: (a) Square mask design aligned to <310> directions; (b) optical microscope image of under-etched Si with square SiO_2 mask aligned to <310> directions; (c) a triangular mask design aligned to <310> directions; (d) optical microscope image of under-etched Si with triangular SiO_2 mask aligned to <310> directions (adopted with permission from Ref. [13]).

It is clear from Fig. 2.5b and 2.5d that SiO_2 masks are aligned perfectly for both structures that will allow edges to meet at a single point. Although a notch is formed during the wet etching as shown in Fig. 2.5d, it will not affect the result. SEM images of pyramid-shaped self-sharpening tips are shown in Fig. 2.6.

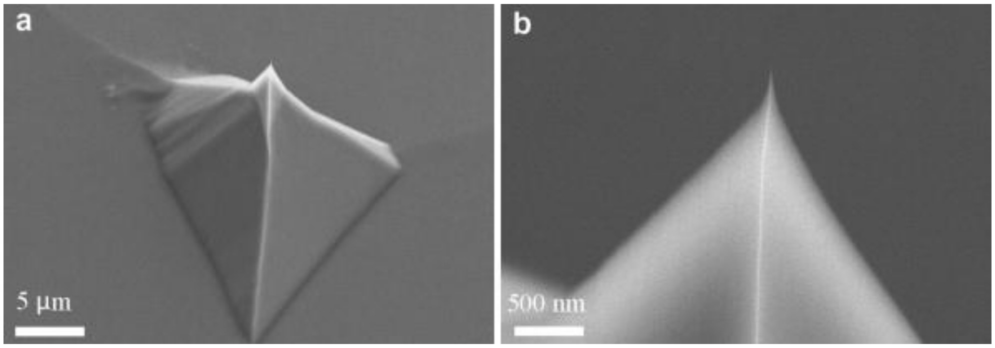

Fig. 2.6: SEM images of a pyramid-shaped silicon tip fabricated by a self-sharpening process with a viewing angle of (a) 0° and (b) 45° (adopted with permission from Ref. [13]).

As a result, diameter of <5 nm tip apex is fabricated as shown in Fig. 2.6 by self-sharpening process. The process is reproducible with high yield with the advantage of one tip etching step. Therefore, the self-sharpening process is an excellent way to fabricate conventional AFM probes as demonstrated by Li et al.[14].

2.5 Dry etching for AFM probe fabrication

Reactive-ion etching (RIE) is a dry etching technology used in nano/microfabrication that has different parameters from wet etching. It simply removes desired materials such as silicon from substrates by using chemically reactive plasma; SF_6 plasma is carried to etch silicon which is an isotropic etching. By modifying etching recipe, the etching profile can be converted to a highly anisotropic etching which is frequently performed to etch deep holes/trenches or tall pillars/walls. The process is called deep reactive-ion etching (DRIE) which is achieved by a conventional process called Bosch process combined of two steps: first, a standard nearly isotropic etching is carried out using SF_6 gas; second, deposition of a passivation layer is performed by C_4F_8 gas. The etching step removes the passivation layer at the bottom instead of on the sidewalls because of directional ion bombardment which allows etching to be carried vertically at each phase. These etching and passivation steps result in some small isotropic pits on the sidewall that is called scalloping effect. Here, each step takes only a few seconds and can be controlled to define the size of each local isotopically etched side pits. When the etching is fast enough, the scalloping effect is almost negligible.

DRIE gives better uniformity and reproducibility than wet etching in general which is also applicable to the AFM tip fabrication[15,16,17,18]. A good example of DRIE for fabrication of AFM prove is illustrated in Fig. 2.7.

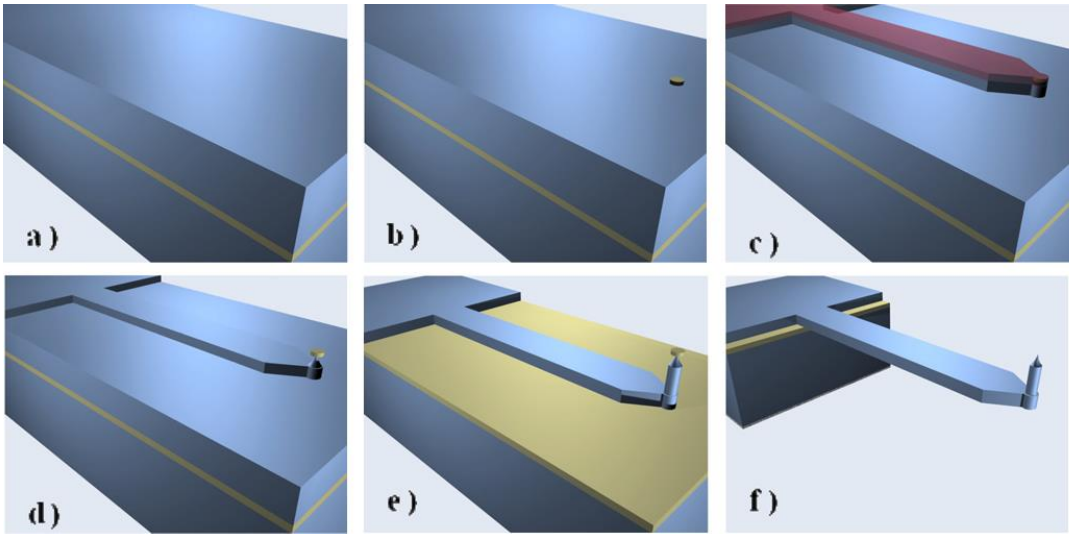

Fig. 2.7: Fabrication steps for AFM probe using DRIE (adopted with permission from Ref. [18]).

First, the fabrication starts with an SOI wafer, and a circular SiO_2 mask is defined using standard lithography tools. Next, cantilever is defined by standard lithography in a similar way and etched to the cantilever thickness where photoresist is generally good enough to mask cantilever under dry etching. After that, DRIE is performed to etch the tip shaft and tip where cycles of 2.5 s SF_6 etching with 1 s C_4F_8 deposition is used for shaft etching followed by cycles of 1 s SF_6 etching with 0.33 s C_4F_8 deposition for tip etching[18]. Afterward, the whole sample is oxidized for tip sharpening and protection for subsequent backside etching. Next, a thick layer of oxide is deposited on the backside and patterned. Finally, the backside of the sample was etched by DRIE, and all the oxide layers are etched in BHF. The fabricated AFM probes are shown in Fig. 2.8.

The advantages of the dry etching process are its high yield and reproducibility, as well as better controllability in etching profile which is achieved by adjusting etching parameters. However, DRIE is costly compared to wet etching; therefore, most of the commercial tips are fabricated using wet etching.

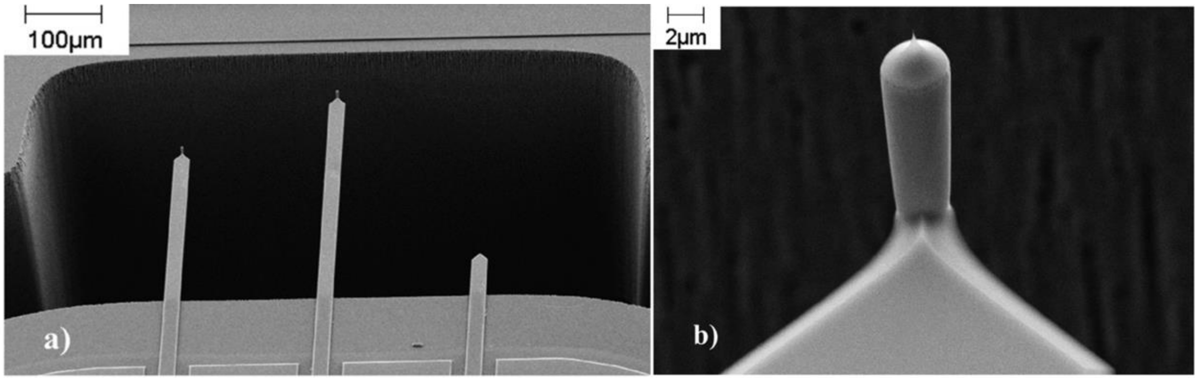

Fig. 2.8: SEM images of AFM probes fabricated by DRIE. (a) AFM probes with 3 different lengths; (b) a close view of the tip shaft and tip (adopted with permission from Ref. [18]).

2.6 Summary

This chapter first summarizes the fabrication of commercial silicon and nitride AFM probes where a combination of oxidation, photolithography, and wet etching steps are involved. In nitride probes, an inverse pyramid is formed inside the silicon for nitride to be filled, and a Pyrex wafer is diced and bounded to nitride as a handle. In the end, remained silicon and silicon oxide were etched away to release nitride probes.

Secondly, several fabrication processes in research level were introduced which are based on either wet or dry etching. In wet etching, KOH solution is selected to form pyramid shaped tips that require a subsequent oxidation sharpening. Alternatively, if a square or triangular mask is aligned to <310> directions on (100) plane, a self-sharpening tip with as small as 5 nm tip apex curvature can be fabricated. On the other hand, the entire AFM probe can be fabricated by dry etching. The etching profile can be controlled by adjusting the gas ratio between SF_6 and C_4F_8 gasses to attain very sharp tips.

Chapter 3

High aspect ratio AFM probe fabrication techniques

In this chapter high aspect ratio AFM tip fabrication methods will be reviewed including focused ion beam milling, electron/ion-beam-induced-deposition, carbon nanotube growing, angle-dependent dry etching, and one-step e-beam lithography techniques.

Although AFM has unique properties such as atomic resolution, it suffers from unfaithful images when it comes to scanning narrow and deep or tall structures. A schematic representation is shown in Fig. 3.1 where AFM tip cannot reach to the bottom of the trench or surrounding of the pillars due to its size and shape. Because of this reason, SEM is still more popular than AFM for imaging such structures.

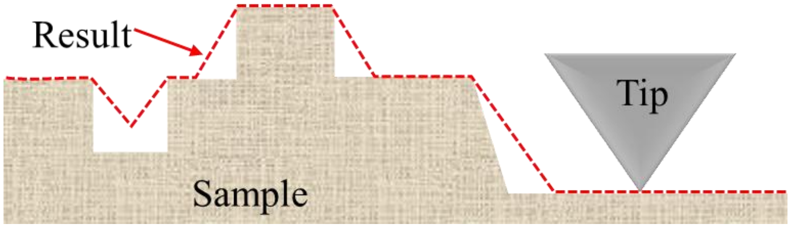

Fig. 3.1: Schematic representation of an AFM scanning by a regular tip.

A solution for the issue is the usage of high aspect ratio AFM tips where the tip apex base diameter is at least three times less than the length. This chapter reviews common and novel fabrication techniques for high aspect ratio (HAR) AFM tips including focused ion beam (FIB) milling, electron/ion-beam-induced-deposition (EBID/IBID) technique, carbon nanotube (CNT) attachment technique, angle-dependent dry etching technique, and one-step e-beam lithography technique.

3.1 Focused ion beam (FIB) milling for HAR AFM tip fabrication

Focused ion beam (FIB) is an instrument similar to SEM, yet it uses focused beam of ions instead. The ions are larger and heavier than electrons that gives a high interaction probability, but less penetration depth into the matter. The ions can remain trapped, so they can also be utilized for doping the substrates. Although ions are slower than electrons, due to their greater mass, they have a larger momentum which makes them suitable for milling. In Fig. 3.2 SEM and TEM images of ion milled HAR AFM tip are shown[19].

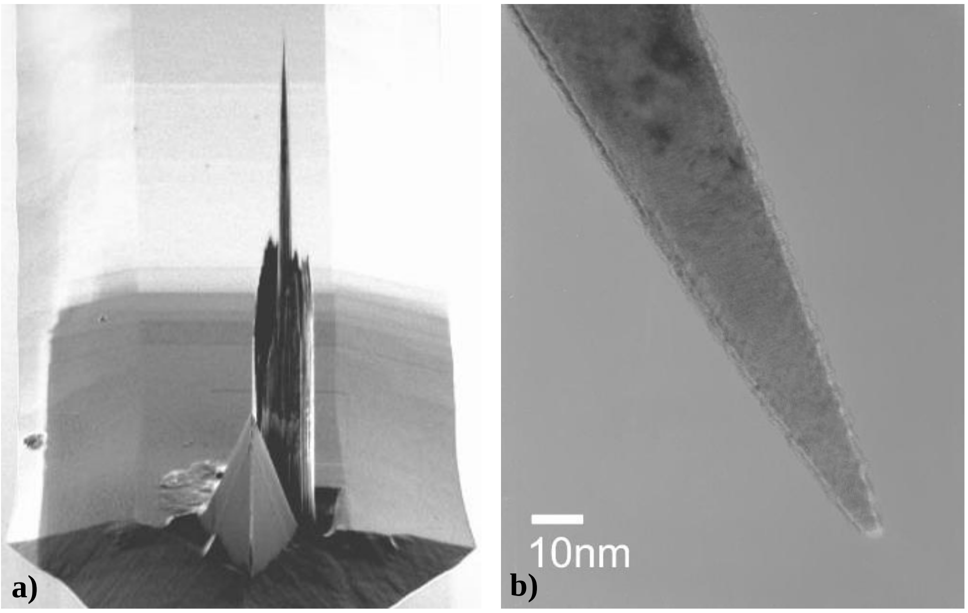

Fig. 3.2: (a) SEM; (b) TEM images of FIB milled HAR AFM tip (adopted with permission from Ref. [19]).

To start ion milling, a commercial AFM probe is frequently customized where the tip part can be partially milled away, or a deposition nearby can be carried out to refine later on (similar to the case shown in Fig 3.2). The fabrication starts with a large wire deposition of the desired material, tungsten in this case. Next, a small ring pattern is milled through the wire to define the tip part followed by larger ring pattern milling to remove remained tungsten at the outer area of the wire. This process is repeated until the tip becomes thin and long enough. A final thinning of the tip with electrochemical etching results in a tip apex of 3.5 nm as shown in Fig. 3.2b. Under FIB, the sample can be rotated to desired angle at which the deposition can be carried out. This allows the HAR AFM tips to be fabricated at the desired angle. Therefore, FIB not only provides HAR AFM tips but also gives tips with tilt angle compensation for better images. The milling can be performed on various materials with slightly different approaches. For instance, a platinum-iridium wire (PtIr) can be cut and glued to tip by FIB and subsequently sharpened[20]. In FIB, the length, angle, and tip apex are highly controllable with the precision of 0.5° angle and down to 9 nm tip apex. However, the whole process takes around 2 hours that results in a poor throughput.

In addition to metal AFM tips, nitride tips can also be machined by FIB[21] following similar approach. Nitride tips are less expensive, durable as well as insulating, so suitable for some specific areas.

While commercially available FIB instruments can handle patterning down to 5 – 10 nm[22] with the advantage of deposition and milling of any arbitrary shape, it is a slow process. Therefore, it is not suitable for commercialization for HAR AFM tip fabrication. Moreover, the process relies on pre-fabricated AFM tips that would significantly increase the overall cost.

3.2 Electron/ion-beam-induced deposition (EBID/IBID) for HAR AFM tip fabrication

Electron-beam-induced deposition (EBID) is a deposition process where a precursor is dissociated by an electron beam produced by either SEM or TEM. EBID is accounted as a direct writing technique in nanometer resolution; <3 nm resolution by SEM[23] and <1 nm resolution by TEM[24] have been reported. Furthermore, three-dimensional and free-standing structures can be deposited where deposited structures can be monitored in situ during or after the deposition. A large range of materials can be deposited by EBID including Al, Au, C, Co, Cr, Cu, Fe, GaAs, Mo, Ni, Os, Pd, Pt, Rh, Ru, Re, Si, Si_3N_4, SiO_x, TiO_x, and W, reported in 2006[25]. There are some drawbacks of the technique such as because the deposition is carried out by focusing a small area, EBID provides a poor throughput compared to top-down fabrication. During deposition, electrons can penetrate to the substrate, and collide with substrate electrons that cause forward scattered and backscattered electrons. A percentage of these electrons contributes to deposition outside of the predetermined deposition pattern which is called proximity effect. Due to proximity effect, a dense pattern array with as good resolution as a single dot or line structures is not possible.

Ion-beam-induced deposition (IBID) is similar to EBID but uses an ion beam to interact with the substrate. A large mass of the ions can cause damage and re-deposition during imaging. To solve this problem, dual beam instruments have emerged which have both FIB and SEM. While EBID can handle better resolution, IBID can achieve much higher deposition rates.

Because of high-resolution capabilities of the EBID and IBID, they can grow HAR AFM tip onto a regular tip apex.

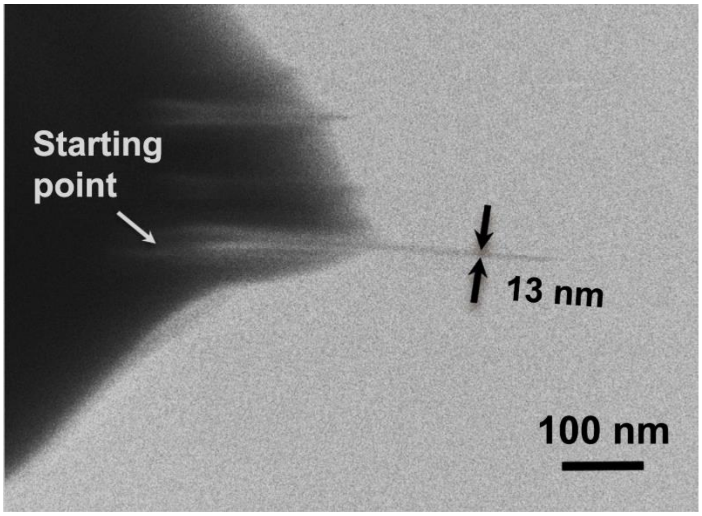

Fig. 3.3: Helium ion microscope image of nanoneedle grown by IBID on a regular AFM tip (adopted with permission from Ref. [26]).

An example HAR PtC AFM tip grown on a regular AFM tip apex by IBID is shown in Fig. 3.3[26], where needle diameter is controlled by dwell time and ion dose. With a controlled process, Nanda et al.[26] achieved 13 nm tip diameter with 700 nm length; thicker tips can be grown by just increasing the dose. In this technique, there is a flexibility in tip shape where various tip geometries can be obtained. For instance, a hammerhead shape was fabricated[26] for 3D-AFM probe where the tip can scan vertical trench edges.

Although EBID and IBID can achieve perfect structures, the tool itself is expensive and not commonly available. Also, the overall fabrication takes hours to fabricate a single tip that leads a poor fabrication throughput compared to standard tip fabrication methods. Therefore, different fabrication approaches are needed.

3.3 Carbon nanotube (CNT) HAR AFM tips

Carbon nanotubes (CNT) are cylindrical carbon molecules with unique properties that gathered attention in nanotechnology. The CNT's length can be grown hundred million times greater than its diameter[27] which can be as small as 0.43 nm[28]. Such extraordinary high aspect ratio leads researchers to use it as a HAR AFM probe. There are several different ways to obtain CNT tips mainly based on either growing CTN or attaching CNT on a regular AFM probe [29,30]. A single-walled nanotube can achieve very high resolution due to its fine diameter, but its probing depth is limited because of thermal vibrations. Alternatively, multiwalled nanotubes can perform better probing depth but less resolution due to their larger diameter[31]. Tang et al.[32] accomplished CNT AFM probes with 20 nm tip diameter with rounded tip apex, and 700 nm length by room-temperature liquid-phase dielectrophoresis technique. An example is shown in Fig. 3.4.

The fabricated tips were tested for imaging 4.5 µm deep trenches and show very accurate results[32] compared to traditional AFM tips. Compared to FIB milled, or EBID/IBID fabricated tips, CNT tips provide a smaller tip diameter. Additionally, CNT tips have a significantly longer lifetime than silicon tips[33]. However, tips are frequently getting broken with cantilever before attaching/growing CNT due to handling or other processing steps.

Furthermore, attaching or growing CNT on tip apex is a challenging task with the desired position, orientation, and length.

So far some of the HAR AFM tip fabrication methods that focus tips sharpening/growing one by one were reviewed. In the following sections, cost-efficient and high throughput methods will be examined.

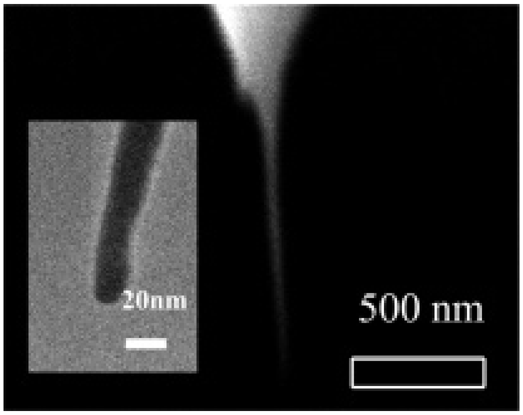

Fig. 3.4: SEM image of CNT AFM tip; inset: a high-resolution TEM image of the tip (adopted with permission from Ref. [32]).

3.4 Angle-dependent dry etching technique using advantage of angle-dependent sputtering yield

For fabrication of HAR AFM tips, a recent novel method emerged[34] that benefits from angle dependence of sputtering where different incident angles result in different thicknesses of the target material. A controlled etching can leave mask material on the tip apex and remove the rest of it, which can be later on used as dry etching mask to form HAR AFM tip. The process followed is illustrated in Fig. 3.5.

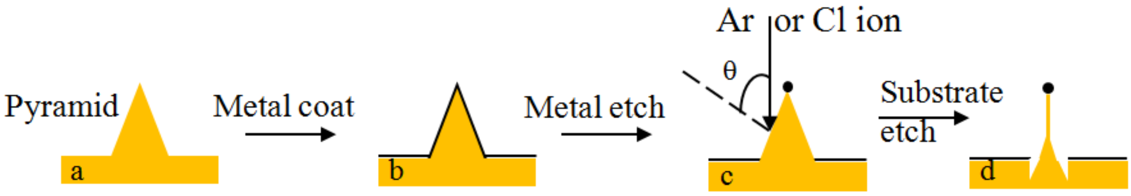

Fig. 3.5: Process steps to fabricate HAR AFM tip benefiting from angle dependent sputtering yield and dry etching (adopted with permission from Ref. [34]).

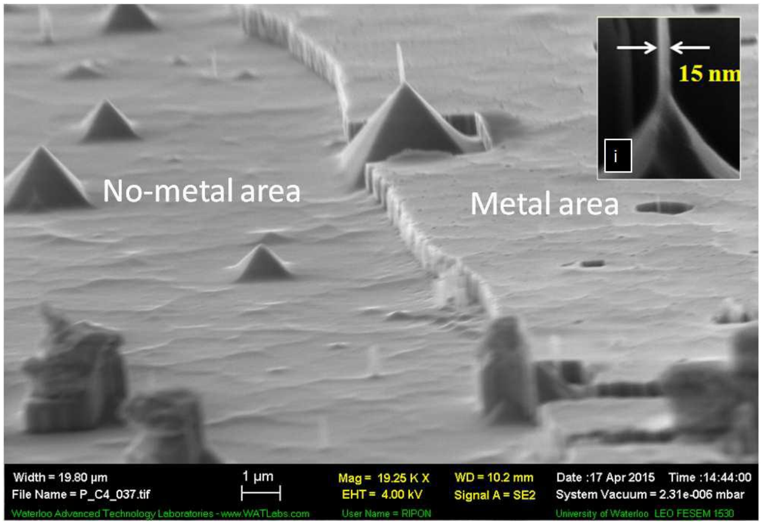

Fig. 3.6: SEM image of HAR tip fabricated by benefiting from angle dependent sputtering yield and dry etching (adopted with permission from Ref. [34]).

By tuning the mask material thickness, the pillar diameter can be adjusted because thicker film leaves wider mask material on the tip apex. Moreover, the tip morphology can be controlled by tuning DIRE process parameters. An example of the process is shown in Fig. 3.6 where silicon pyramids were formed for testing. The fabrication process results in 15 nm tip diameter. Alternatively, 2 layers of masks can be coated where top mask material can be used to mask bottom mask material where taller tips can be expected if etching selectivity is good between the masks and the substrate. The process is not only applicable to silicon but also nitride AFM probes. In Fig. 3.6 a commercial nitride tip is sharpened by the process to form high aspect ratio tip on the regular tip apex.

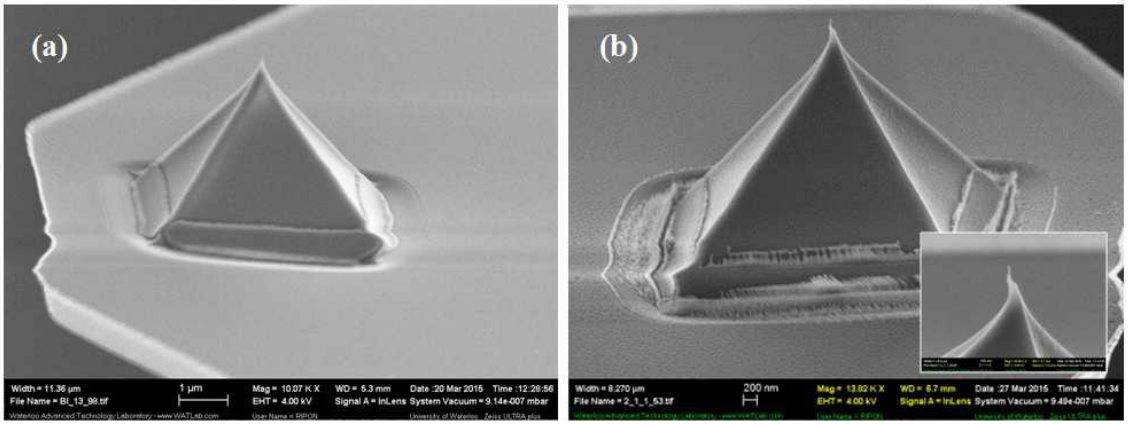

Fig. 3.7: SEM images of (a) a regular nitride AFM tip; (b) sharpened nitride AFM tip (adopted with permission from Ref. [34]).

The process is lithography-free and does not require to focus tips one by one. Therefore, it has high throughput and low fabrication cost. However, the process still relies on pre-fabricated AFM tips which will eventually increase the overall fabrication cost. During the fabrication process, there is a chance to break the tips with cantilevers similar to CNT tips. Furthermore, as the process is highly deposition angle dependent, there will be a yield issue when handling a large-scale deposition because the deposition rate will be different; the deposition is faster close to the target. Although the difference is not so significant for a 4" wafer, it will still affect the process because even a small deviation will result in a different mask size.

3.5 One-step e-beam lithography technique (our method)

All the reviewed methods above are based on refining pre-fabricated commercial AFM tips which increases overall fabrication cost significantly. On the other hand, most of the techniques suffer from high throughput. Fabrication of HAR AFM tips with a high throughput can be carried out by DRIE process similar to the process discussed in Chapter 2 by tuning etching parameters. However, that process involves a couple of lithography steps which would increase the fabrication cost.

Here, we report process steps consist of one lithography step that defines both cantilever and tip pattern at the same time where lithography involves spin-coating, baking, exposure and development steps. The process not only benefits from fabrication cost but also simplicity. The method will be discussed in Chapter 5 in detail.

3.6 Summary

In this chapter, several popular HAR AFM tip fabrication techniques are reviewed. HAR tips are important because they provide more accurate image profile, especially in dense, deep and tall structures. FIB milling, EBID, IBID, and CNT can handle ultra-high aspect ratio AFM tip fabrication where the first three methods can control the angle, height, and dimensions precisely. All these methods provide excellent AFM scanning performance. Especially CNT provides a great tip profile, but the overall fabrication is more complicated than others. The techniques rely on one by one fabrication that increases fabrication cost and suffers from throughput.

Alternatively, an angle-dependent dry etching technique using the property of angle-dependent sputtering yield emerged for batch fabrication of HAR AFM tips. However, the method relies on pre-fabricated commercial tips that increases the overall cost.

Chapter 4

AFM tip fabrication by UV lithography

In this chapter, batch fabrication of HAR AFM tips will be introduced, and etching methods with important processing parameters will be discussed.

4.1 A complete fabrication process to fabricate HAR AFM tips using UV lithography

Batch fabrication of HAR AFM tips is highly demanded because of their high cost of \$70 to \$500 per tip when fabricated one at a time (not batch fabrication)[34]. Here, we first introduce a standard procedure to fabricate high aspect ratio tips on large scale where we carried out DRIE to form HAR AFM tips. In Fig. 4.1, our process steps to fabricate HAR AFM tips are illustrated.

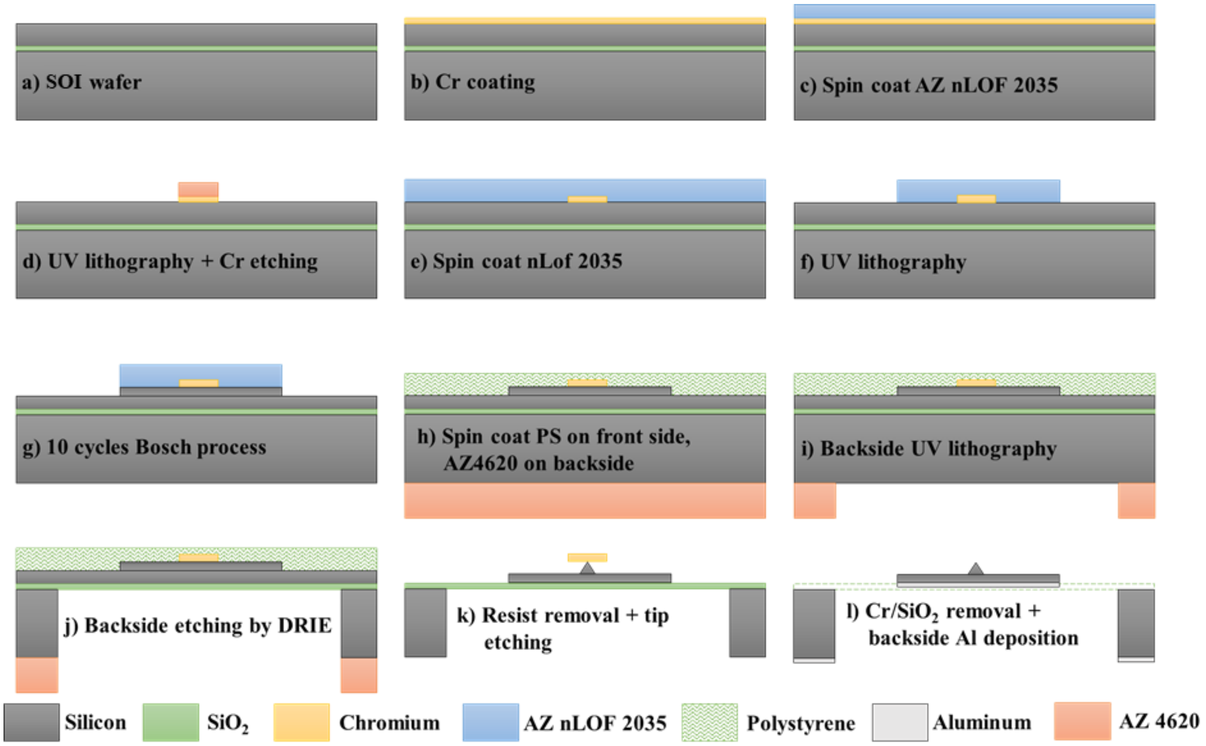

Fig. 4.1: A schematic representation of the HAR AFM tip fabrication by UV lithography.

As summarized in Fig. 4.1, the fabrication starts with a SOI wafer consisting of 13 µm device layer, 1 µm SiO_2 layer and 350 µm handle wafer. The wafer is first cleaned with acetone ultrasonication, isopropanol rinse, nitrogen blow, and 2 min oxygen (O_2) plasma under 20 W RF power, 20 sccm O_2 flow, 20 mTorr chamber pressure conditions (Fig. 4.1a). Next, as a hard mask to define tip pattern, 140 nm chromium (Cr) layer is deposited by Intlvac e-beam evaporator with 1 Å/s deposition rate to obtain a good uniformity (Fig. 4.1b). After that, a layer of negative photoresist (AZ nLOF 2035) is spin-coated at 4000 rpm for 40 sec followed by 1 min baking on a hotplate at 110 °C (Fig. 4.1c). Tip pattern is defined by a CAD software, and the sample is exposed at 700 mJ/cm^2 by MLA150 direct write UV lithography system capable of good resolution down to 1 µm under optimized conditions. Next, post-exposure baking is performed at 110 °C for 1 min where the temperature and baking time is so important for this particular resist as it determines the sidewall profile; lower temperatures cause higher negatively tapered profile. The exposed resist is then developed in AZ 300MIF developer for 1 min at room temperature followed by DI-water rinse and hard baking at 110 °C for 1 min that is important for subsequent etching step. Here, resist pattern is transferred into Cr by dry etching using conditions of 42 sccm Cl_2, 8 sccm O_2, 12 mTorr chamber pressure, 10 W RF power, 1200 W ICP power, and 50 °C etching temperature (Fig. 4.1d). Next, remained photoresist is stripped in acetone, and another layer of photoresist is spin-coated (Fig. 4.1e) and patterned using same parameters to define cantilever pattern (Fig. 4.1f). Here, photoresist will be used as a mask to transfer the pattern into silicon where 10 cycles of Bosch process is carried out to etch about 4 µm silicon followed by subsequent resist removal (Fig. 4.1g). At this point the backside of the wafer is processed to define holder part of AFM probe before etching into the tip because otherwise there is a high chance of damaging the tip while working on the backside. Therefore, a layer of polystyrene is spin-coated on the front side for protection; the polystyrene is preferred because it does not stick to hot plate, which will be required in subsequent processing steps. Next, a cleaning step is followed by two layers of AZ 4620 positive photoresist spin-coated at 2000 rpm for 40 sec (Fig. 4.1h). After each spin-coating, the sample is baked at 90 °C for 5 min. The total resist thickness is nearly 24 µm which is thick enough to mask entire 350 µm thick silicon under DRIE. The exposure is carried out by direct write UV lithography system with 1800 mJ/cm^2 exposure dose. The sample is then developed in AZ 400K, KOH based developer, for 8 min and rinsed by DI-water (Fig. 4.1i). At this stage, a photo and an optical microscope image of the sample backside are illustrated in Fig. 4.2 and Fig. 4.3, respectively. There are some bubbles formed in photoresist due to its thickness and other environmental reasons which will be discussed in detail in the following sub-topic.

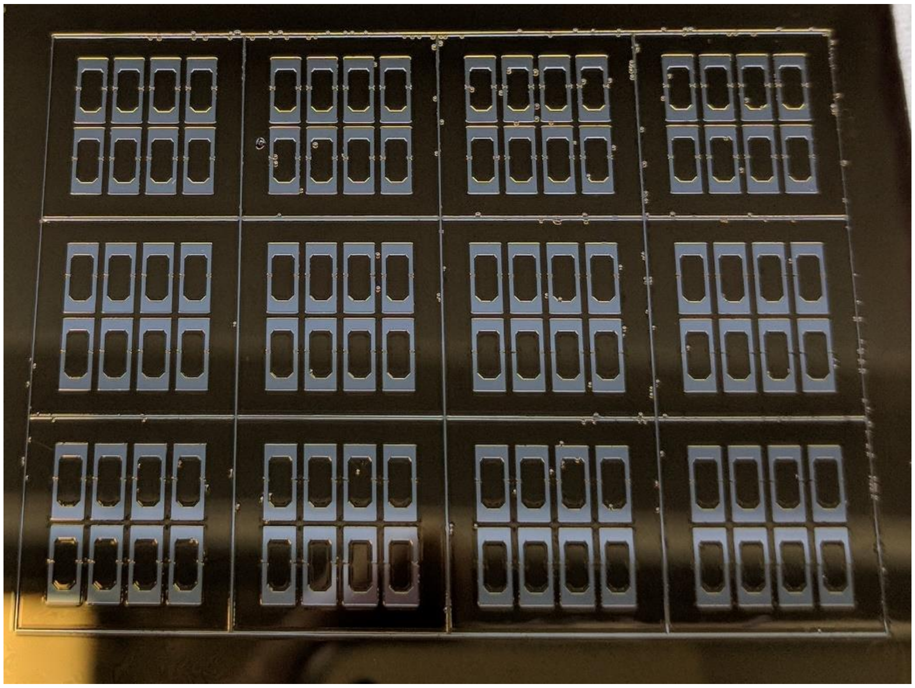

Fig. 4.2: A photo of the sample backside after development.

The sample consists of 96 AFM probes. Afterward, the sample should be baked prior to the DRIE which is one of the most critical steps. If the sample is not baked well enough, the photoresist mask will be consumed before the entire wafer is etched. Therefore, it is baked at 120 °C for 45 min on a hotplate soon before DRIE. Next, 850 cycles Bosch process is carried out to etch 350 µm of backside silicon (Fig. 4.1j and Fig. 4.4), and remained photoresist, and protective layer of polystyrene are striped in acetone (Fig. 4.5).

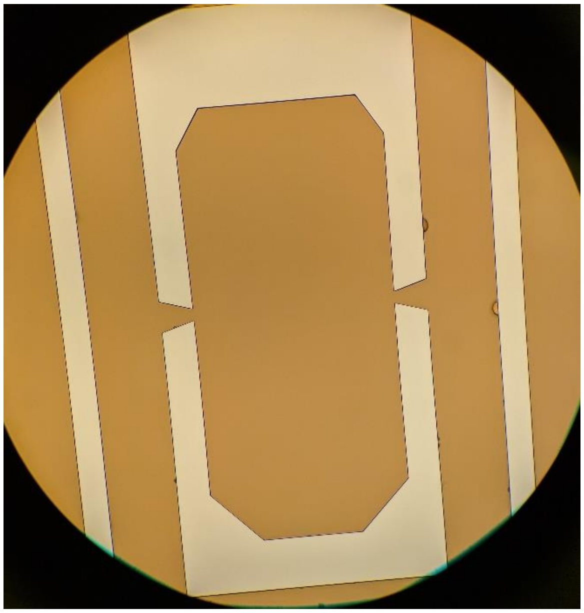

Fig. 4.3: An optical microscope image of sample backside after development.

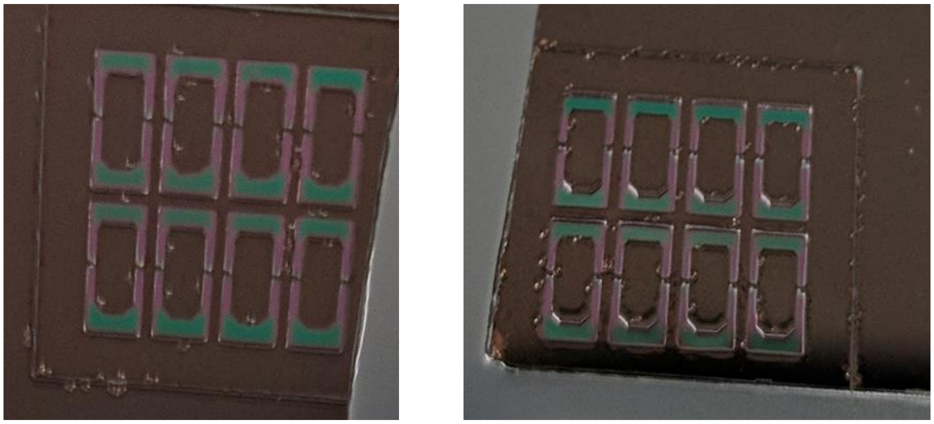

Fig. 4.4: Images of two samples after backside silicon etching.

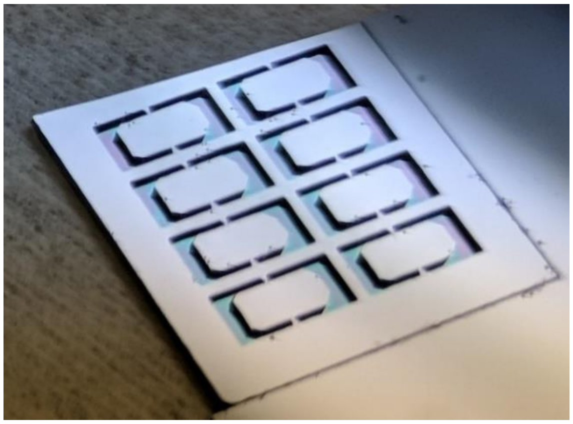

Fig. 4.5: An image of the sample after backside photoresist stripping.

At this point, non-switching Bosch process is carried out to form the AFM tip under 20 W RF power, 1200 W ICP power, 10 mTorr chamber pressure, 15 °C chamber temperature; gas flows of 46 sccm C_4F_8 and 14 sccm SF_6 etching parameters (Fig. 4.1k). The etching is highly non-isotropic with controlled angle resulted from the nature of the non-switching Bosch process, which will be discussed in detail in the following sub-topics. Finally, remaining Cr and SiO_2 films are removed to release cantilever, by Cr etchant (8% ceric ammonium nitrate in 1:5 acetic acid: DI-water) and HF (37 min 1:5 HF: DI-water) solutions, respectively, followed by 60 nm Al deposition by e-beam evaporation on backside as reflection layer (Fig. 4.1*l*). It should be noted that some of the SEM images are taken with Cr mask still present. SEM images of the fabricated AFM probes are shown in Fig. 4.6, 4.7 and 4.8.

The probe is designed to have a size of 45 µm × 125 µm cantilever with various tip diameters. Fig 4.6b shows the tip with 1.2 µm base diameter, 10.1 µm tip height, and 178 nm diameter at the thinnest point close to the tip apex. As can be seen in the image, there is some undercut close to the top which happens because pillar sidewalls start to act as a “substrate” (note that ion has a tendency to strike the “substrate” at local normal direction) after certain height is reached. AFM tip fabrication can benefit from undercut to etch very sharp tips. In Fig. 4.7 another example of the fabricated tip is shown where the tip got broken at thinnest point during processing which is still attached to the tip end.

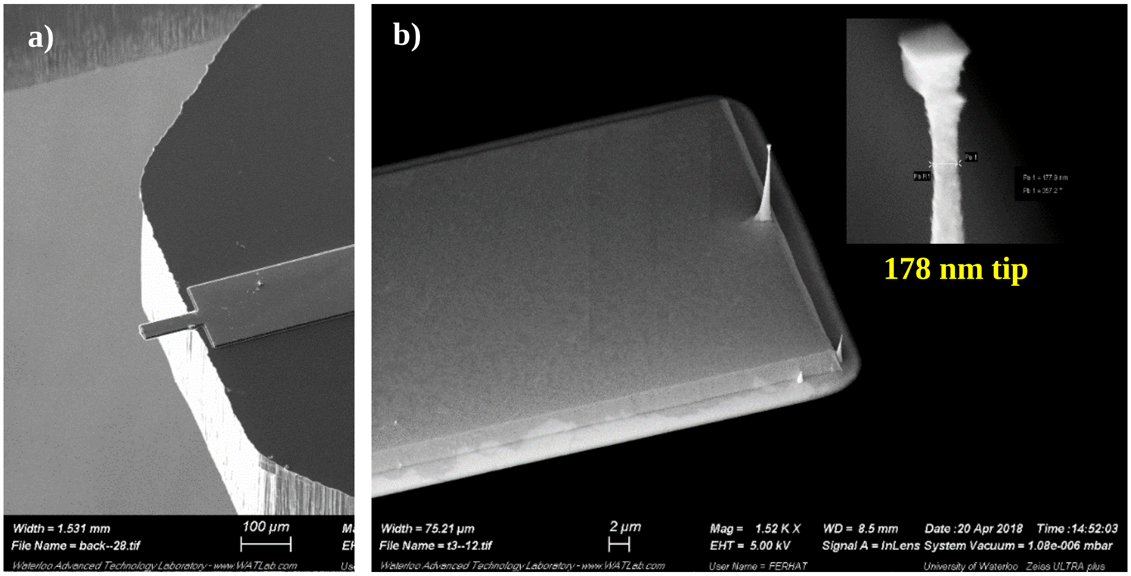

Fig. 4.6: 45° SEM images of fabricated AFM probes; (a) overview of cantilever holder and the tip; (b) closer view of cantilever and the tip, inset: zoomed in image of b.

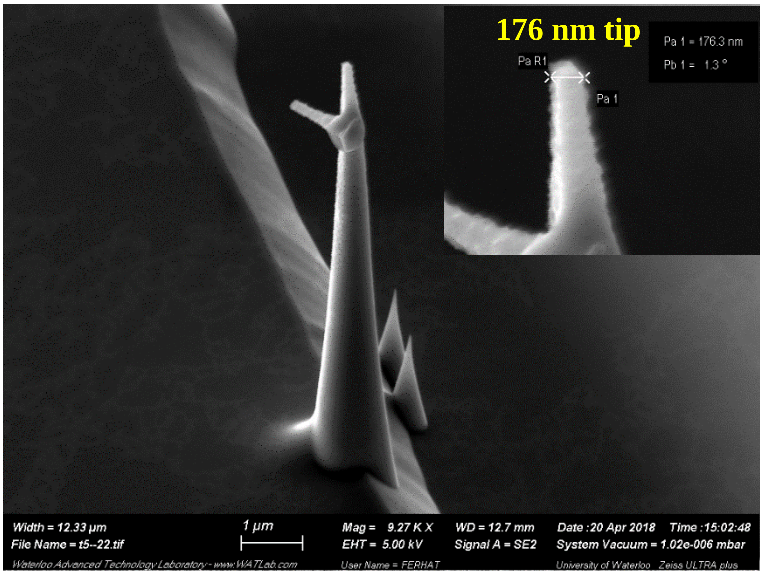

Fig. 4.7: 45° SEM image of fabricated AFM tip, inset: close view of the tip.

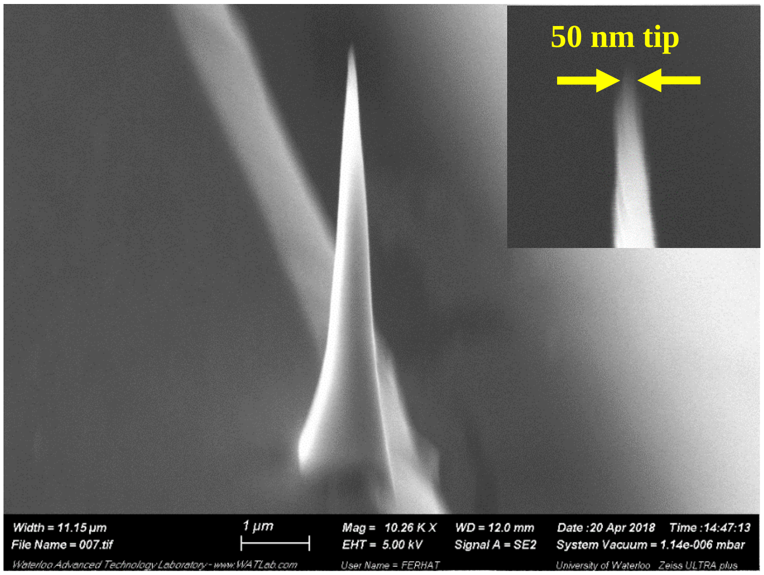

Fig. 4.8: 45° SEM image of fabricated AFM tip, inset: close view of the tip.

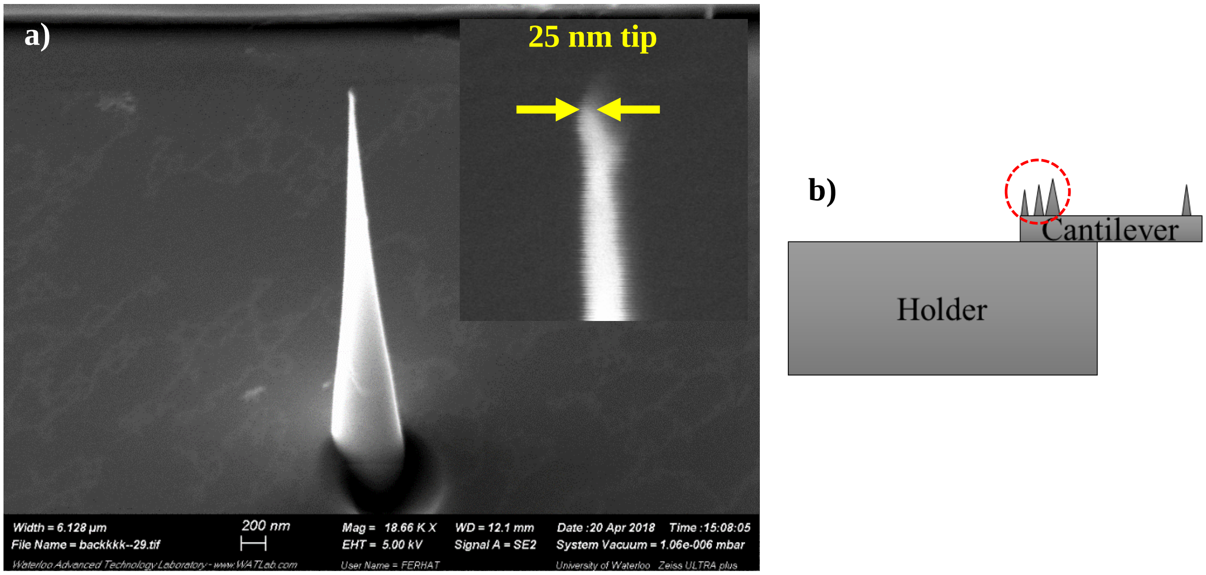

Fig. 4.9: (a) 45° SEM image of a tip fabricated at the far end of the cantilever, inset: close view of the tip; (b) a schematic showing where the far-end is.

For both tips' in Fig 4.6 and 4.7, the base diameter was designed to be 1.2 µm resulting in practically the same tip diameter after DRIE process. A bit longer etching would result in thinner tip apex. Fig. 4.8 shows SEM image of a slightly smaller AFM tip with 8.3 µm height, 1 µm base diameter and 50 nm tip diameter resulting in better tip profile. The height is 1.8 µm shorter than the tip shown in Fig 4.6 which is probably because of breakage of the tip. A short over-etching made the tip a bit blunt to have 50 nm diameter. Some extra tips with different dimensions are also designed at the far end of the cantilever to be able to compare the results for each. In Fig. 4.9, a tip with 600 nm base diameter, 4 µm height and 25 nm tip diameter is shown. This is the sharpest tip fabricated in the same run due to its smaller mask diameter. Although the tip shrank down to 4 µm, it can still be used as an AFM tip. More tips were fabricated in similar shape with the one presented in Fig. 4.8 which are not included here to avoid repetition.

Even though some tips with undercut profile does not seem usable, they can still be improved by oxidation sharpening that would give even a better tip profile. The oxidation can be performed until oxide meets in the center of the thinnest point on the tip, then the oxide can be removed by HF. A well-controlled process can result in tips with as small as 3 nm apex as mentioned previously. The oxidation sharpening process will be discussed in detail in Chapter 5.

Furthermore, one of the fabricated tips was installed to Dimension 3100 AFM for testing. The cantilever view from AFM camera is shown in Fig. 4.10. As it can be noticed, the cantilever looks shorter than real size, which is because the holder is etched in DRIE with almost no slope, and AFM scanning is carried out at a certain angle that makes some part of the cantilever shadowed. A solution for shadowing problem will be introduced at the end of the following chapter.

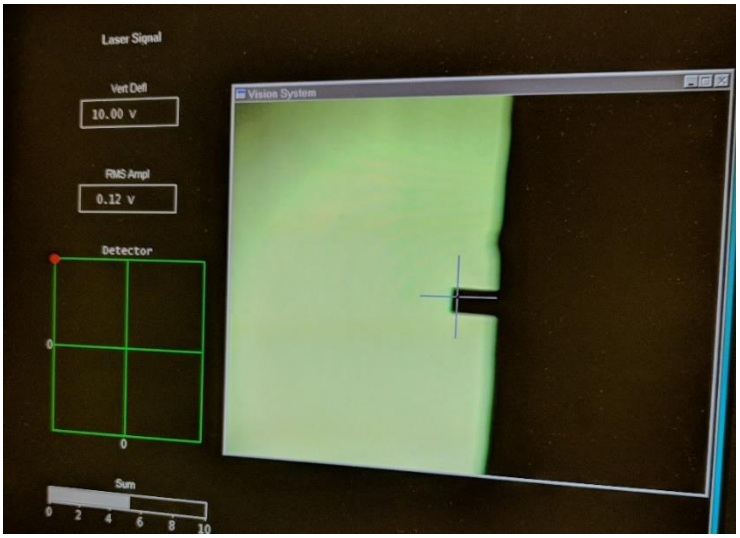

Vert Defl 10.00 V

RMS Ampl 0.12 V

Fig. 4.10: Cantilever backside viewed by AFM camera.

One of the properties of the AFM tip is the resonance frequency which is directly measured by AFM. The drive frequency vs. amplitude curve is given in Fig. 4.11 where the resonance frequency of the tip was found to be 149 kHz.

Fig. 4.11: Drive frequency vs. Amplitude curve of fabricated AFM tip.

Lastly, an AFM measurement was performed using Dimension 3100 scanning probe microscope to confirm it is working. Due to lack of pre-patterned sample, a piece of bare silicon was scanned. The result is shown in Fig. 4.12.

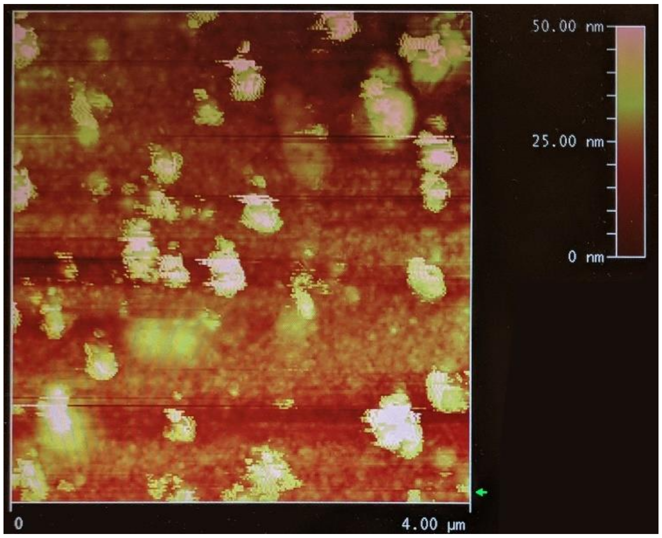

Fig. 4.12: AFM measurement on bare silicon substrate (4 µm × 4 µm area scanned with 0.6 Hz scan rate (4.81 µm/s tip velocity), and 256 samples/line.).

We could not get permission to re-characterize our tip to scan a sample with known dimensions on it. As a result, we can only say that the fabricated tip is working with an acceptable resonant frequency and a good tip profile confirmed by SEM images.

Next, some of the fabrication parameters mentioned above will be discussed in following sub-topics.

4.1.1 Working with thick photoresist

AZ 4620 is the main photoresist suitable for etching mask for holder part of the AFM as a mask for DRIE. It is preferred to simplify the overall fabrication where it involves only spin-coating and baking steps, avoiding extra hard mask (oxide, nitride or metal film) coating/growing not to mention etching or lift-off process to transfer the pattern into the hard mask. Under optimized parameters 10 – 12 µm photoresist is enough to etch whole 350 µm silicon using standard Bosch process, meaning nearly 1:35 selectivity (referring Oxford Instruments ICP380 at Quantum NanoFab located in University of Waterloo). Some parameters should be paid with attention when working with photoresists, and some of them especially crucial for thick photoresists are rehydration, nitrogen outgassing, and hard bake parameters. Each one will be discussed briefly below.

Rehydration: DNQ-sulphonates based photoresists require water content in certain amount for exposure. The baking process after spin-coating (soft bake) hardens the photoresist and decreases the water concentration significantly. Water content should be available in certain amount to have reasonable development time on exposed areas. Therefore, depending on the resist type and the thickness, the sample should be rehydrated after soft baking. In processing technology, 1 µm thick resist is generally spin-coated that requires only 10 – 15 s for rehydration in a usual cleanroom environment. This short time would be already passed after transferring sample from hot plate to the mask aligner for exposure. Thus, it does not require to pay extra attention to the rehydration. Due to the same reason, people who work in cleanroom environment often are not aware of the concept. In case of thick photoresist, the rehydration time is extremely important. For instance, 1 min rehydration extends development time to 100 min while 10 min rehydration results in 10 min development time for a 20 µm thick resist[35]. This may make one think that the exposure dose is not enough for the photoresist at that thickness when seeing the sample not getting developed after a long time. The rehydration conditions can be obtained from suppliers for a specific type of the photoresist. The concern with under-rehydrated samples is not only the development time but also the sidewall profile of the resist. Over-development can cause a slope on the sidewalls while sufficient rehydration should result in steep sidewall profile due to the shorter development time.

In our experiments, we rehydrated our samples several hours after soft baking because of the low humidity in the clean room to avoid this problem.

Nitrogen formation during exposure: Most of the positive photoresist releases nitrogen during the exposure. In the case of thin photoresists, the exposure dose is relatively low which results in a small amount of nitrogen releasing that can escape rapidly and will not cause trouble. However, thick photoresist requires relatively high doses that causes large volume of nitrogen formation, which can be a severe problem. There are two incidences where nitrogen can affect process: during exposure and during hard bake. If the resist is thick enough, a high exposure dose can cause nitrogen gas trapped inside the resist causing a sponge-like appearance on exposed areas. This may affect pattern roughness and resolution. One solution to solve this problem is exposing the sample in several low exposure doses with a delay between each exposure to let the nitrogen diffuse out. The hard baking makes the nitrogen outgass faster which causes immediate nitrogen bubble formation that deforms the resist while nitrogen escapes. To avoid this problem, in our experiments we rest the sample for several hours at room temperature to let nitrogen escape slower. Some minor deformations can be observed in Fig. 4.2 and 4.4 which did not affect the device.

Hard bake and reflow: A hard bake is a baking step performed after development step to make the photoresist pattern more stable against wet or dry etching steps. Although soft bake is performed to reduce the solvent content of the photoresist, for thick photoresist long enough baking time and appropriate temperature should be applied during the hard bake to reduce solvent content to a reasonable amount. Longer and higher temperature baking hardens the photoresist which is desired for subsequent dry etching process to accomplish a good selectivity. However, further hardening resist causes brittleness; occasionally, visible cracks can be seen on photoresist. The risk of crack formation can be reduced by slowly cooling down the sample. On the other hand, it becomes very difficult to remove the hardened photoresist using standard strippers. The issue can be solved by using some special removers. Another important resist process parameter is reflow which means photoresists flow if they are baked above their softening point. In the case of thick photoresists, the reflow amount is significant at high temperatures, causing rounded pattern edges and poor resolution. In our experiments, we hard baked the sample at low temperatures of 110 °C to 120 °C and kept baking time at least 30 min to avoid reflow and cracks.

Lastly, the photoresist should be baked right before the etching to obtain good selectivity and adhesion. Over time, the photoresist becomes rehydrated that causes lower dry etching resistance. Due to this fact, some people call hard bake as pre-etching bake. In our experiments, we have followed pre-etching bake tradition and obtained quite decent selectivity between photoresist and silicon.

4.1.2 Bosch process

The Bosch process is a dry etching process to fabricate anisotropic structures in silicon. The process consists of two consecutive steps repeated until the desired depth is achieved: etching step using SF_6 gas and passivation step using C_4F_8 gas. The process is illustrated in Fig. 4.13 where using an etching mask (Fig. 4.13a), the silicon sample is etched using SF_6 gas (Fig. 4.13b) which etches isotopically. To avoid widening of the structure, the etching step is performed for a short time. Next, a passivation layer is coated using C_4F_8 gas (Fig. 4.13c) followed by repetition of etching step (Fig. 4.13d). Although the passivation layer coats the entire substrate, only the passivation layer at horizontal surfaces are etched due to directional ion bombardment in the etching step.

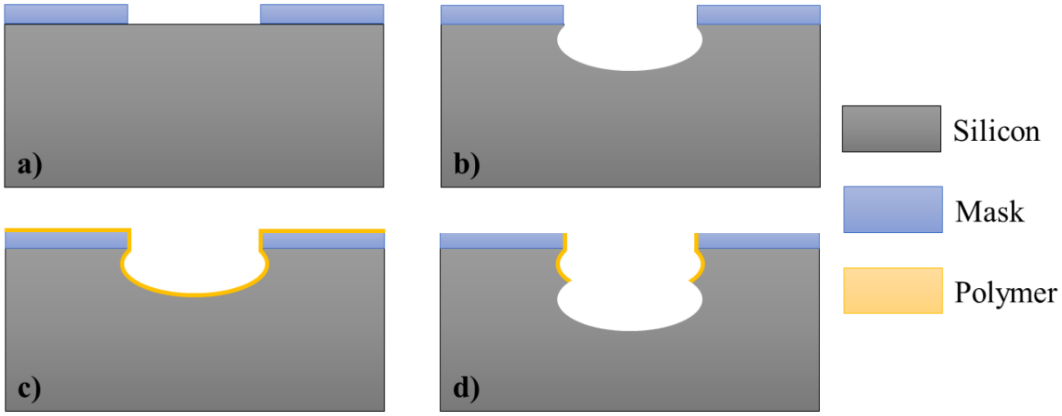

Fig. 4.13: A schematic representation of the Bosch process.

As represented in Fig. 4.13d, each etching cycle causes a trench pattern on the sidewall which is also called scalloping effect. This effect can be minimized by tuning etching and passivation time to be very short, which requires a sophisticated reactive ion etcher that can switch gasses very fast. Another solution could be an edge smoothening step where a short isotropic etching can be applied to etch away the trenches. Moreover, the etching profile can also be tuned: shortening etching step will cause narrowing at the bottom; shortening passivation step will cause widening at the bottom.

We have utilized the following Bosch recipe throughout our experiments which etches silicon about 400 nm/cycle.

Etching: 7 sec, 160 sccm SF_6, 20 W RF, 800 W ICP, 25 mTorr, 15 °C.
Passivation: 5 sec, 160 sccm C_4F_8, 5 W RF, 800 W ICP, 20 mTorr, 15 °C.

Lastly, the etching profile can be controlled by introducing two gasses, SF_6 and C_4F_8, to etching chamber at the same time. The ratio between the gasses determines the etching profile with smoot sidewalls. This process is known as pseudo-Bosch process or non-switching Bosch process. Next section will review the non-switching Bosch process as it plays a major role in AFM tip fabrication.

4.1.3 Non-switching Bosch process to define tip profile

A part of this section is reprinted with permission from Ref. [42]. Copyright (2018) American Vacuum Society:

> Ayari-Kanoun, A., Aydinoglu, F., Cui, B. and Saffih, F., 2016. Silicon nanostructures with very large negatively tapered profile by inductively coupled plasma-RIE. *Journal of Vacuum Science & Technology B, Nanotechnology and Microelectronics: Materials, Processing, Measurement, and Phenomena*, 34(6), p.06KD01.

Silicon patterning is required in many micro- and nano-scale applications including AFM probe fabrication. Developing etching processes for fabrication of demanding applications is essential. Especially, fabricating HAR structures with tunable etching profile can be critical for a wide range of applications including solar cells[36], microelectronic devices such as lasers and finFETs[37], chemical analyses[38], HAR AFM probes, and so on. All these applications can benefit from non-switching Bosch process as it allows pattern transferring while maintaining mask resolution[39]. On the other hand, some applications specifically require tapered profile such as antireflection structure for photo-detectors and solar-cells[40]. While anisotropic wet etching using KOH or tetramethylammonium hydroxide (TMAH) allows etching at a fixed tapering angle, non-switching Bosch process can etch structures with positive taper angle up to 39°,[41] and negative taper angle down to -9.7° [42] for which experiments were performed on pillars with 1 µm diameter where bottom part of the pillars becomes extremely thin at that angle. Even larger negative angles could be obtained under this process. To obtain AFM tips with desired tip profile and smooth sidewall, we also studied the non-switching Bosch process which will be discussed in this section.

While there are plenty of studies regarding vertical or positive taper angle silicon structures, only a few studies are reported in the literature regarding structures with negative taper angle profile that can potentially find applications in fabrication of hydrophobic and omniphobic surfaces which repel both water and oil[43], fabrication of reentrant AFM probes that allows sidewall imaging[44], and single electron transistors[45]. While positively tapered structures have thinnest point on top, negatively tapered structures require extra attention because the thinnest point will be at the bottom that may cause detached structures in case of over-etching. In the extreme case, without passivation by C_4F_8, pure SF_6 etching of silicon is isotropic like wet etching, because etching of silicon in fluorine-based plasma is spontaneous without the need of damage by ion bombardment, and the sticking coefficient of the etching species (free radicals) is only ~0.01, so they mostly bounce back after hitting the etch bottom/sidewall to etch the silicon right below the mask. Thus, non-switching Bosch process has been studied to develop recipes to obtain better control in etching processes.

We have patterned thick Cr structures on silicon substrate by following the process steps shown in Fig. 4.14.

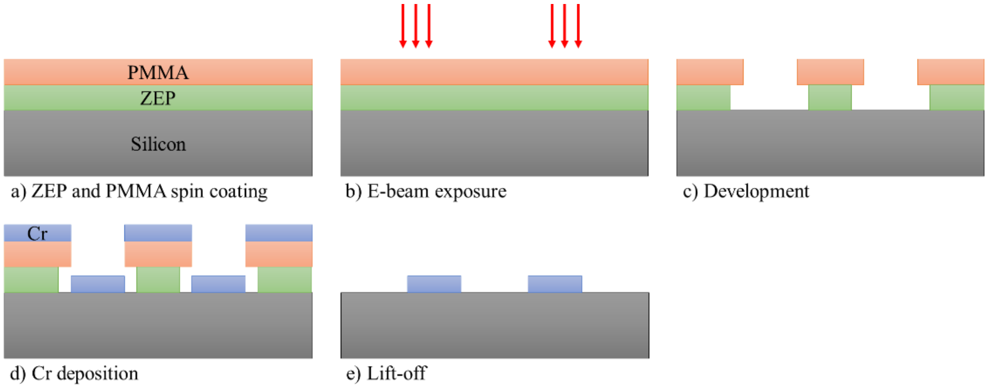

Fig. 4.14: Fabrication steps to pattern thick Cr structures.

To be able to have flexibility in etching depth, we chose to pattern a 150 nm thick Cr on silicon substrate using double layer e-beam resists with different sensitivity for subsequent lift-off. First, 270 nm ZEP-520A is spin-coated on silicon and baked at 150 °C for 10 min followed by 260 nm PMMA (6% dissolved in Anisole) spin-coating and 10 min baking at 130 °C. The total thickness of the bilayer resist is measured as 410 nm after intermixing, which is good enough to lift-off 150 nm metal film (Fig. 4.14a). Next, e-beam exposure is performed to define circular patterns using Raith 150^{TWO} system at 20 keV, and 0.2 nA beam current with an exposure dose of 100 $\mu C/cm^2$ (Fig. 4.14b). After that, the exposed pattern is developed in amyl acetate for 90 sec at room temperature which develops both ZEP and PMMA resists (Fig. 4.14c). In general, ZEP resists leaves a residual layer after development which may cause trouble for subsequent lift-off. Thus, a brief O_2 RIE is applied to the sample to etch away the residual layer under 20 W RF, 20 sccm, 20 mTorr etching parameters. Afterward, 150 nm Cr film is deposited by e-beam evaporation at 1 Å/s deposition rate to obtain sufficient uniformity (Fig. 4.14d). Next, lift-off is performed in anisole until both ZEP and PMMA layers are removed (Fig. 4.14e). Alternatively, the lift-off process can be carried out using a mixture of ZEP and PMMA where the resist sensitivity and undercut profile can be controlled by tuning the mixture ratio[46]. Finally, the non-switching Bosch process is carried out by tuning RF power and SF_6/C_4F_8 gas ratios.

First, the effect of RF power on sidewall profile is studied by keeping all other etching parameters constant as 20 sccm SF_6, 40 sccm C_4F_8, 1200 W ICP, 25 mTorr, 15 °C and varying RF power from 45 W to 120 W. The pressure is a critical parameter in the plasma etching. Generally, higher pressure leads to more reactive species (mainly free radicals) in the plasma to speed up the etching, and more collisions of the ions to decrease the etching anisotropy[47,48]. That is why in our first experiments, we tried to increase the pressure in order to promote the lateral etching for obtaining negatively tapered profile; however, it turned out that, for the range of RF powers fixed in this work (45 – 120 W), the ICP plasma failed to strike for pressures higher than 30 mTorr. Therefore, we fixed the pressure to 25 mTorr to ensure the stability of the ICP plasma.

As a reasonable starting point, we adopted the etching recipe that we reported previously, which gave a large positively tapered angle, except that we drastically increased the SF_6/C_4F_8 gas flow ratio (50% – 65% of SF_6 in the gas mixture) to promote etching and suppress sidewall passivation. However, as shown in Fig. 4.15 for 65% of SF_6 gas percentage in the C_4F_8/SF_6 gas mixture, a clear undercut profile was obtained instead. Therefore, we systematically studied the synergic effect of RF power and gas flow ratio. Other etching parameters, including pressure, ICP power, and substrate temperature, are not systematically investigated in this study. Generally, higher pressure results in more frequent collision of ions with the gas molecules and smaller bias voltage for a fixed RF power, which both decrease anisotropy; ICP power determines the plasma density and affects more the etching rate than the etching profile; and the substrate temperature affects the etching profile only when the volatility of the passivation layer varies significantly for the temperature range under study.

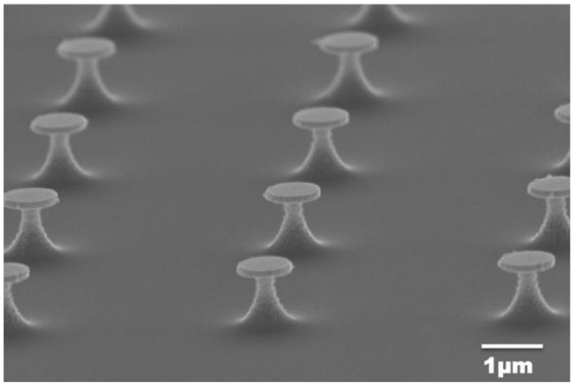

Fig. 4.15: SEM image of Si nanostructures with a pronounced undercut profile obtained with 65% of SF_6 gas in the C_4F_8/SF_6 gas flow mixture. The RF power, ICP power, and pressure are, respectively, 60 W, 1200 W, and 35 mTorr [42] (reprinted with permission from American Vacuum Society).

4.1.3.1 Effect of RF power

The effect of the RF power was studied at a fixed gas flow of $C_4F_8/SF_6 = 40/20$, an ICP power of 1200 W, and a pressure of 25 mTorr. Fig. 4.16 shows the Si etch rate and the sidewall taper angle as a function of the RF power. For the effect of RF power, on one hand, by increasing the RF power, the DC bias is increased, and ions are then more accelerated toward the sample, which promotes physical sputtering and more directional etch. On the other hand, higher RF power leads to larger dark space (sheath) thickness above the sample, and thus, the ions have to travel a longer distance to reach the sample surface with a higher chance of collision with gas molecules in the chamber, which promotes less directional etch[49]. The net effect is the tradeoff of those two competing effects. In this work, as seen in Fig. 4.16, we noticed a relatively small dependence of the Si etch rate on the RF power. Instead, the Si etch rate remained almost constant at around 280 nm/min for RF powers between 45 and 120 W. This indicates that here ions have little effect on the etching rate, since etching is mainly done by free radicals that are much more abundant (by 2–3 orders) than ions in typical plasma. This behavior was also observed by other researchers[43,50]. However, Fig. 4.16 shows that the sidewall taper angle decreased considerably from +3.1° at 45 W to -2.2° at 60 W, to saturate then at approximately -3° between 80 and 120 W. Above RF power of 80 W, the balance of the two competing effects of RF power as mentioned above led to a nearly constant -3° taper angle. As such, tuning the RF power alone did not give a large desired negative taper angle of close to -10° (Fig. 4.17).

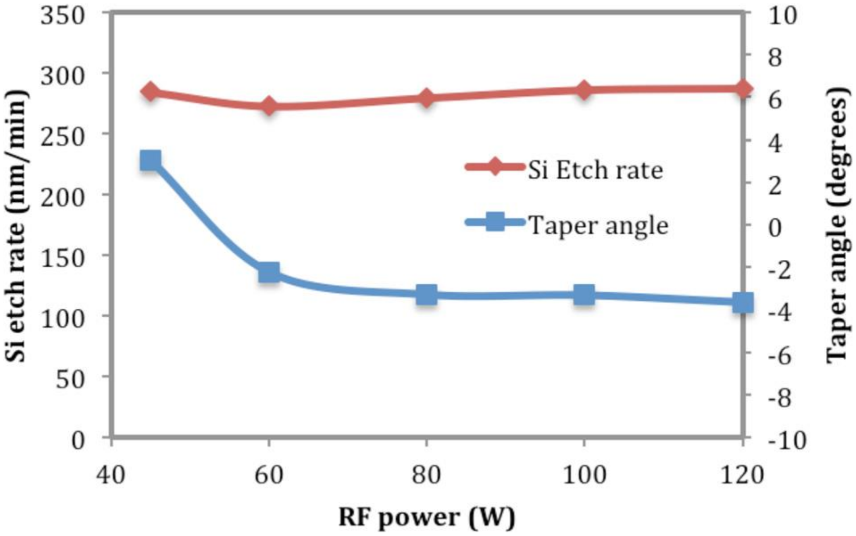

Fig. 4.16: Si etch rate and taper angle as a function of the RF power[42] (reprinted with permission from American Vacuum Society).

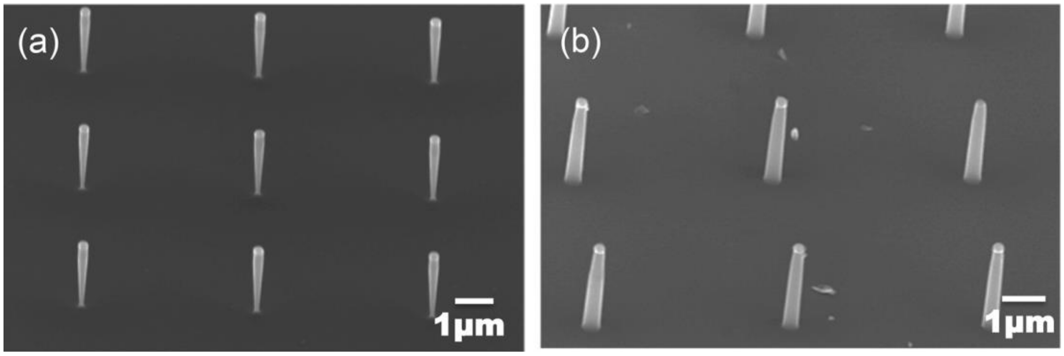

Fig. 4.17: SEM image of 300 nm diameter Si structures obtained at 33% of SF_6 (C_4F_8/SF_6=40/20) and RF power of, respectively, (a) 45 W (taper angle of +3°) and (b) 60 W (taper angle of -2.2°)**[42]** (reprinted with permission from American Vacuum Society).

4.1.3.2 Effect of SF_6 gas flow percentage

As mentioned above, in the C_4F_8/SF_6 gas mixture, the SF_6 gas is destined to etch the Si whereas the C_4F_8 is used as passivation to protect the Si structure sidewalls to achieve good control of the etching profile[51,52]. Indeed, the SF_6 percentage can impact the structure sidewalls from a positive to a negative profile[48]. Therefore, the SF_6 gas flow percentage represents a key parameter to achieve a good control of the sidewalls profile. However, all the plasma etching parameters should be well optimized collectively to avoid the undercut profile usually obtained by only increasing the SF_6 gas flow, as shown in the example presented in Fig. 4.15.

The effect of the C_4F_8/SF_6 gas flow ratio on the etch rate and sidewall taper angle was studied at an optimal RF power of 60 W, an ICP power of 1200 W, and a pressure of 25 mTorr. The total gas flow is fixed to 60 sccm. To avoid dominance by chemical etching that promotes an undesirable undercut profile, a lower percentage of SF_6 (i.e., <50% of the total gas flow) than C_4F_8 gas was always used. Fig. 4.18 shows the variation of the Si etch rate and the sidewall taper angle as a function of the SF_6 gas flow percentage in the mixture.

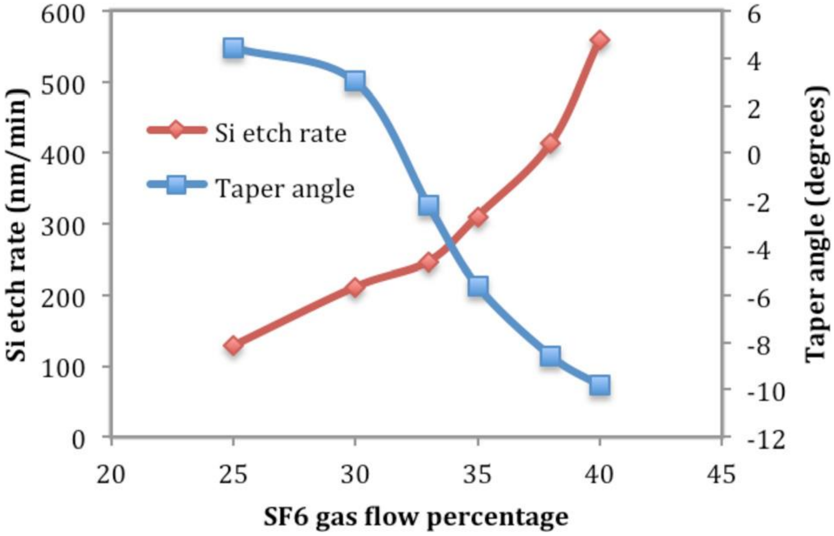

Fig. 4.18: Si etch rate and tapered angle variation as function of the SF_6 gas flow percentage in the mixture[42] (reprinted with permission from American Vacuum Society).

As seen, by slightly increasing the SF_6 gas flow from 20% (C_4F_8/SF_6 = 48/12) to 40% (C_4F_8/SF_6 = 36/24), the etching rate is increased from 128 to 558 nm/min, and the taper angle is considerably decreased from 4.4° to -9.7°. The balancing point between etching and passivation to give a vertical sidewall profile was obtained at 33 SF_6 gas flow percentage. Examples of unique Si structures etched at different SF_6 gas flow percentages varying from

25% to 40% are shown in Fig. 4.19. A low magnification SEM image of an array of Si nanostructures obtained at 40% of SF_6 with a large negative taper angle of -9.7° is shown in Fig. 4.20. To the best of our knowledge, this is the first time such a straight (not curved) and large negative taper angle is achieved by dry etching.

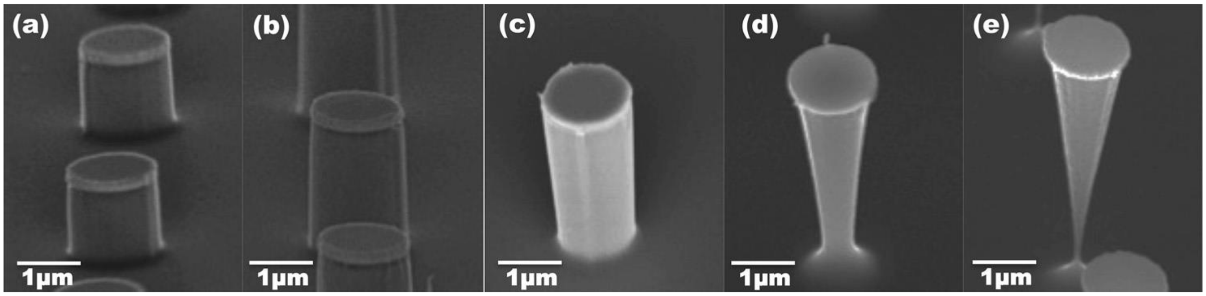

Fig. 4.19: SEM images of Si structures (Cr mask still on, mask diameter 1.2 μm) as a function of SF_6 gas flow percentage in the C_4F_8/SF_6 mixture with respective taper angles: (a) 25% of SF_6 (4.4°), (b) 30% of SF6 (3°), (c) 33% of SF6 (-4.6°), (d) 38% of SF_6 (-8.5°), and (e) 40% of SF6 (-9.7°)[42] (reprinted with permission from American Vacuum Society).

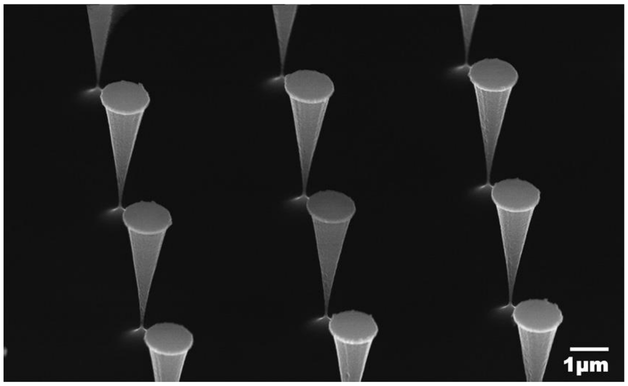

Fig. 4.20: SEM image of Si structures (Cr mask still on, mask diameter 1.2 μm) obtained at 40% of SF_6 and RF power of 60 W, showing a large negative taper angle of -9.7° [42] (reprinted with permission from American Vacuum Society).

As mentioned earlier, the pillars with negative taper angle can be benefited for special AFMs for sidewall imaging. Etching with positive taper angle will be discussed throughout the fabrication steps in the following chapter. In the next section, another important etching term, loading effect, will be reviewed.

4.1.4 Loading effect in RIE

In reactive ion etching, the etching rate depends on supply rate of highly energetic and reactive species produced from a gas or mixture of gasses, so the etching rate will decrease if the supply rate decreases. In other words, when the quantity of material to be etched is increased, the etch rate will decrease while keeping the gas flow rate, pressure and other conditions the same. This effect is known as the *loading effect*. There are two main types of loading effect: macroloading and microloading. *The macroloading effect* is defined as a decrease in etch rate while increasing overall substrate area to be etched. Thus, the etch rate may not be the same for two different designs and should be re-calibrated for different designs and size of samples when working on features with low tolerance. *Microloading effect* is observed when there is variation in local pattern density or pattern size. For example, the same feature will be etched slower if they are densely located compared to an individual isolated feature. Larger openings will result in a higher etching rate because more free radicals will be available. On the other hand, etching gas and product will have difficulty to get in and out of the narrower areas that slows down the etching rate. A schematic illustration of the microloading is presented in Fig. 4.21.

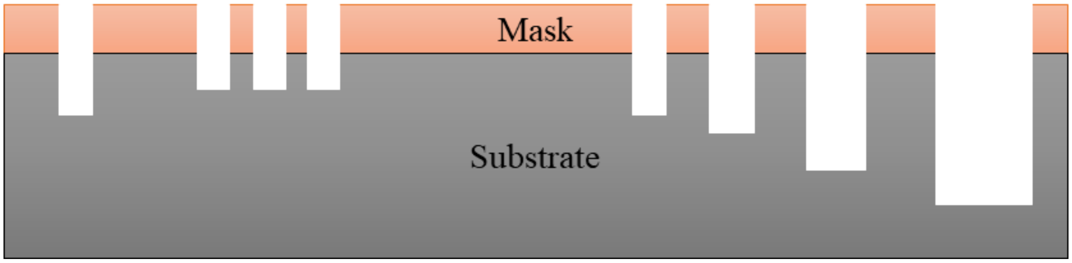

Fig. 4.21: Schematic illustration of the microloading effect.

The loading effect is critical in AFM tip fabrication because the holder, cantilever and the tip have a large variation in size. Therefore, one needs to consider the loading effect to be able to get successful results out of fabrication. Moreover, some of the reactive ion etchers operate only if there is a sample carrier wafer. The etch rate changes significantly by the type of the carrier wafer. For instance, glass carrier wafers would give higher etch rates than silicon when etching silicon due to macroloading effect. However, glass carriers are not compatible in some equipment because of their transparency where photodetector cannot detect the carrier wafer, and thus the etcher would not operate.

4.2 Using photoresist only for AFM tip and cantilever fabrication

Spin-coating is a fast and cost-efficient process compared to hard mask deposition or growing, which will still require a spin-coating for mask patterning. To reduce the number of the processing steps and cost for AFM tip fabrication, we developed a process where we use only photoresist as mask (instead of using Cr as mask for tip part and resist as mask for cantilever part, as presented in Section 4.1). The backside and complete fabrication of AFM tip is already demonstrated in the previous section. Therefore, here we focus on the front side fabrication on a bare silicon wafer. A summary of the fabrication steps to fabricate the front side of the AFM tip is presented in Fig 4.22.

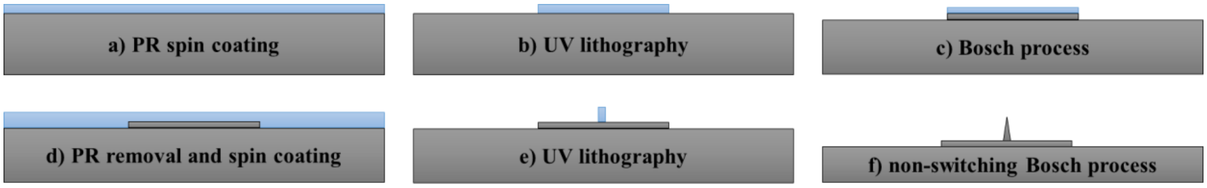

Fig. 4.22: Schematic representation of process steps for front side of AFM tip fabrication using photoresist only.

First, the silicon substrate is cleaned, and nLOF 2035 negative photoresist is spin-coated at 4000 rpm for 40 sec followed by 110 °C baking for 1 min on a hotplate (Fig. 4.22a). Next, UV exposure is performed under 350 mJ/cm^2 exposure dose to define the cantilever pattern. The resist requires post-exposure bake for complete exposure as it is a type of chemically amplified photoresist; thus, it is baked at 110 °C for 1 min. After that, the resist is developed in AZ 300 MIF developer and hard baked at 110 °C for 1 min (Fig. 4.22b). An optical image of the cantilever array is displayed in Fig. 4.23.

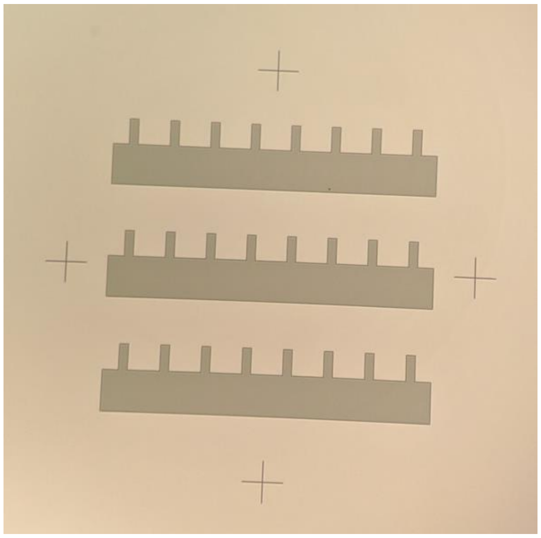

Fig. 4.23: Optical microscope image of cantilever array after development.

Right after hard baking, the cantilever pattern is transferred into silicon by DRIE using 9 cycles of Bosch process that etches about 3.6 µm (Fig. 4.22c). Afterward, remained photoresist is stripped in acetone, and another layer of nLOF 2035 is spin-coated on the sample under the same conditions (Fig. 4.22d). Since the sample is already patterned with micron-scale features, the resist thickness will not be uniform on the pattern area. An optical microscope image of the pattern after spin-coating is shown in Fig. 4.24.

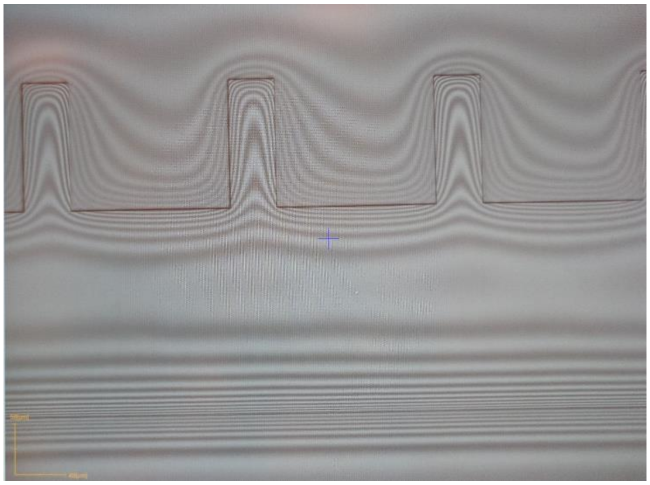

Fig. 4.24: Optical microscope image of cantilever array after spin-coating on patterned sample.

Although the photoresist is not uniform, the thickness gradient is consistent among the cantilevers. For AFM tip, only a small area of ≤1 µm is needed; therefore, the process can still be utilized to obtain consistent results. Next, UV lithography is carried out to define the tip pattern under the same parameters except the exposure dose is doubled because higher dose is required to expose small isolated patterns (Fig. 4.22e). Even though the resolution limit of the instrument is reported as 1 µm, smaller pattern size can still be expected because resolution is a measure of pattern density. One can expose isolated, separate line or dot structure to achieve smaller pattern size than resolution capability. The optical microscope images after second step patterning are shown in Fig. 4.25. Here, some large squares were exposed to make sure the exposure and development processes are successful while working on small features.

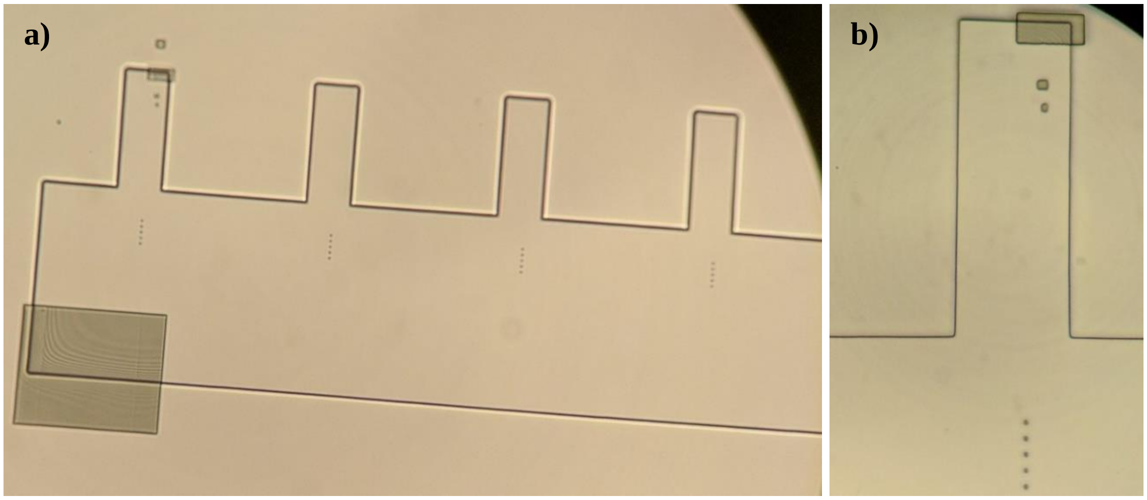

Fig. 4.25: Optical microscope images after second step patterning. (a) an overview of the patterns; (b) close view of one of the cantilevers.

Finally, the resist pattern is transferred in silicon using non-switching Bosch process under 20 W RF, 1200 W ICP, 10mTorr, 15 °C, 40 sccm C_4F_8 and 20 sccm SF_6 for 20 min. It is expected to get almost vertical profile after the etching; however, pillars having a positive sidewall profile with 3.6° taper angle were obtained as shown in Fig. 4.26.

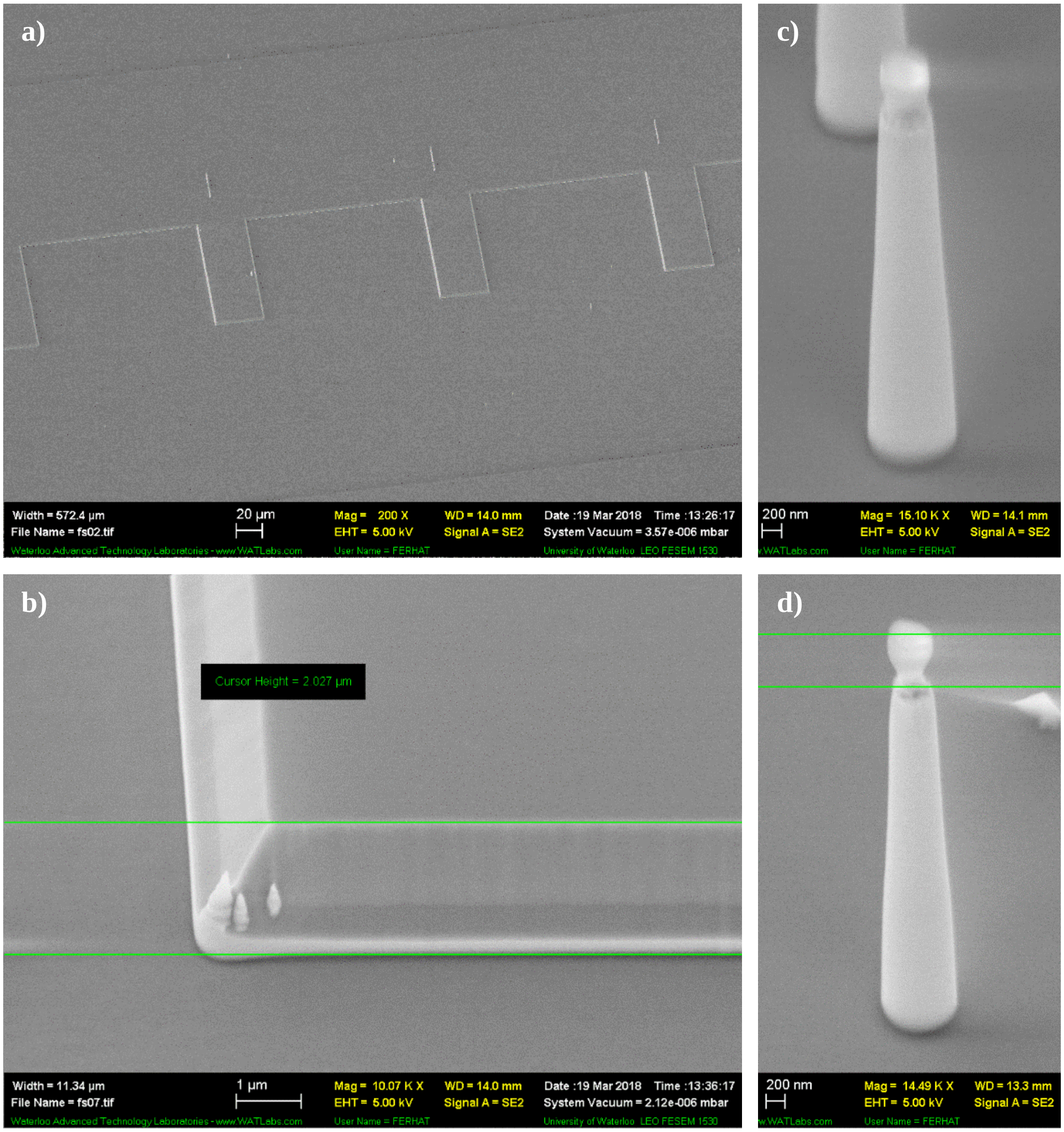

Fig. 4.26: SEM images of fabricated AFM tips using photoresist. (a) cantilever array; (b) close view of the edge of the cantilever; (c) tip with diameter of 545 nm; (d) tip with diameter of 390 nm.

The etching resulted in 2.86 µm thick cantilever and 4.8 µm tall pillars with 3.6° taper angle. Such high taper angle is obtained because the photoresist was eroded on the sides throughout the etching. The photomask diameter matches the top of the pillar diameter in various sized pillars which also confirmed that the etching profile is determined by photoresist erosion.

The same erosion is also observed in cantilever pattern (Fig. 4.26c). Moreover, base diameters of 937 nm and 770 nm (Fig. 4.26b and d, respectively) show that sub-micron structures can be obtained by photolithography. The original thickness of the photoresist was measured as 2.4 µm, and around 800 nm resist is remaining which means 2.4 µm nLOF 2035 baked at 110 °C for 1 min is enough to etch 7.2 µm silicon under this recipe. As well, a sharper profile for AFM tip would be obtained if etching was continued. Pillars with smaller diameters was also designed at the cantilever end; however, those structures were removed during the development which is probably due to the inadequate exposure dose.

In this work our goal was a proof of the concept, so further experiments were not carried out. A summary of the process steps using photoresist only is illustrated in Fig. 4.27. In this process flow, first backside is patterned by AZ 4620 and subsequent DRIE. Next, the wafer is mounted on a transparent carrier such as a glass wafer to be able to do backside alignment and protect the sample against possible damages during spin-coating and handling processes. After that, the front side patterning is carried out in a similar process discussed above.

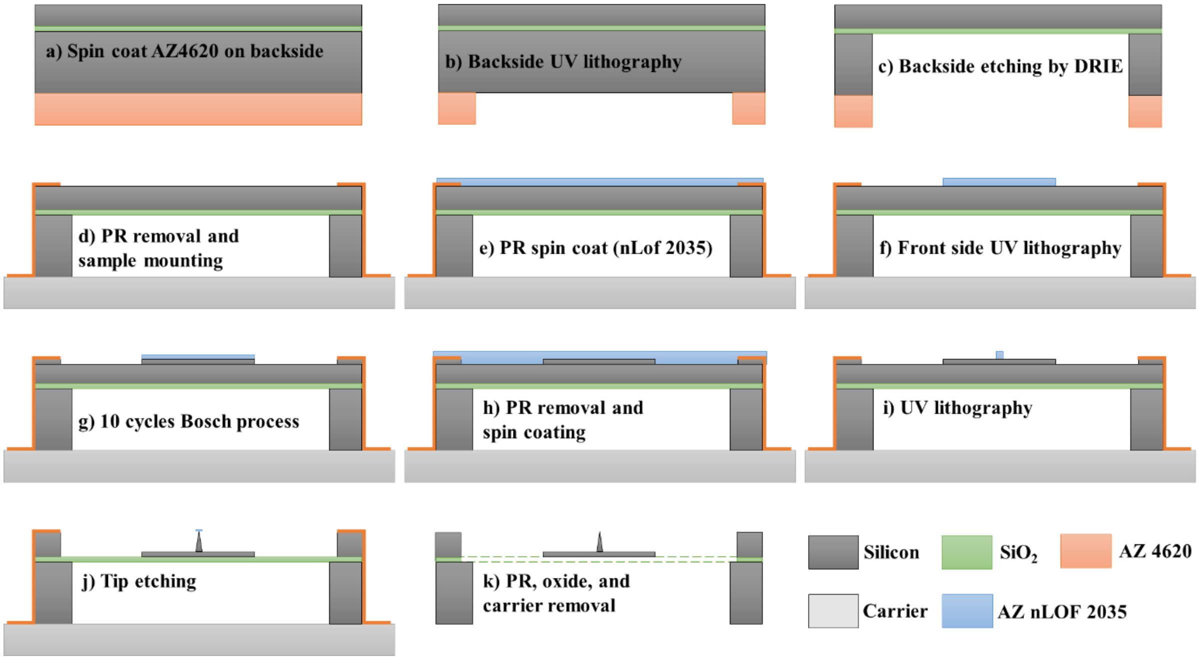

Fig. 4.27: Schematic representation of process steps for AFM tip fabrication using photoresist only.

Chapter 5

Fabrication of high aspect ratio (HAR) atomic force microscopy (AFM) probes by one step e-beam lithography

In this chapter, our one-step e-beam lithography method for HAR AFM tip fabrication, and performance of fabricated tips will be introduced. Also, some challenges and possible solutions regarding the fabrication method will be discussed.

We have developed processes for batch fabrication of AFM tip using UV lithography discussed in previous chapter. Although the processes are promising, higher resolution patterning is required for better control in tip shape and size. In previously discussed method, the UV lithography step simply can be replaced by e-beam lithography to define the tip pattern. However, there are two lithography steps required to define cantilever and the tip separately. Here, we developed a systematic process to define both cantilever and the tip pattern in one lithography step. The process involves stack of two e-beam resists and two metal films as hard masks. We first worked on a bare silicon wafer, instead of SOI (silicon on insulator) wafer, to develop the fabrication process for the cantilever and tip parts.

5.1 Frontside fabrication

Stack of resists with different sensitivities can be used to form 2-step structures as shown in Fig. 4.14 in case of lift-off. However, electron-beam resists are usually not good enough for several microns of silicon etching required for AFM tip fabrication. Therefore, we patterned a metal film as a hard mask in this process. As e-beam resist, we selected polystyrene and PMMA resists. The fabrication process steps are illustrated in Fig. 5.1.

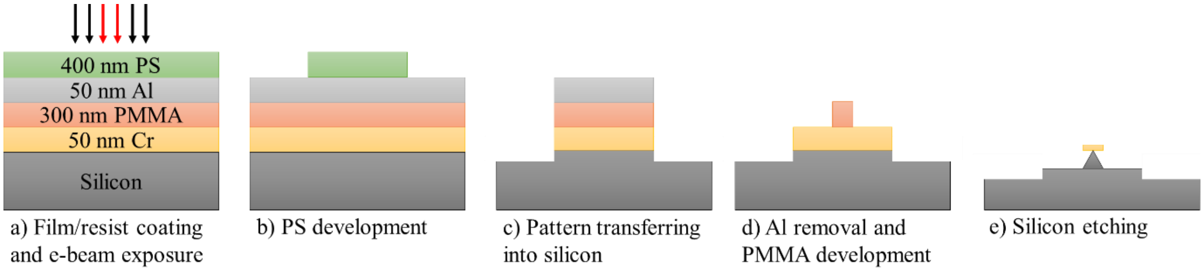

Fig. 5.1: A schematic representation of AFM probe fabrication steps involving only one e-beam exposure step.

First, 50 nm Cr is deposited as hard mask for tip pattern at 1 Å/s deposition rate by e-beam evaporation. Next, 300 nm PMMA is spin-coated at 4000 rpm and baked at 180 °C for 20 min where 6% PMMA is dissolved in anisole to obtain target thickness at 4000 rpm. After that, 50 nm Al is deposited at 1 Å/s deposition rate by e-beam evaporator, followed by 400 nm polystyrene (PS) spin-coated at 4000 rpm and baked at 100 °C for 10 min where 5% 260 kg/mol PS dissolved in xylene is used to obtain the target thickness. The PS is a negative e-beam resist and defines the cantilever pattern here, and Al is used as an isolation layer between PS and PMMA. Although PS can be dissolved in various solvents, PMMA is also dissolved in these solvents. To avoid xylene from attacking exposed PMMA (xylene can dissolve exposed PMMA, but not unexposed one), here, a protection layer is required. Furthermore, PS is baked at a low temperature of 100 °C to avoid reflow of PMMA. On the other hand, PMMA is a positive e-beam resist but can be crosslinked if the exposure dose is high enough and, as such, becomes a negative e-beam resist. The process is continued by e-beam exposure step under the following exposure parameters: 20 keV acceleration voltage, 30 µm aperture, 150 µC/cm^2 exposure dose for PS for 30 µm × 100 µm cantilever, and 15000 µC/cm^2 exposure dose for PMMA (here negative tone) for the 350 nm and 550 nm diameter tips (Fig. 5.1a). After that, PS is developed in xylene for 90 sec at room temperature (Fig. 5.1b). The PS pattern is then transferred into all the layers down to silicon under following etching conditions, respectively (Fig. 5.1c).

3 min Al + PMMA etching: 50 sccm BCl_3, 1 mTorr, 300 W RF, 800 W ICP, 22 °C

90 sec Cr etching: 42 sccm Cl_2, 8 sccm O_2, 12 mTorr, 10 W RF, 1200 W ICP, 50 °C

10 min Si etching: 100 sccm SF_6, 25 mTorr, 60 W RF, 1000 W ICP, 15 °C

Combination of three etching steps consumes PS and some of Al; remaining Al is etched in HF (1:100 HF:H_2O) for 1 min. Here, HF is preferred over PAN (Phosphoric, Acetic, and Nitric acids) etchant because acetic acid dissolves PMMA. Next, PMMA is developed in anisole for 90 sec at room temperature, and PMMA pattern is transferred into Cr using the above recipe (Fig. 5.1d). Finally, non-switching Bosch process is performed for 10 min under 20 W RF, 1200 W ICP, 10mTorr, 15 °C, 40 sccm C_4F_8 and 20 sccm SF_6 etching conditions (Fig. 5.1e). We kept the remaining Cr mask to see if it is enough to achieve our goal. The results are shown in Fig. 5.2.

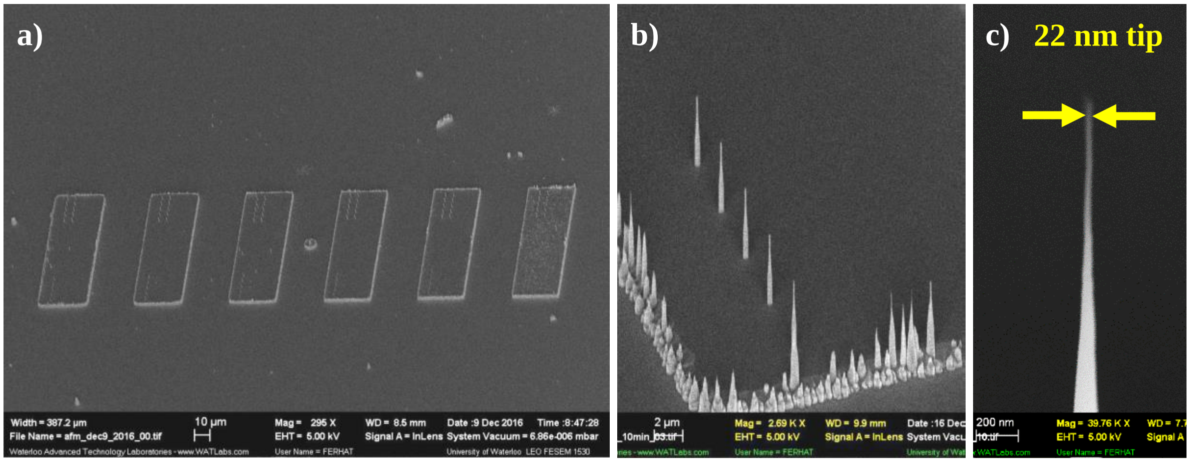

Fig. 5.2: SEM images of fabricated tips, (a) overview of cantilever array; (b) close view of a cantilever edge; (c) close view of a tip with 22 nm diameter.

The cantilever array is shown in Fig. 5.2a, and a close view of it in Fig. 5.2.b with a measured thickness of 2.7 µm. Furthermore, the etching resulted in 7 µm length and 22 nm diameter of tip where the tip has a satisfactory aspect ratio and profile. However, there are randomly formed pillars all around the cantilever edge after the second etching step. Although the reason is not apparent, we think that some PMMA is crosslinked at the edge during reactive ion etching steps and was not fully developed in subsequent steps. Therefore, we later on performed 2 min additional O_2 RIE step (20 sccm O_2, 20 W RF, 50 mTorr) to isotopically etch the PMMA while Al film is still on top of it. Finally, non-switching Bosch process is carried out for 10 min to define pillars up to 1 µm diameter under 42 sccm C_4F_8 and 18 sccm SF_6 gas flows. Here the C_4F_8 gas ratio is increased to obtain a higher positive taper angle. Furthermore, the etch rate will be slower because of higher passivation gas (C_4F_8) flow and lower etching gas (SF_6) flow. The results are shown in Fig. 5.3, 5.4 and 5.5.

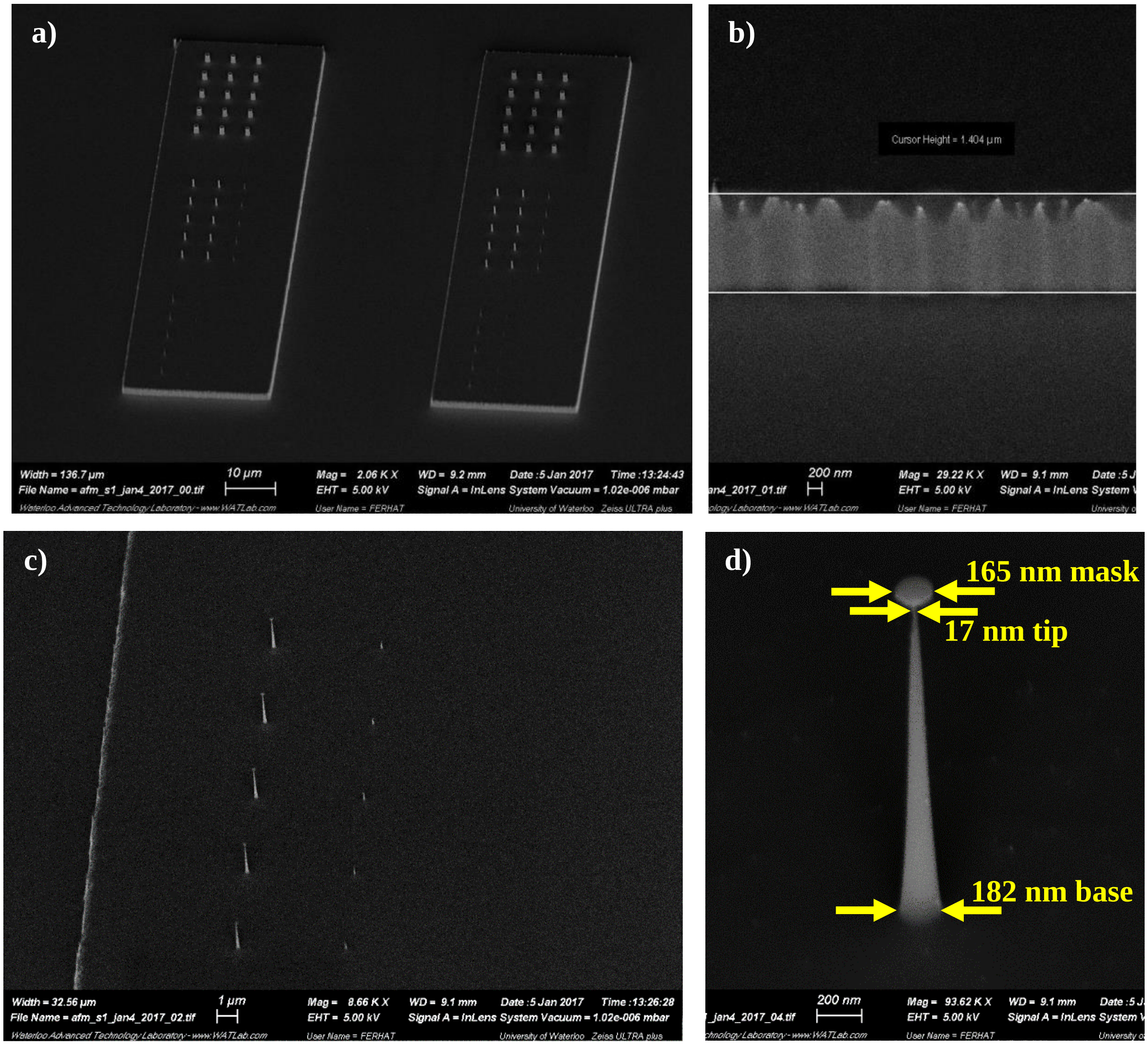

Fig. 5.3: SEM images of (a) 2 cantilevers with various tips etched for 10 min under 42 sccm C_4F_8 and 18 sccm SF_6, 20 W RF, 1200 W ICP, 10mTorr, 15 °C; (b) close view of cantilever end; (c) tip array on cantilever; (d) close view of one of the tips.

Our process worked as it can be seen in Fig. 5.3; the edges of the cantilever is smoother and free from random pillars. Additionally, tips with large diameter resulted in larger tip apex, but etching by 165 nm diameter Cr mask resulted in tips with the length of 2 µm and an apex diameter of only 17 nm. The shape and tip diameter showed promising result, but the height of the tip may not be enough as an AFM tip. Too long etching would erode the thinnest point of the tip, so a taller tip would not be obtained. Therefore, the etching time is only moderately increased to 30 min to obtain taller tips with sharp tip apex. The etching results for 30 min are shown in Fig. 5.4.

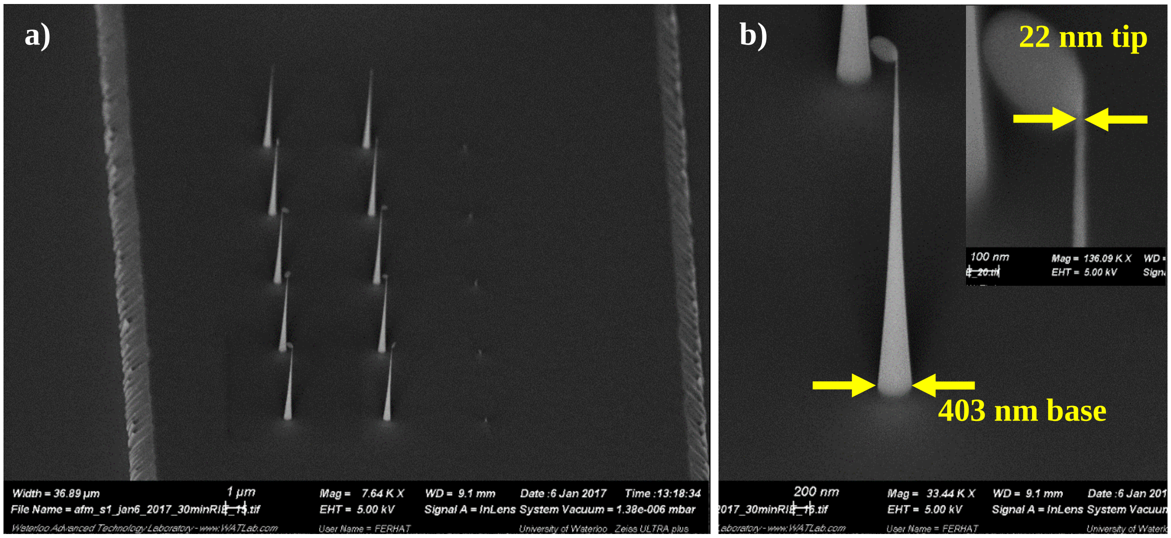

Fig. 5.4: SEM images of (a) tip array on cantilever etched for 30 min under 42 sccm C_4F_8 and 18 sccm SF_6, 20 W RF, 1200 W ICP, 10mTorr, 15 °C; (b) close view of one of the tips (inset: close view of tip apex).

The etching resulted in 4.92 tall, 403 nm base diameter and 22 nm tip apex diameter tips while maintaining smooth cantilever edge. The tip is longer, and the etching is uniform among the cantilevers and pillars. The overall tip profile is suitable to be a HAR AFM tip, and the tip apex diameter can be further sharpened with oxidation sharpening.

Further experiments were performed to fabricate tips with larger base while maintaining the tip apex diameter. Therefore, larger tips were etched for 30 min under the same etching conditions except for the gas flows of 44 sccm C_4F_8 and 16 sccm SF_6. It is expected to have larger taper angle and slower etch rate. The etching results are shown in Fig. 5.5.

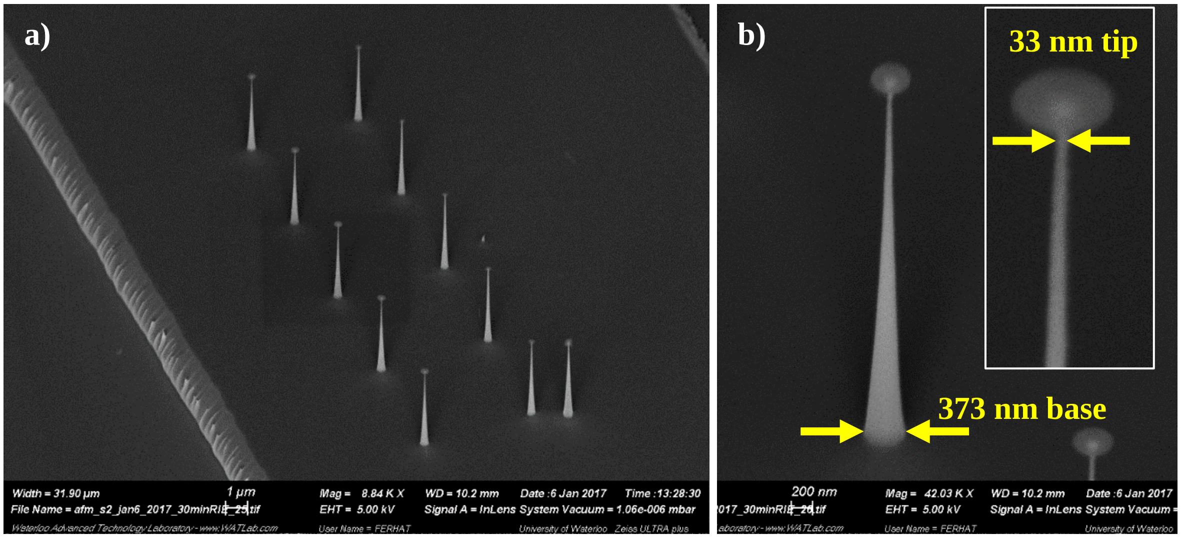

Fig. 5.5: SEM images of (a) tip array on cantilever etched for 30 min under 44 sccm C_4F_8 and 16 sccm SF_6, 20 W RF, 1200 W ICP, 10mTorr, 15 °C; (b) close view of one of the tips (inset: close view of tip apex).

The etching resulted in a shorter tip with smaller base diameter and larger tip apex diameter of 4.75 µm, 373nm, and 33 nm respectively. Since etching gas ratio is decreased and the passivation gas ratio is increased, the etching rate decreased. Thus, it is expected to have shorter tip at the end for the same etching duration. Because of the same reason, the base diameter is smaller, and tip apex is larger. Longer etching would result in a taller tip with smaller apex and larger base diameters. Overall the tip dimensions are great while maintaining clean etching without random pillar formation at the edges of the cantilever.

As can be seen from Fig. 5.5 and 5.6, the Cr masks are almost entirely etched away under given etching parameters. Therefore, it can be concluded that 50 nm Cr is enough to etch about 5 µm Si with these recipes; to be able to etch longer tips, thicker Cr mask is required. However, the etching selectivity between PMMA and Cr is quite low where PMMA has poor dry etching resistance. Coating thicker PMMA will result in lower resolution structures, so here we studied Cr_2O_3 mask to replace Cr where Cr_2O_3 has similar selectivity to silicon etching and better selectivity to polymers. Therefore, it suits well to our process. In the next section, Cr_2O_3 mask will be discussed where polystyrene is chosen for comparison because it has better dry etching resistance than PMMA that makes the experiments easier.

5.1.1 Choice of tip mask material

This section is reprinted with permission from Ref. [53]*. Copyright (2018) American Vacuum Society:*

> Aydinoglu, F., Saffih, F., Dey, R.K. and Cui, B., 2017. Chromium oxide as a hard mask material better than metallic chromium. *Journal of Vacuum Science & Technology B, Nanotechnology and Microelectronics: Materials, Processing, Measurement, and Phenomena*, *35*(6), p.06GB01.

Thin film plasma etching is one of the most essential processes in semiconductor device fabrication for both industrial and R&D applications. Choice of the etching mask material is often as important as the etching recipe itself because it will determine the final structure's morphology such as sidewall smoothness, taper angle, and feature resolution. Poor etching masks can cause rough or tapered sidewalls because of mask erosion[54]. For a given etching selectivity between the mask and the material to be etched, higher etching depth requires thicker mask, but thicker mask structure is more difficult to fabricate with high resolution[55]. Electron-beam resist and photoresist are apparently the most popular mask material. One of the well-known limitations for high-resolution lithography using thick resist is pattern collapse caused by capillary force during rinsing liquid drying and after development. That is, to achieve very high-resolution lithography, the polymer resist should be very thin such as 10–30 nm, leading to a great challenge in pattern-transferring into the substrate because polymer resist usually has poor etching resistance[56]. An apparent approach to greatly increase resists' resistance to dry etching is to incorporate metal into organic polymer resists. One example is poly(sodium 4-styrenesulfonate), which is a water-soluble and developable negative tone resist containing the metal sodium[57]. A second example is organometallic metal carbonyl polymer, cyclopentadienylcarbonyldiphenylphosphinobutanoyliron, which contains metal iron[58]. Alternatively, metal Cr can be incorporated physically into polystyrene (PS) resist using cothermal evaporation[59].

A more popular approach to etch deep into the substrate is to use conventional polymer resist combined with an intermediate hard etching mask, where the intermediate hard mask is first patterned by lithography and pattern transferring, and then the substrate or sublayer is dry etched using the patterned hard mask structure as etching mask. Cr is probably the most widely utilized hard mask material for plasma etching because of its high selectivity to silicon and its compound when using fluorine or chlorine based etching chemistry. Use of Cr film was studied since 1976[60,61,62,63], and its applications include photomask as the opaque layer, etching mask in semiconductor device fabrication, and electrodes for thin film transistor liquid crystal displays and field emission displays (FEDs)[64,65,66,67]. Pattern transferring from the resist structure into Cr can be carried out either by lift-off or direct etching techniques using the resist as mask. Whereas lift-off is very popular for R&D because it patterns metals like Cr efficiently, it is rarely used by industry because of its low yield. In the lift-off technique, the pattern edges are often not well defined, and metal flakes in the lift-off solution may stick onto other parts of the sample. In the direct etching pattern transferring method, wet etching or dry plasma etching can be performed, with dry plasma etching always preferred for high-resolution nanofabrication. One disadvantage of the dry etching process is usually the poor etching selectivity between resist materials and metals. This is particularly true when Cr is used as the intermediate etching mask because etching of Cr requires the addition of oxygen to the chlorine gas, and oxygen etches very fast the polymer resist material.

In this study, we will show that chromium oxide (Cr_2O_3) mask can achieve higher etching selectivity to resist than Cr does, and thus is easier to pattern by lithography followed by direct dry etching pattern transfer; and at the same time, for further pattern transferring into the substrate notably silicon, the patterned Cr_2O_3 is as efficient as metallic Cr as the intermediate hard mask material. Here, higher selectivity of Cr_2O_3 to resist is obtained because Cr_2O_3 contains oxygen by itself that promotes the formation of the volatile etching product CrO_2Cl_2, and hence less oxygen is needed that in turn reduces the resist etching rate.

Moreover, as it was discovered that Al_2O_3 is superior to Al as etching mask because it is insulating, we expect the same conclusion holds true for Cr_2O_3 as compared to Cr[55].

To determine the etching rates of Cr and Cr_2O_3, over 300 nm thick of both materials were deposited on Si substrates using electron beam evaporator with Cr or Cr_2O_3 as source material. The film samples were then partially masked by a thick photoresist, and dry etching was carried out using Oxford 380 inductively coupled plasma-reactive ion etching (ICP-RIE) system. Afterward, the remaining resist was stripped away, and the resulted step heights were measured using a Veeco Dimension 3100 atomic force microscope. For etching Cr or Cr_2O_3, the chamber pressure, RF bias power, ICP coil power, total gas flow of Cl_2/O_2, and the chamber temperature were kept constant as 12 mTorr, 10 W, 1200 W, 50 sccm, and 50 °C, respectively. While keeping the total gas flow at 50 sccm, the ratio between Cl_2 and O_2 was changed gradually to study the effect of O_2 percentage on the etching rate and selectivity for both materials.

To study the etching selectivity between Cr or its oxide and a polymer resist, we took PS as an example. Negative resist is preferred for this study because it is more commonly used for pattern transferring by direct etching to fabricate protruded structures (to fabricate recessed structures by direct etching, positive resist is preferred). PS is a very versatile negative resist offering tunable sensitivity and contrast by merely varying its molecular weight[68,69]. PS has a dry etching rate very close to that of ZEP-520A (positive) resist and is two to three times slower than PMMA because PMMA is a linear polymer with higher oxygen content and higher radiation yield of chain scission reactions, whereas ZEP-520A has a stable phenyl group in its chemical structure[70,71,72]. PS film of 400 nm thickness was coated on a silicon wafer using the spin-coating method.

Last, to demonstrate the advantage of Cr_2O_3 over Cr as an intermediate hard etching mask, as shown in Fig. 5.6, we coated Cr or its oxide film on silicon wafer, then carried out electron beam lithography using PS as resist, followed by etching Cr or its oxide using Cl_2/O_2 ICP-

RIE, and finally conducted Si ICP-RIE using a non-switching pseudo-Bosch process (Oxford 380 ICP-RIE system, 10 mTorr, 20 W RF power, 1200 W ICP power, 38 sccm C_4F_8, 22 sccm SF_6, 15 °C, etches Si 390 nm/min). This non-switching ICP-RIE process using SF_6 and C_4F_8 gas is very versatile, offering a broadly tunable sidewall taper angle from large positive (cone structure) to large negative (inverse cone structure)[39,42,55].

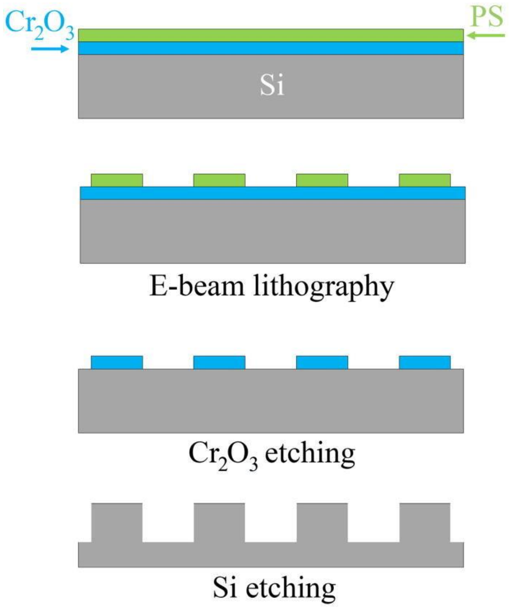

Fig. 5.6: Fabrication of silicon nanostructures, here using Cr_2O_3 as an intermediate hard etching mask[53]. (reprinted with permission from American Vacuum Society).

Unlike sputter deposition for which the film composition is always very close to the target material composition, evaporation often does not maintain the chemical composition of the source material when depositing compound materials particularly alloys. This is caused by the different vapor pressures of each element in the compound at the evaporation temperature. It is therefore essential to characterize the film composition of chromium oxide. As shown in Fig. 5.7, the energy-dispersive x-ray spectroscopy (EDX) measurement indicates that the evaporated film coated on a silicon substrate contains 60.4 at. % O and 39.6 at. % Cr, which is very close to the 3:2 atomic ratio in stoichiometric Cr_2O_3.

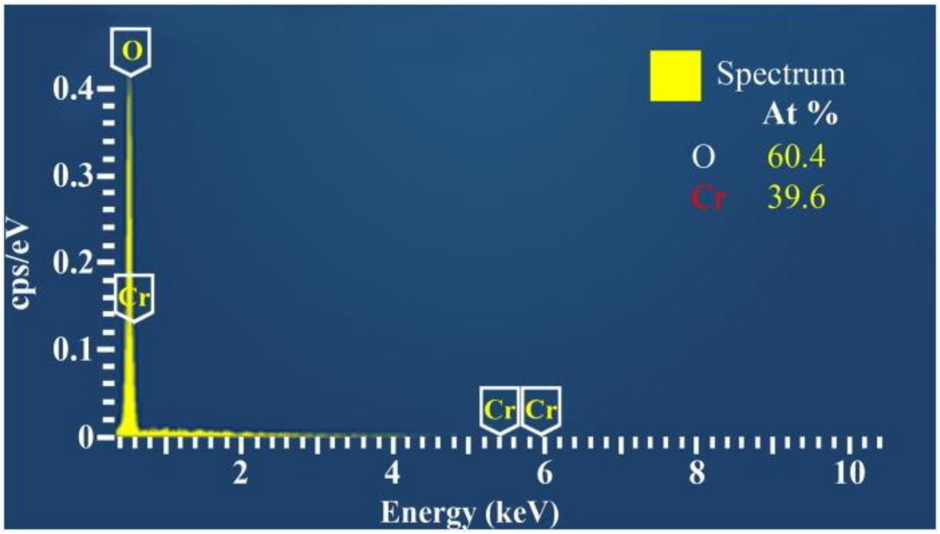

Fig. 5.7: EDX spectrum of e-beam evaporated chromium oxide film (Cr_2O_3 as source material) on a silicon substrate, with 10 keV incident electron energy (Si and C peaks are excluded from the spectrum)[53]. (reprinted with permission from American Vacuum Society).

As standard photomask materials, respectively, for light blocking (Cr) and antireflection (Cr_2O_3), the plasma etching of Cr and Cr_2O_3 has been well established. Using Cl-containing gas (e.g., Cl_2 and CCl_4) and oxygen, the reactions are: $Cr + 2O^* + 2Cl^* \rightarrow CrO_2Cl_2$ (boiling point 117 °C, volatile at room temperature), and $CrO_x + (2 - x)O^* + 2Cl^* \rightarrow CrO_2Cl_2$; here O* and Cl* are neutral free radicals generated in the plasma[73,74]. Addition of oxygen to the chlorine-containing gas is essential because otherwise the formed $CrCl_n$ ($n = 1 - 3$) has a very low vapor pressure at room temperature (melting point of $CrCl_3$ is 1152 °C and boiling/decomposition point ∼1300 °C). Therefore, the amount of O_2 and Cl_2 or CCl_4 is essential to determine the etching rate of Cr and Cr_2O_3. Unfortunately, adding oxygen also considerably boosts the etching of the polymer resist, leading to a great reduction of the etching selectivity between resist and Cr.

The etching rates with varying O_2 flow rates at a fixed total flow of $Cl_2 + O_2 \equiv 50$ sccm for Cr, Cr_2O_3, and PS are listed in Table 5-1, as well as illustrated in Fig. 5.8 as a function of O_2 flow rate. As expected, decreasing O_2 flow from 8 to 3 sccm decreased the etching rate of PS from 45 to 31.5 nm/min, and the etching rate of Cr from 70 to 44 nm/min. However, the etching rate of Cr_2O_3 was found to be constant at 130 nm/min. As a result, 10 nm PS resist would be enough to mask the etching of approximately 40 nm Cr_2O_3 film using the 47/3 Cl_2/O_2 gas flow ratio; whereas 10 nm PS can sustain the etching of only 17 nm Cr using the optimal 45/5 Cl_2/O_2 gas flow ratio. This difference is caused by the fact that Cr_2O_3 contains oxygen by itself to promote fast etching even with low O_2 gas flow. This mechanism is somewhat similar to the etching of Si and SiO_2 using CHF_3 or CF_4/H_2 gas, which can etch SiO_2 much faster than Si because the former contains oxygen to increase the F/C ratio in the plasma (as O in the oxide reacts and helps remove species like $CF_{2,3}$ and H to form volatile CO and H_2O).

Gas flow of Cl_2 and O_2	**Material**	**Etch rate (nm/min)**
42 sccm Cl_2, 8 sccm O_2	Cr	70
	Cr_2O_3	130
	PS	45
45 sccm Cl_2, 5 sccm O_2	Cr	60
	Cr_2O_3	130
	PS	35
47 sccm Cl_2, 3 sccm O_2	Cr	44
	Cr_2O_3	130
	PS	31.5
50 sccm Cl_2, 0 sccm O_2	Cr	<1
	Cr_2O_3	11.3
	PS	23.3

Table 5-1: Etching rates of Cr, Cr_2O_3, and PS for four different etching recipes. The pressure, RF power, ICP power, and temperature are fixed at 12 mTorr, 10 W, 1200 W, and 50 °C, respectively[53]. (reprinted with permission from American Vacuum Society).

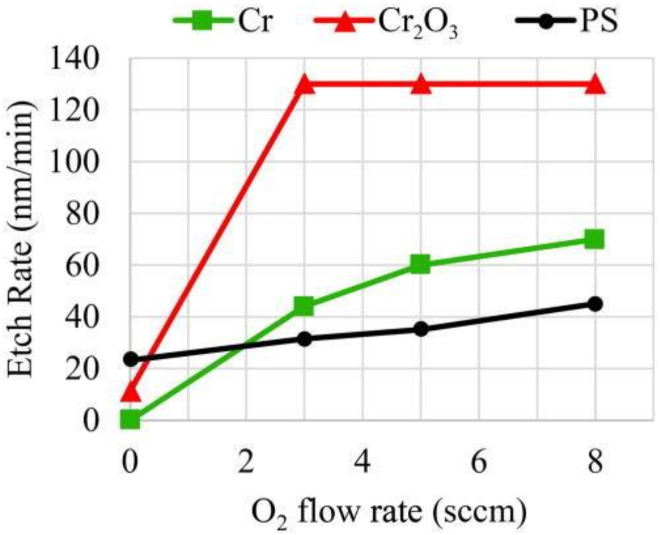

Fig. 5.8: Etching rates of Cr, Cr_2O_3, and PS as a function of O_2 flow rate. Note that the etching condition and the etching rate values here are the same as those listed in Table 5-1[53]. (reprinted with permission from American Vacuum Society).

When only Cl_2 gas was used, the etching rate of Cr was found to be <1 nm/min, and that of Cr_2O_3 was reduced to 11.3 nm/min. As the reduction in etching rate for PS is not as dramatic, the etching selectivity between Cr_2O_3 and PS is lower. Therefore, the addition of oxygen is essential, and a gas flow ratio of $Cl_2/O_2 = 47/3$ is considered optimal for our process.

It is equally important to have high etching selectivity between the hard mask material and the material to etch, here Si as an example. Therefore, etching rates of Cr_2O_3, Cr, and Si were examined using a non-switching pseudo-Bosch process. It is found that the etching rate for Cr_2O_3 was the same as that for Cr which was 4 nm/min, and the etching rate for Si was 390 nm/min that was nearly 100× faster than Cr or its oxide. Therefore, Cr_2O_3 is as efficient as Cr for masking Si etching. Fig. 5.9 shows high aspect ratio Si pillars fabricated by electron beam lithography and pattern transferring using Cr_2O_3 as the intermediate hard mask layer. As seen, pillars with a diameter down to 150 nm and height of 1.7 µm have been fabricated successfully.

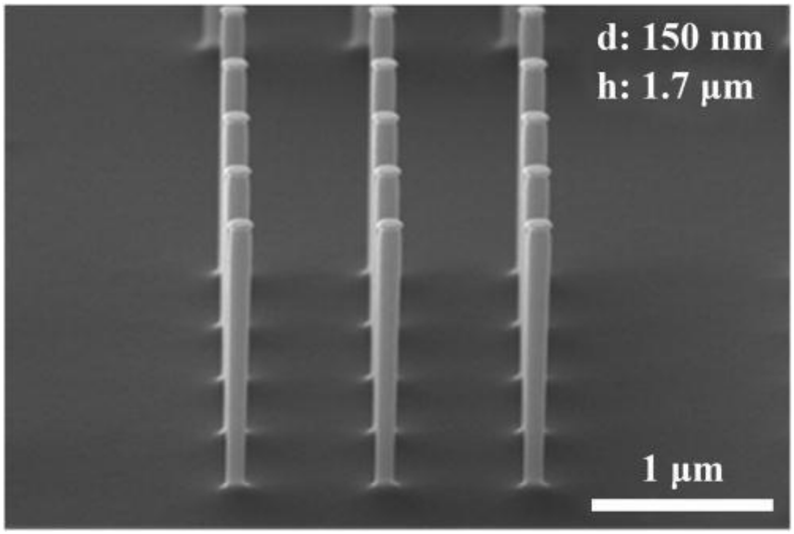

Fig. 5.9: SEM image of Si structures (Cr_2O_3mask still on) etched by non-switching pseudo-Bosch process[53] (reprinted with permission from American Vacuum Society).

As a result, we reported that Cr_2O_3 is a better choice than Cr as an intermediate hard etching mask material, where the resist pattern is first transferred into this material then into the substrate. This is because it contains oxygen by itself, and thus less oxygen is needed to be added to Cl_2 to form the volatile CrO_2Cl_2 etching product. With less oxygen in the Cl_2/O_2 gas mixture, the etching rate for resist, here polystyrene as an example of a negative resist, is reduced, and hence it is easier to transfer the resist pattern into Cr_2O_3 than into Cr. To achieve a high etching selectivity between Cr_2O_3 and polystyrene resist, 47/3 Cl_2/O_2 gas flow ratio has been found optimal with a selectivity of 4.1:1 (resist etches slower), as compared to the best selectivity of only 1.7:1 between Cr and polystyrene. For further pattern transferring into the substrate here silicon using non-switching SF_6/C_4F_8 gas, it was found that Cr_2O_3 has the same etching selectivity to silicon as Cr, both reaching a high value of 100:1.

Therefore, it is safe to say that the Cr_2O_3 mask is suitable for our HAR AFM tip fabrication process. In the following section, we will introduce a complete process flow for HAR AFM tip fabrication using one step e-beam lithography method.

5.2 Complete process to fabricate HAR AFM tip

Overall process flow, tip and cantilever profile, and the mask materials have been optimized in previous sections. Now, we will introduce the processing steps for batch fabrication of a complete HAR AFM tip. A schematic representation of the process flow is summarized in Fig. 5.10.

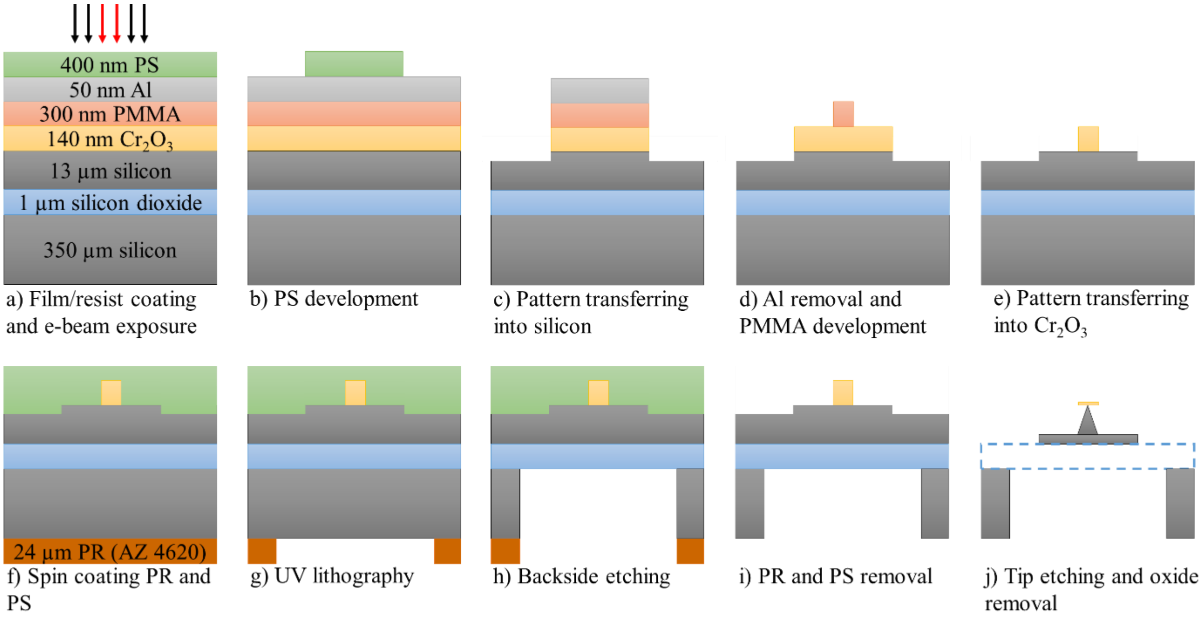

a) Film/resist coating and e-beam exposure
b) PS development
c) Pattern transferring into silicon
d) Al removal and PMMA development
e) Pattern transferring into Cr_2O_3
f) Spin coating PR and PS
g) UV lithography
h) Backside etching
i) PR and PS removal
j) Tip etching and oxide removal

Fig. 5.10: A schematic representation of fabrication steps with one step e-beam lithography for HAR AFM tip fabrication.

The fabrication starts with an SOI wafer with 13 µm device layer. First, a 140 nm Cr_2O_3 layer is deposited by an e-beam evaporator, and PMMA, Al, PS layers are coated under the same conditions with the process in section 5.1. The process steps until pattern transferring into Cr_2O_3 are kept the same (Fig 5.10a to 5.10e) except Cr_2O_3 etching is performed instead of Cr; however, the same recipe carried out to etch Cr_2O_3 has the same etching time as the (thinner) Cr due to the fast etching rate of the Cr_2O_3. Next, a layer of polystyrene (PS) is spin-coated on the front side to protect features from damage, contamination from handling and subsequent processes. Here, PS is preferred because it does not stick to the hot plate at our processing temperatures. After that, a cleaning step is followed by two layers of AZ 4620 positive photoresist was spin-coating at 2000 rpm for 40 sec (Fig. 5.10f). The sample is baked at 90 °C for 5 min after each spin-coating which resulted in 24 µm thick resist, and it is thick enough to mask entire 350 µm thick silicon under DRIE. The exposure is carried out by direct write UV lithography system under 1800 mJ/cm^2 exposure dose. The sample is then developed in AZ 400K for 8 min (Fig. 5.10g) followed by 45 min hard baking at 110 °C shortly before the etching. Afterward, 550 cycles Bosch process is performed under the following parameters (Fig 5.10h). Here, silicon dioxide is the etch stop layer as there is a good selectivity of >1:70 between silicon oxide and silicon.

Etching cycle: 7 sec, 160 sccm SF_6, 20 W RF, 800 W ICP, 25 mTorr, 15 °C.
Passivation cycle: 5 sec, 160 sccm C_4F_8, 5 W RF, 800 W ICP, 20 mTorr, 15 °C.

Previously 850 cycles Bosch process was performed to etch the same thickness because a silicon sample carrier wafer was utilized in etching which resulted in 400 nm/cycle etch rate. Recently, we started using a glass sample carrier wafer to benefit from low loading effect. The etch rate increased significantly from 400 nm/cycle to 650 nm/cycle allowing 500 cycles of Bosch process to etch 350 µm silicon. Here, a sample carrier wafer is used because the reactive ion etcher (Oxford Instruments Model: ICP380) is designed for operations with fixed sample size. Furthermore, we found out that only 10 µm AZ 4620 is consumed in case of using glass carrier wafer meaning that only one layer of resist is enough to etch entire wafer which makes the process even simpler. Next, remained photoresist and polystyrene are stripped. Finally, non-switching Bosch process is carried out for 75 min under 44 sccm C_4F_8 and 16 sccm SF_6, 20 W RF, 1200 W ICP, 10mTorr, 15 °C to form the AFM tip, followed by silicon oxide removal in HF solution (1:5 HF:H_2O for 37 min at room temperature).

An overview of the fabricated holder and cantilevers are shown in Fig. 5.11 where 2 cantilevers are designed as 30 µm × 115 µm and 30 µm × 225 µm.

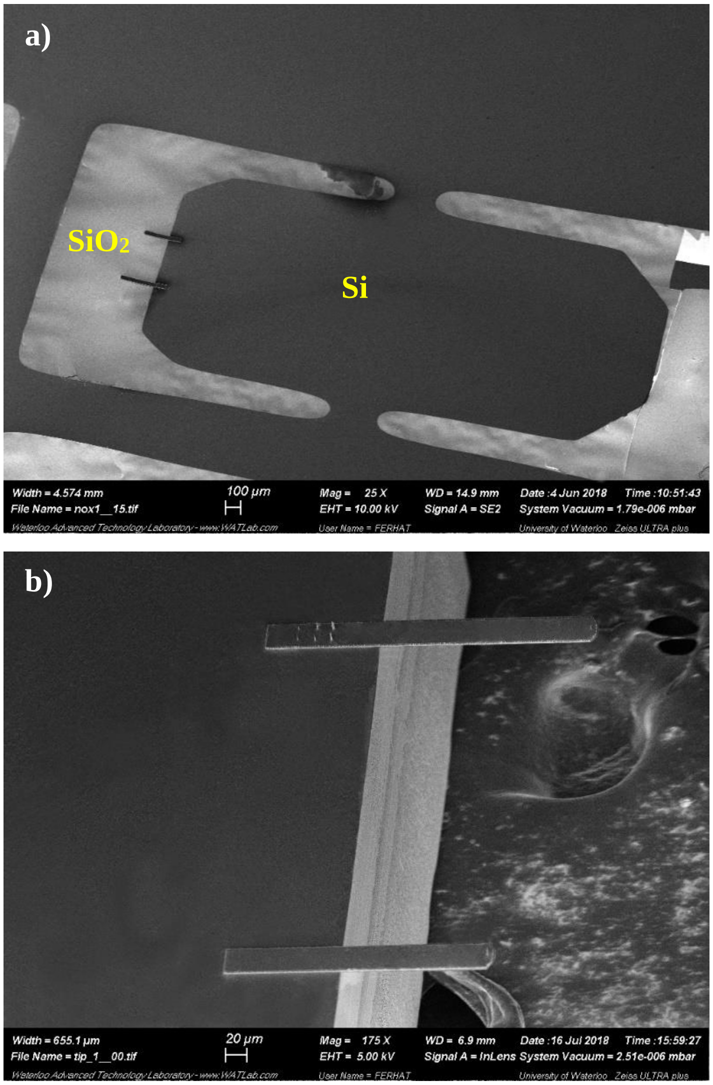

Fig. 5.11: SEM image of AFM probes, (a) overview of holder with two cantilevers with SiO_2 not etched away; (b) closer view of the cantilevers after SiO_2 etching.

In Fig. 5.12, close view of the long cantilever (30 µm × 225 µm), which is a close view of Fig. 5.11b, and HAR AFM tip are shown after oxide removal. There are some extra tips with different diameters patterned at the far end of the long cantilever to compare the results. Additionally, SEM images of a short cantilever (30 µm × 115 µm), which is a different cantilever than the one shown in Fig. 5.11, with a close view of tip are shown in Fig. 5.13.

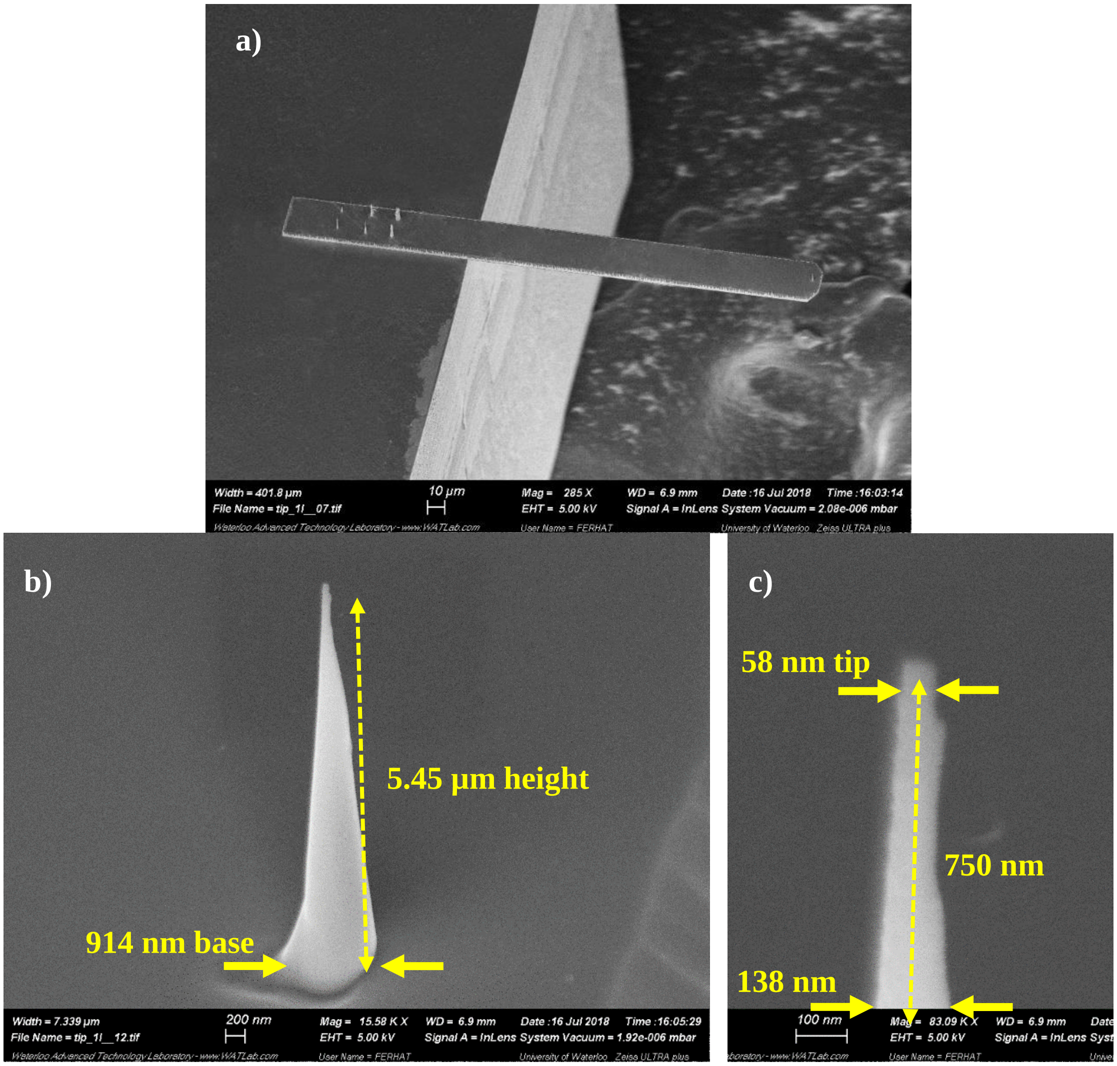

Fig. 5.12: SEM image of fabricated AFM tips; (a) 30 µm × 225 µm cantilever; (b) close view of the tip; (c) close view of tip apex etched under 44 sccm C_4F_8 and 16 sccm SF_6, 20 W RF, 1200 W ICP, 10 mTorr, 15 °C.

The original Cr_2O_3 mask designed for the tip has 600 nm diameter for long cantilever. Due to the non-switching Bosch recipe, the base diameter became larger to 914 nm, and the tip got broken because of the undercut etching, which happens because of lateral etching. Furthermore, the over-etching causes tip apex to be blunt; thus, the etching resulted in 5.45 µm height, 914 nm base diameter, and 58 nm tip apex diameter. Although the tip is not very sharp, it is in a suitable range for oxidation sharpening where tip diameters up to 200 nm are thin enough to be sharpened by oxidation. Additionally, the diameter of the tip is still 138 nm which is 750 nm below the tip apex meaning it can provide AFM scanning into very deep and dense structures.

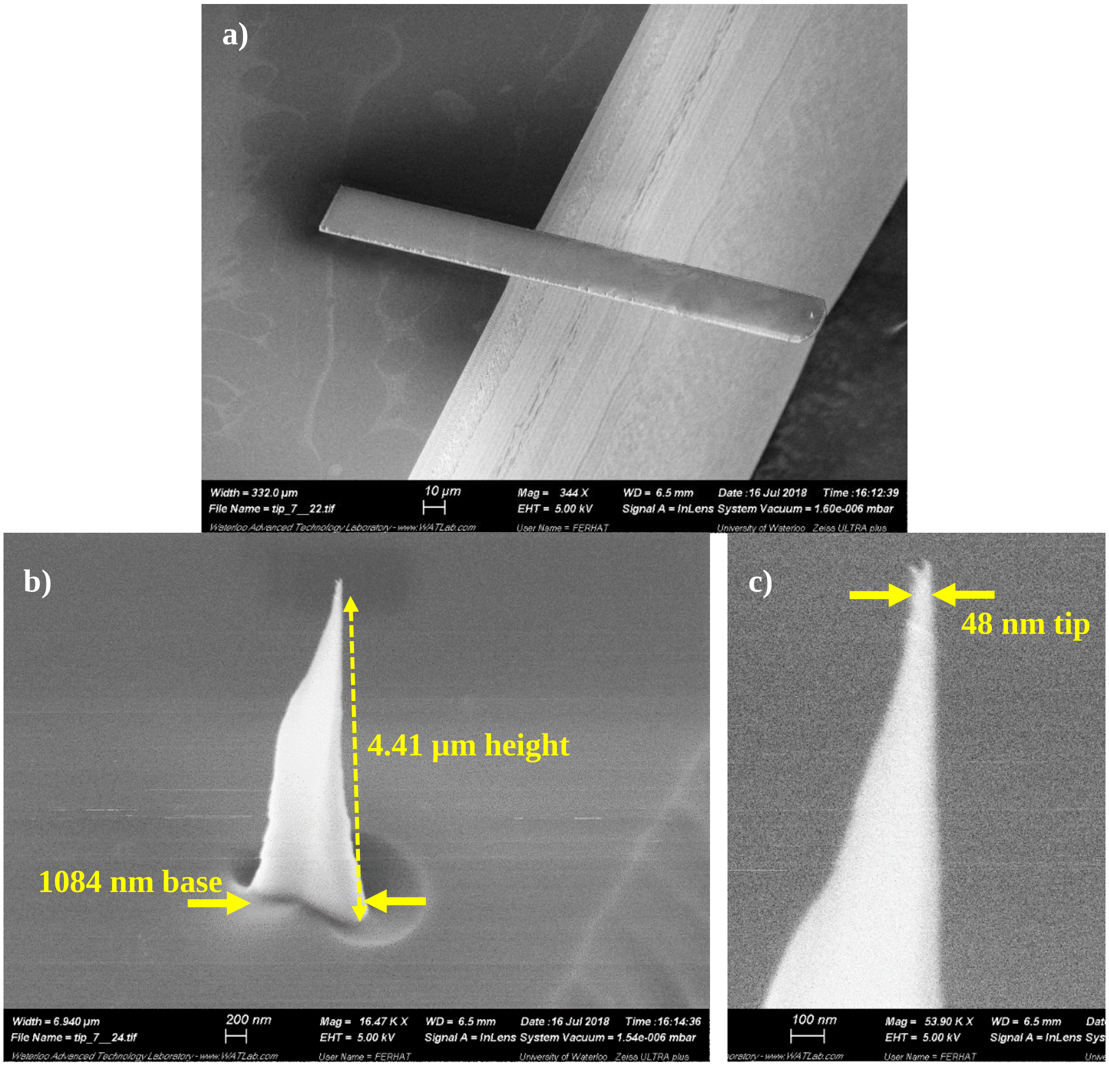

Fig. 5.13: SEM image of fabricated AFM tips; (a) 30 µm × 115 µm cantilever; (b) close view of the tip; (c) close view of tip apex etched under 44 sccm C_4F_8 and 16 sccm SF_6, 20 W RF, 1200 W ICP, 10 mTorr, 15 °C.

The original Cr_2O_3 mask designed for the tip has 800 nm diameter for short cantilever, and the etching resulted in tip with 1084 nm base diameter, 4.41 µm height, and 48 nm tip apex diameter. Similar to previous sample, the tip was broken at thinnest point during the etching where a fork like structure is formed at the tip apex (Fig. 5.13c). In general, over-etching causes blunting or formation of fork-like structures due to random metal mask falling down.

The tip has a thicker base diameter due to larger masking. Both tips shown in Fig. 5.12 and 5.13 do not have conical profile as obtained in the previous section on a silicon substrate. There are three possible reasons for irregular tip profile formation. 1) The tip is located at the end of the cantilever where the silicon gets thinner on silicon dioxide, and etching species change direction to etch left side of the tip faster. The effect is more obvious at the second pillar because it is originally thicker. Therefore, the tip is possibly getting affected by microloading effect. 2) The mask material might be deformed during processing the backside of the sample which results in deformed mask profile structures. 3) Passivation fluoro-polymer over time accumulates on the sidewalls randomly, causing non-uniform tip profile. In this case, the periodic plasma cleaning process may solve the problem. However, some of the tips at the far end of the cantilever have decent etching profile. One of them with a smaller diameter is shown in Fig. 5.14.

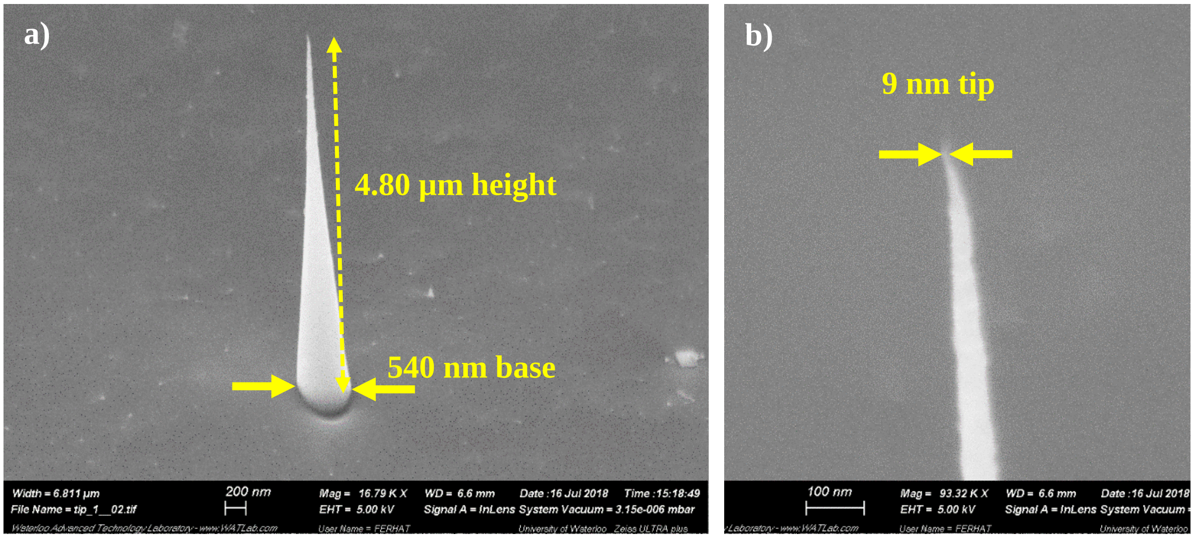

Fig. 5.14: SEM images of (a) the tip at the far end of the cantilever; (b) close view of tip apex etched under 44 sccm C_4F_8 and 16 sccm SF_6, 20 W RF, 1200 W ICP, 10mTorr, 15 °C.

The tip profile in Fig. 5.14 shows that the possible cause of the deformation observed on tip at the end of the cantilever is probably the microloading effect. Otherwise, the process has the potential to etch the tips as sharp as 9 nm as shown in Fig. 5.14b. The tip maintains a high aspect ratio for a couple of hundred nanometers which would be a perfect HAR AFM tip if it was on the other edge of the cantilever. The problem can be minimized by relocating the tip to further away from the edge. Additionally, both tips illustrated in Fig. 5.12 and 13 are still considered as high aspect ratio AFM tips due to the tip apex profile. On the other hand, we always measured the radius of the tip apex. In fact, the part of the tip that touches and feels the substrate during AFM scanning is a lot sharper than the apex radius. To find out the sharpness, a transmission electron microscopy (TEM) image needs to be taken. Instead, we prefer to test the performance of the tips under AFM. There are many more tips fabricated with similar tip profiles, though only a few of them was shown here.

5.3 Tip testing

The fabricated tips are tested in Dimension 3100 AFM to evaluate the performance of the tips. For comparison, we have scanned a sample with dense 400 nm diameter pillars with about 430 nm height by a commercial, regular AFM tip and our HAR AFM tips with long and short cantilever. The scanning results for the commercial, regular AFM tip is shown in Fig. 5.15.

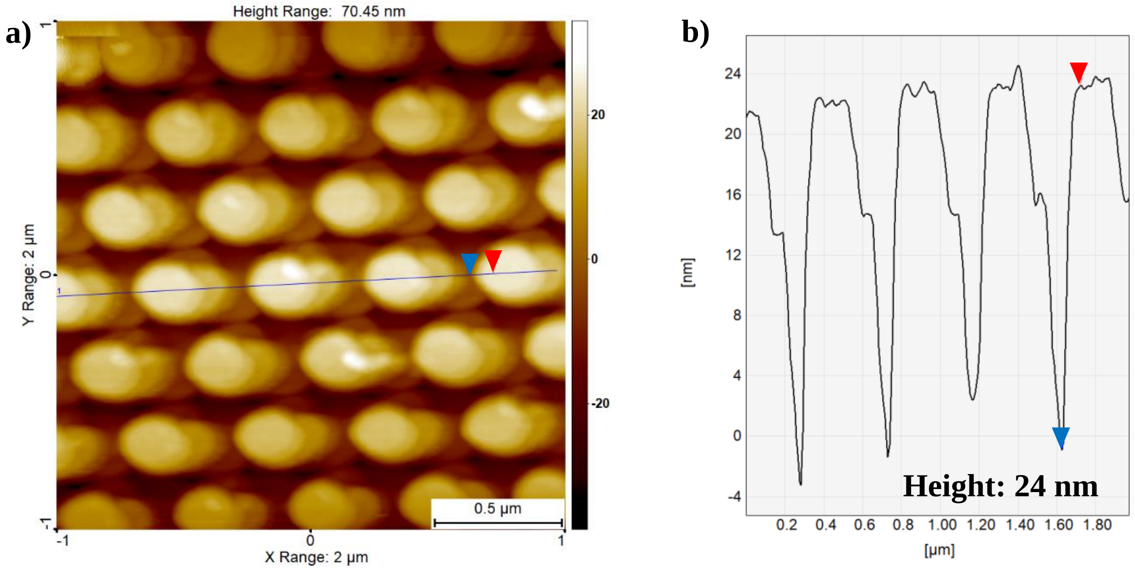

c)

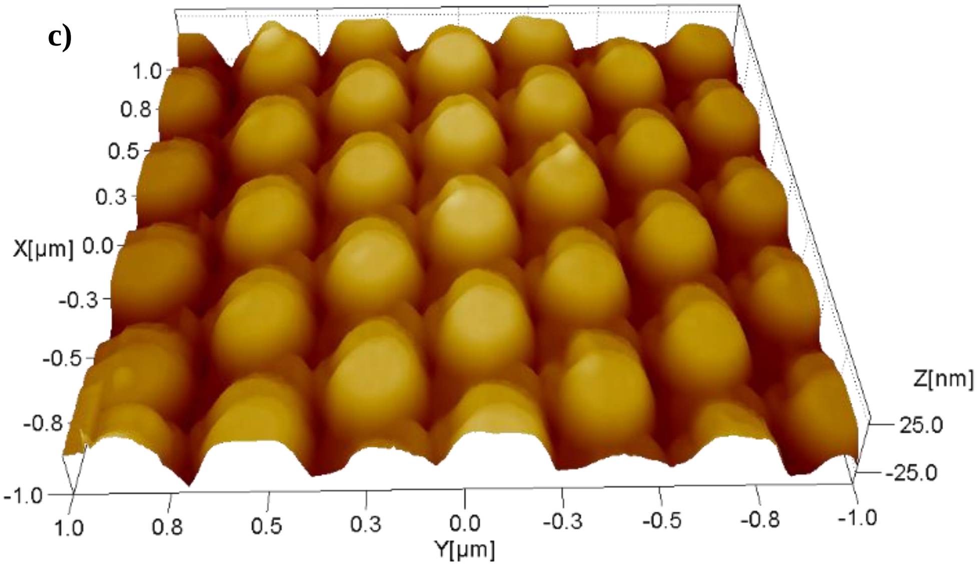

Fig. 5.15: (a) AFM image of pillar array scanned by a regular commercial AFM tip; (b) cross-section of pillars marked in (a); (c) 3D view of (a).

A 2 µm × 2 µm area was scanned with 0.5 Hz scan rate (2 µm/s tip velocity) and 256 samples/line parameters. Although the original height of the pillars are about 435 nm, the AFM scanning result shows 24 nm which is far from the real height. The reason for this huge difference is that the tip cannot reach to the bottom of the substrate in between closely patterned pillars. The regular tips are fabricated by KOH etching that forms a pyramid-shaped tip with large angle (54.74°). A schematic representation of a substrate scanning with a regular tip has been shown in Fig. 3.1. On the other hand, there are artificial profiles produced by AFM in the areas in between the pillars due to the same reason (Fig. 5.15c).

To image these type of samples, high aspect ratio AFM tips are required, so we tested our tips on the same sample under same scanning conditions. Furthermore, we measured resonance frequency of our cantilevers by AFM instrument. The scanning results are shown in Fig. 5.16 for the long cantilever, and in Fig. 5.17 for the short cantilever.

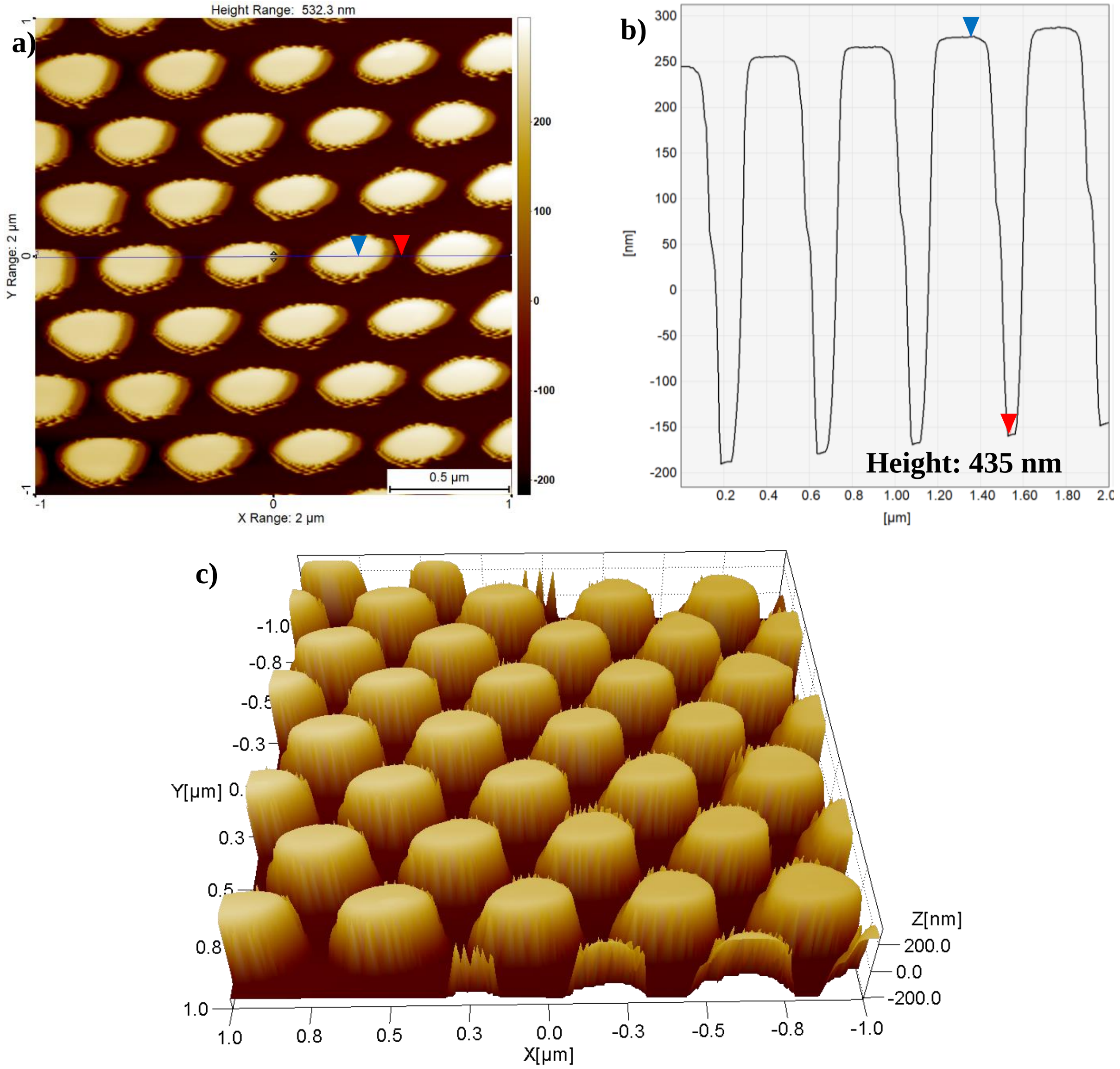

Fig. 5.16: (a) AFM image of pillar array scanned by our HAR AFM tip with long cantilever (displayed in Fig. 5.12); (b) cross-section of pillars marked in (a); (c) 3D view of (a).

The AFM scanning results for the long cantilever shows that there is a clear separation between pillars (Fig. 5.16a), and the tip can reach to the bottom; the height of the pillars is measured accurately according to the cross-sectional diagram (Fig. 5.16b). Also, the 3D view shows great improvement as expected (Fig. 5.16c).

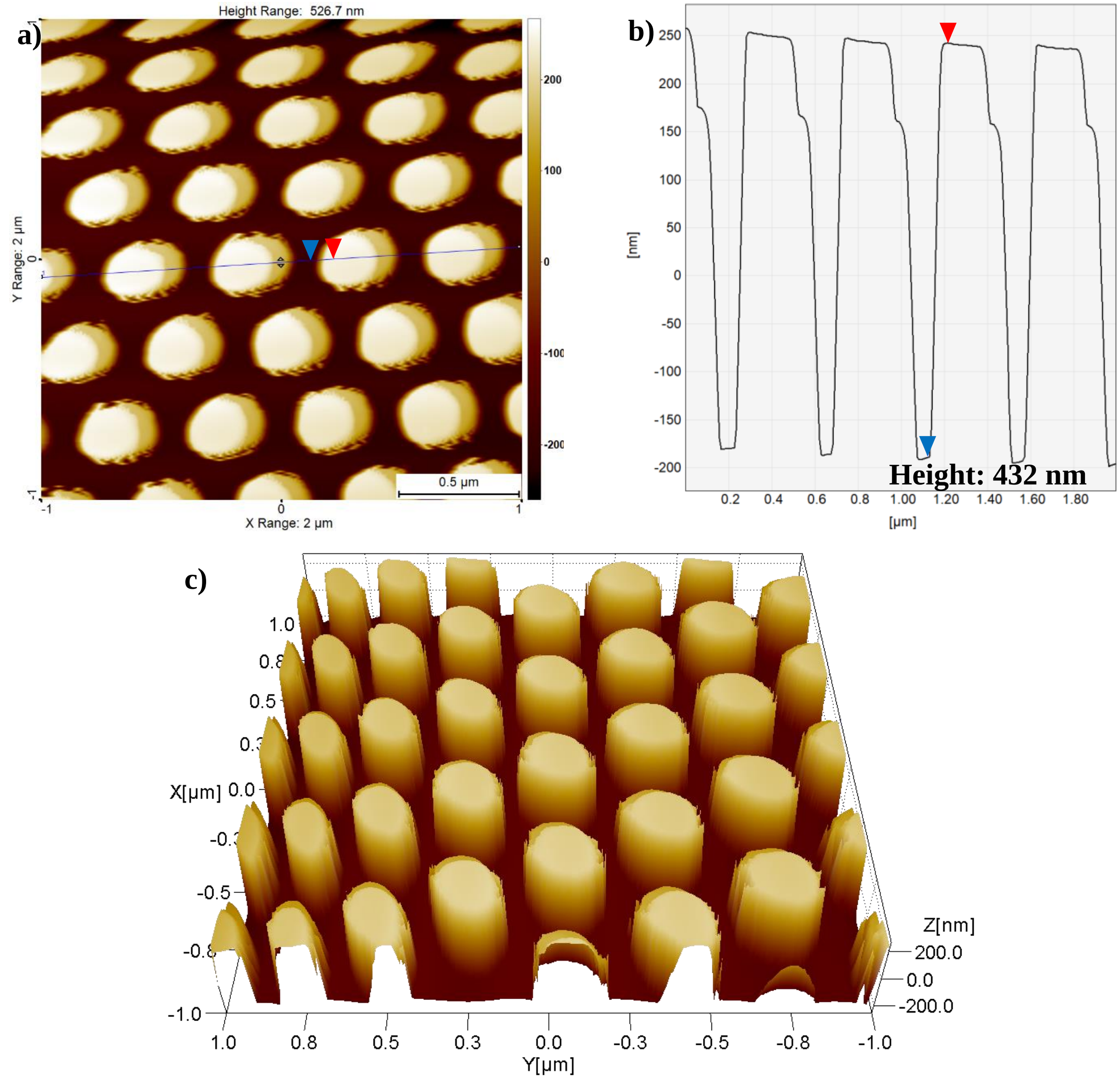

Fig. 5.17: (a) AFM image of pillar array scanned by our HAR AFM tip with short cantilever (displayed in Fig. 5.13); (b) cross-section of pillars marked in (a); (c) 3D view of (a).

The AFM scanning results for the short cantilever also demonstrates the success of the fabricated tips. There is a clear separation between pillars (Fig. 5.17a), and the tip can reach to the bottom similar to the previous tip; the height of the pillars is measured accurately as 432 nm according to the cross-section diagram (Fig. 5.17b). Also, the 3D view shows that there is a great improvement in results as expected (Fig. 5.17c).

Overall, we obtained excellent AFM scanning from both tips; the height is accurate, the surface of the sample and top of the pillars are very smooth. The resonance frequency of the tips also measured under AFM (Fig. 5.18); the long cantilever resonates at 100 kHz (Fig. 5.18a); the short one resonates at 165 kHz (Fig. 5.18b).

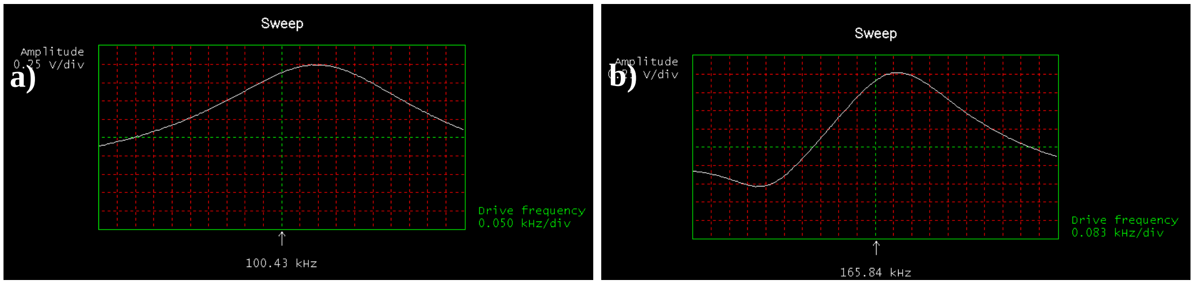

Fig. 5.18: Drive frequency curves of (a) long cantilever; (b) short cantilever.

The resonance frequency of the cantilever can be calculated by the following equation.

$$f_0 = \frac{1}{2\pi}\sqrt{\frac{k}{m_0}} \qquad and \qquad k = \frac{Ewt^3}{4l^3} \qquad \therefore \qquad f_0 \propto \sqrt{\frac{E}{\rho}}\frac{t}{l^2}$$

where f_0 is resonance frequency; k is spring constant (also called force constant); m_0 is effective mass; E is Young's modulus; w, t, l are width, thickness, length, respectively; ρ is density. As it can be seen, the resonance frequency is inversely proportional to square of the length and proportional to thickness. Increase in length decreases the frequency very fast; therefore, the resonance frequency of the tip is mostly determined by the length. The resonance frequency is important because it determines how fast AFM scanning can be performed while AFM imaging is slower than other imaging methods like SEM. On the other hand, spring constant determines the stiffness of the cantilever which is an important parameter for scanning mode. In general, a thick and short AFM cantilever has a high spring constant and resonance frequency which properties are suitable for non-contact mode AFM operations because otherwise it is stiff and can damage the sample; a thin and long cantilever has a low spring constant and resonance frequency and is suitable for contact mode AFM operations since it is soft and does less damage during the scanning. Our long cantilever can be considered as intermediately stiff, and short cantilever stiff which have calculated spring constants of 7 N/m and 36 N/m, respectively. Furthermore, we did not target a specific application while fabricating the AFM tips, and the resonance frequencies can be tuned by changing dimensions of the cantilever. We obtained smaller resonance frequency for the long cantilever, and larger for short as expected. The resonance frequency range in standard operations is 50 kHz to 500 kHz while there are slower and faster special AFM probes available commercially. A comparison between a commercial HAR AFM tip cantilever with our cantilever is listed in Table 5-2 where the resonance frequency and spring constants are higher in commercial one because of its larger width and thickness. Overall, there is a well agreement between our and commercial cantilevers.

	NanoWorld	**Our tip**
Resonance Frequency	130 kHz	100 kHz
Spring Constant	15 N/m	7 N/m
Length	225 µm	225 µm
Width	33 µm	30 µm
Thickness	5 µm	4 µm

Table 5-2: Cantilever parameter comparison with a commercial AFM probe from NanoWorld[75].

Lastly, we faced some issues regarding the tip holder part formed by DRIE. In the following sections, we will address the issues and introduce some solutions.

5.3.1 Two steps holder profile

To avoid the cantilever and tip holder from touching the sample, AFM scanning is carried out under a small cantilever tilt angle of 10° - 15° (i.e., cantilever not parallel to the horizontal surface). Because we etched holder part by DRIE, the etching profile is quite vertical, causing a part of the cantilever to be “shadowed” from the laser light; therefore, they look shorter than reality. Fig. 5.19 illustrates how our AFM probes look under AFM camera.

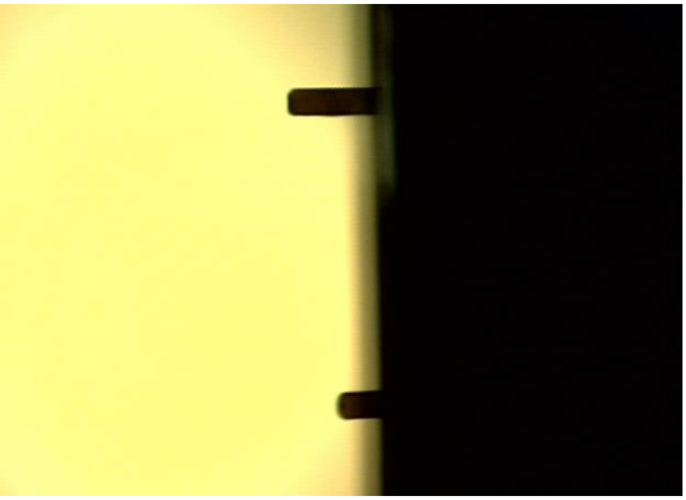

Fig. 5.19: Image of cantilevers’ backside from AFM camera where the probes are tilted.

In case of high resonance frequency AFM probes, the cantilever should be even shorter that may cause a problem for laser to shine onto the backside of the cantilever. To avoid this issue, the holder part is generally etched in KOH solution where etching results in 54.74° taper angle. Alternatively, we developed two steps structure to reduce this problem (Fig. 5.20).

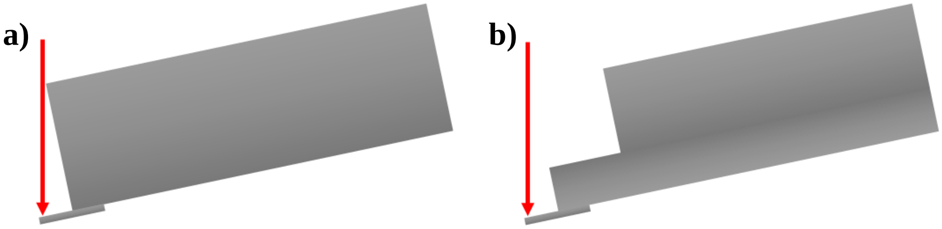

Fig. 5.20: Schematic representation of tilted AFM probes with (a) 1 step; (b) 2 steps holder profile.

The SOI wafer came with a 1 µm oxide on the back side of the wafers, and we patterned this oxide layer to form 2 steps structure. The fabrication process is presented in Fig. 5.21.

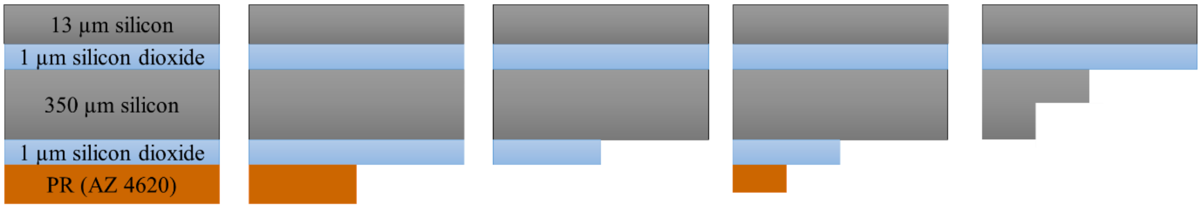

a) Spin coating PR
b) UV lithography
c) Oxide etching
d) UV lithography
e) DRIE + PR and oxide removal

Fig. 5.21: Schematic representation of fabrication processes for 2 steps holder profile.

The process consists of two UV lithography steps; first lithography is carried out to pattern oxide layer; a second lithography step is performed to define second holder step. After DRIE step, 2 steps structure will be defined. 1 µm oxide layer is enough to mask 100 µm to 150 µm silicon, and the thickness of the steps can be tuned by thinning the oxide layer. As can be seen from the cross-sectional representation of the structure in Fig. 5.20b, the steps will allow laser to focus on even shorter cantilevers. Images of the AFM holder array after second lithography step and SEM image of the holder after etching are shown in Fig. 5.22.

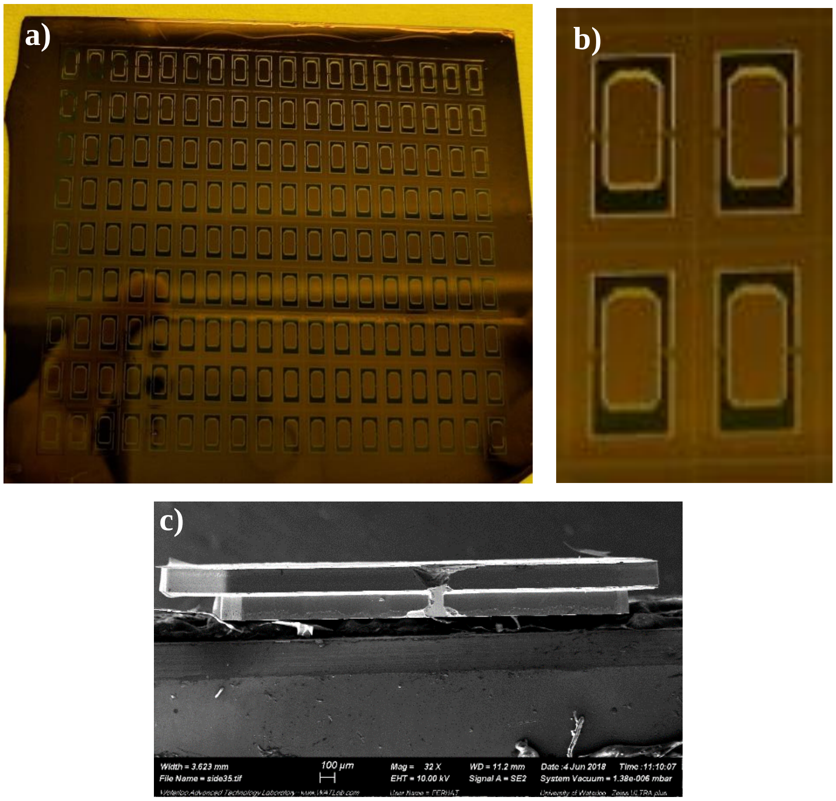

Fig. 5.22: Image of large array of AFM holders after second lithography step. (a) displays 182 holders, (b) close view of (a); (c) SEM image of 2 steps structure after DRIE.

Unfortunately, we have not fabricated tips with 2 steps structures because our tips are already serving our purpose. Therefore, we only focused process developing for the future works.

Also, we studied KOH etching to embed it to our process as it does not require 2 steps UV lithography, and it is cost efficient compared to DRIE.

5.3.2 KOH etching for holder part

There are two concerns to make our process compatible with KOH etching. First, it requires a layer of mask that is resistant to KOH which requires an additional coating step. Second, the front side of the device needs to be protected against KOH etching. In general, an oxidation step is performed to protect the front side and mask the backside as discussed in Chapter 2. However, in our case, we performed 1 step lithography to define both cantilever and tip patterns where a layer of Cr_2O_3 is present before backside processing. Although the melting point of the Cr2O3 is quite high, there will be oxidation underneath of the mask that will peel the mask off in subsequent oxide removal step. Therefore, we preferred to use a product called ProTEK B3-25 (from Brewer Science Inc.) alkaline protective coatings. Additionally, there is ProTEK PSB photosensitive alkaline-protective material commercially available. As they only involve spin-coating step, the process will be compatible and straightforward to our method. We have prepared some samples under different conditions, which are listed below, to evaluate the protection performance of the product. Thus, the samples are immersed into 40% KOH at 70 °C for 5 h.

Sample 1:
Spin-coat HMDS: 1500 rpm (10000rpm/s acceleration) for 30 sec
Spin-coat ProTEK B3-25: 1500 rpm (5000 rpm/s acceleration) for 40 sec
Bake at 110 °C for 1 min + 205 °C for 15 min

Sample 2:
3x spin-coat ProTEK Primer: 1500 rpm (10000 rpm/s acceleration) for 30sec
Bake at 205 °C for 2min (cooldown between each spin-coating)
Spin-coat ProTEK B3-25: 1500 rpm (5000 rpm/s acceleration) for 40 sec
Bake at 110 °C for 1min + 205 °C for 15 min

Sample 3:
Spin-coat ProTEK B3-25: 1500 rpm (5000 rpm/s acceleration) for 40 sec
Bake at 110 °C for 1 min + 205 °C for 15 min

Sample 4:
30 nm Cr deposition

Spin-coating ProTEK B3-25: 4000 rpm (10000 rpm/s acceleration) for 40 sec
Bake at 110 °C for 1 min + 205 °C for 2 min

Sample 5:

Spin-coat HMDS: 1500 rpm (10000 rpm/s acc.) for 30 sec
Spin-coat ProTEK B3-25: 4000 rpm (10000 rpm/s acc) for 40 sec
Bake at 110 °C for 1 min + 205 °C for 5 min

The images of the samples before and after KOH immersion are shown in Fig. 5.23.

Fig. 5.23: Images of samples prepared under different conditions; (a) before; (b) after KOH immersion.

As it can be seen from images in Fig. 5.23b, spin-coating at 1500 rpm causes peeling off of the protective coating at the edges significantly. When it is spin-coated at 4000 rpm, no peeling off is observed. The film thickness is 7 µm at 1500 rpm and 4.2 µm at 4000 rpm spin-coating where the film thickness will be even higher at the edges due to the edge bead effect. Therefore, either the edges should be thinned by acetone, or the film can be spin-coated at higher speeds. In the later case, it should be made sure that the film is thick enough to protect the features on the front side. Overall the performance is great, so we will benefit from this product in our future works.

5.3.3 Oxidation sharpening

Oxidation sharpening is an essential concept in AFM tip fabrication as standard methods are not sufficient to form tips at range that oxidation sharpening does. In this concept, pre-fabricated silicon-based AFM tips are thermally oxidized until the tip apex diameter reaches the target range, and then the oxide is etched away in HF solution. The process works because the oxidation rate decreases with stress which is higher at tip apex. Thus, oxidation close to the top is slower than the base of the tip. Tip apex radius below 1 nm is reported in literature in 1991[76], and it is a well-developed concept. SEM and TEM images of the oxidized tip are shown in Fig. 5.24 where original tip diameters are from 25 nm to 150 nm.

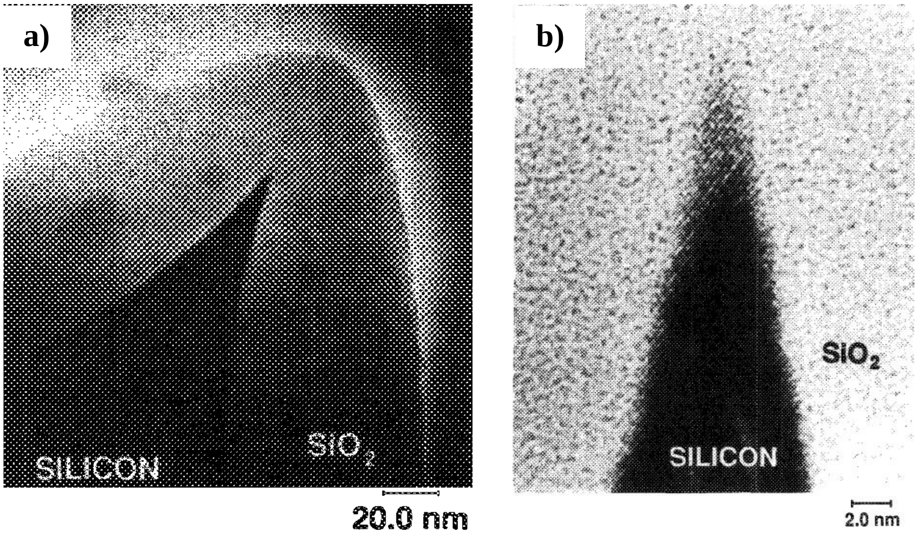

Fig. 5.24: (a) SEM ; (b) TEM images of the oxidized AFM tips (Adopted by permission from Ref.[76]).

Although ultra-sharp tips can be formed by oxidation sharpening, in standard tips the aspect ratio of the tip is limited which is due to the original profile of the tip. On the other hand, oxidation sharpening would result in decent results on our HAR AFM tips due to their conical profile with small taper angle. Therefore, as a future work, we will add oxidation sharpening step to our process.

Chapter 6

AFM cantilever patterning using grafted polystyrene monolayer brush

Our one-step e-beam lithography method can handle fabrication of any arbitrary pattern on a cantilever that can find applications on cantilever-based sensors. On the other hand, the methods mentioned in Chapter 2 (such as FIB) are commonly employed to pattern or re-shape a pre-fabricated AFM tip to make the tip apex high aspect ratio or create structures on the flat cantilever part for various applications. E-beam lithography is more cost-efficient than FIB, and here we will present e-beam lithography on a cantilever using mono-layer brush resist.

The main part of this chapter is reprinted with permission from Ref. [77]*. Copyright (2018) American Chemical Society.*

> Aydinoglu, F., Yamada, H., Dey, R.K., and Cui, B., 2017. Grafted Polystyrene Monolayer Brush as Both Negative and Positive Tone Electron Beam Resist. *Langmuir*, *33*(20), pp.4981-4985.

Although spin-coating is the most widely used electron-beam resist coating technique in nanolithography, it cannot typically be applied for nonflat or irregular surfaces. Here, we demonstrate that monolayer polystyrene brush can be grafted on substrates and used as both positive and negative electron-beam resist, which can be applied for such unconventional surfaces. Polystyrene is a popular negative resist when using solvent developer, but solvent cannot be used for grafted polystyrene brush that is firmly bonded to the substrate. Instead, we employed two unconventional development methods to lead polystyrene brush to positive or negative tone behavior. Negative tone was achieved by thermal development at 300 °C because exposed thus cross-linked polystyrene brush is more thermally stable against vaporization than unexposed linear one. Surprisingly, positive tone behavior occurred when the brush was grafted onto an aluminum (Al) layer and the film stack was developed using diluted hydrofluoric acid (HF) that etched the underlying Al layer. By transferring the patterns into the silicon (Si) substrates using the thin Al layer as a sacrificial hard mask for dry etch, well-defined structures in Si were obtained in two different electron-beam resist tones as well as in nonflat surfaces.

To fabricate nanostructures, lithography methods are used for both industry and research purposes, such as electron beam lithography (EBL) and photolithography. These lithography methods use resists on which patterns are drawn or duplicated from the mask or mold. The most widely used method for resist coating is spin-coating because of its simplicity, cost efficiency, and high resist thickness uniformity. However, spin-coating does not coat a uniform resist layer on nonflat substrates that is required for some applications such as patterning on atomic-force microscope (AFM) tips for tip-enhanced Raman spectroscopy[78] or lab-on-fiber technology[79]. Therefore, fabrication methods that are applicable in these nonflat surfaces are desired.

Several methods have already been demonstrated to pattern nanostructures on irregular or nonplanar surfaces. For example, as EBL resists coating techniques on such surfaces, ice lithography[80,81], evaporative resists[59,82], spray coating[83], spin-coating using low viscosity resists[84,85], float coating[86], and dip coating[87] have been developed. For ice lithography, an amorphous ice layer is formed on the cooled substrate inside a vacuum e-beam (or ion beam) chamber, and then patterning is performed by focused electron beam or focused ion beam. The drawback of this method is that it requires specially modified scanning electron microscope (SEM) system. Also, the sensitivity of ice resist is extremely low compared to the typical electron beam resist such as PMMA. Evaporated polystyrene resist can also be used as an electron beam resist on irregular surfaces[59,82]. Uniformity of the film coated by this method is much better than that of the spin-coated film because evaporated resists do not suffer from the edge bead effect, which deteriorates the uniformity of the spin-coated film. However, resists choices that can be thermally evaporated are limited. For example, the popular positive tone electron beam resist, PMMA, cannot be used for this method because its thermal decomposition mainly relies on depolymerization or end-chain scission. Also, thermal evaporation system is costlier than the spin-coating system. Another method that can be used for nonflat surfaces is spray coating[83]. It can be applied even on sharp edges of trenches. However, it requires optimization of resist solution to achieve proper mobility of resist, and the resist thickness varies significantly between flat surfaces and slanted surfaces. Next, spin-coating using low viscosity resists can be applied for nonflat surfaces[84,85]. Resists can be coated even on nearly vertical surfaces by using this method. However, to obtain uniform thickness, side faces of the substrate should be parallel to the radial direction of the spinning. Float coating is another method that can be applied on nonflat surfaces[86]. In this method, resist is dried on the surface of wafer in which substrate is submerged. Then, water is extracted, and the resist covers the substrate. The patterning on AFM tips has been demonstrated by using this method. Lastly, dip coating can cover irregular surfaces with resist[87], but it suffers from the difficulty to make uniform film.

There are several other methods to make nanopatterns on irregular, nonflat substrates. Nanoimprint lithography can be used for nonflat or irregular surfaces with or without using spin-coating[88,89,90]. Spin-coating of imprint resist can only be applicable for slightly curved but smooth surface. Resist coating on nonflat surfaces can also be achieved by transferring the prefabricated nanopatterns on rigid substrates to unconventional substrates by using an intermediate polymer layer[91,92]. The transfer of metal nanostructures to fiber facet and silica microsphere has been demonstrated by using this method. Transferred hard mask lithography can also be applied for unconventional substrates[93]. Si membrane hard masks are made by conventional nanofabrication methods like electron beam lithography or photolithography and then transferred onto substrate. Because the substrate should be smooth enough to be covered with membranes, it cannot be applied for sharp structures.

Using self-assembled monolayer (SAM) resists[94,95],[96] is another well-known method that would be capable of patterning irregular substrates. The most popular SAM resist is based on trichloro-silane that bonds readily to −OH terminated substrate[97]. However, SAM resists are too thin (typically 1–2 nm[98]) for acting as dry etching mask; and they have very low sensitivity, typically one order lower than that of PMMA[99]. Additionally, long-term stability of SAMs is limited for a range of reagents/media[100,101].

Although many methods have been developed for nanofabrication on unconventional substrates, each method has the limitation on its applicability, and there is no universal method. Therefore, a new method to fabricate nanostructures on irregular, nonflat surfaces is still desired to be developed. Previously, we have shown that PMMA polymer brush grafted on substrates can be used as resists for EBL, and it can be applied for nanofabrication on irregular or nonplanar surfaces[102,103]. In this paper, we will show nanopatterning on AFM cantilever using monolayer polystyrene (PS) brush. Although thick PS film is known as a negative electron beam resist when solvents are used as developer[104,105,106], we have found that PS monolayer brush layer can be used as both negative and positive resist depending on the development condition. Negative tone behavior was achieved using thermal development that preferably desorbs the unexposed linear PS; whereas positive tone behavior was unexpectedly attained when PS was coated on Al and the film stack was "developed" using diluted HF that etches Al, indicating electron beam exposure weakened PS capability of protecting the underlying Al against HF etch.

Fig. 6.1 shows the schematic representation of the fabrication process to utilize PS brush as electron beam resist. First, a silicon substrate was cleaned by RCA cleaning, and a thin layer of Al (~8 nm) was deposited on substrate as a sacrificial hard mask layer because the brush layer is too thin for pattern transferring. The surface was then treated by oxygen plasma for 1 min. Afterward, carboxyl-terminated polystyrene PS-COOH (Scientific Polymer Products, Ontario, New York State, molecular weight (Mn) 13 000 g/mol) was dissolved in toluene with a concentration of 10 w/v%. After spin/drop coating (spin for flat substrate (at 4000 rpm for 40 s), drop for AFM cantilever), the thick resist film was baked at 160 °C for 24 h to promote the adsorption of PS-COOH onto the substrate, presumably via the reaction of the −COOH end group and the hydroxyl group on the substrate with the release of H_2O. Then, the substrate was soaked in toluene for 1 min to remove the bulk of PS film that could be very nonuniform if the substrate was nonplanar. Therefore, only a grafted monolayer of PS-COOH with remarkably uniform thickness remained on the substrate. Here the coating condition is not critical for our process, because anyway the thick/ungrafted part of the PS will be washed away by a solvent after the thermal annealing.

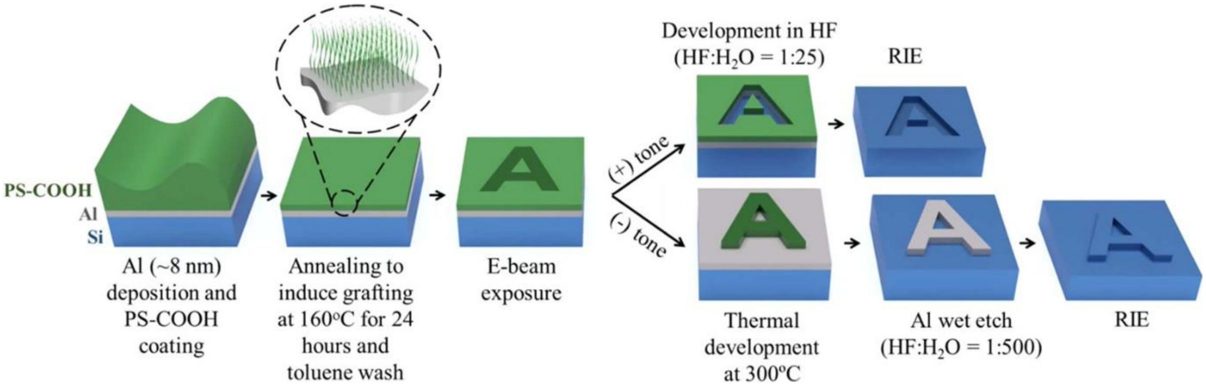

Fig. 6.1: Process steps for patterning substrates using PS brush as a monolayer resist for both negative and positive tone[77] (reprinted with permission from American Chemical Society).

Next, electron beam exposure was performed using LEO 1530 field emission SEM (Carl Zeiss) integrated with the nanometer pattern generation system (NPGS, JC Nabity Lithography Systems). The brush layer was developed with different conditions to obtain recessed or protruded structures. To achieve protruded structures, the PS brush layer was used as a negative resist. First, the resist was thermally developed on a hot plate at 300 °C for 60 s to preferably vaporize the unexposed PS, and then the aluminum layer was etched by diluted hydrofluoric acid (HF/H_2O, 1:500 volume ratio) for 70 s. Finally, the pattern was transferred to the silicon substrate by dry etching in CF_4 and O_2 plasma (20 sccm CF_4 gas, 3 sccm O_2 gas, 10 mTorr pressure, 50 W RF power) using the aluminum layer as a hard mask. On the other hand, to obtain recessed structures, the PS brush layer was used as a positive resist. In this case, without thermal development, the exposed area of the PS brush layer was lifted off by soaking for 15 s in diluted HF solution (HF/H_2O, 1:25 volume ratio) that etched away the underneath Al layer. This implies that the exposed PS became less effective in protecting the underneath Al against HF etching. Finally, the pattern was transferred in the same way as fabricating protruded structures.

To evaluate the thickness of the brush monolayer (see Fig. 6.2), PS-COOH was grafted on a silicon substrate after a brief oxygen plasma treatment to form hydroxyl group on the surface. Next, a layer of chromium (Cr) was evaporated simultaneously on the grafted silicon and bare silicon substrates which are partially shadow-masked. Afterward, unmasked brush layer was removed by O_2 RIE, and then the brush including Cr thickness measured by AFM was compared with Cr thickness on the bare silicon to obtain the brush layer thickness.

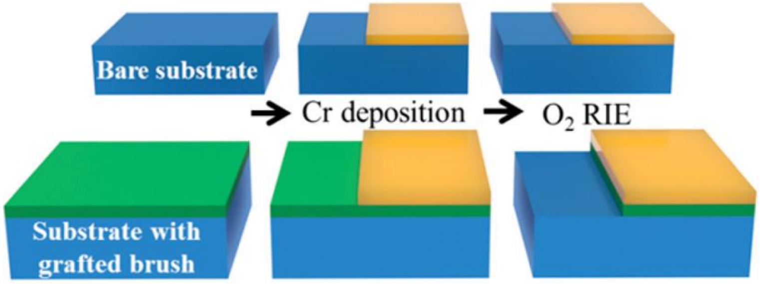

Fig. 6.2: Fabrication steps for brush thickness characterization[77] (reprinted with permission from American Chemical Society).

The monolayer brush thickness was measured as 15 nm from which the packing density/surface coverage for the PS monolayer can be calculated as 0.723 chains per square nanometer using the following equation $\sigma = (h\rho N_A)/Mn$, where h is monolayer thickness, ρ is bulk density of polystyrene (1.05 g/cm^3), and N_A is Avogadro's number. This surface coverage is in the high surface density regime. Formation of denser surface coverage is possible, too, using the "grafting from" approach where polymer brushes are generated in situ. In this work, the "grafting to" approach was preferred because it is an easier way to coat a surface, and it works well enough for our e-beam lithography application.

The molecular weight of the PS-COOH was chosen according to its commercial availability, and other MW would also work for our purpose. Generally, for higher resolution polystyrene with lower molecular weight would be preferred; for higher sensitivity (at the cost of resolution), higher molecular weight would be preferred. As for grafting temperature, it is chosen as 160 °C that is well above the glass transition temperature of PS and well below its decomposition temperature. Annealing time was selected as 24 h to ensure grafting with a high packing density, as it is reported that long annealing time will increase the number of grafted chains[107].

Moreover, as we pointed out in our previous study[103], carboxyl group might not bond chemically to −OH terminated substrate, and we were not able to show unambiguously the chemical bond formation. According to some studies[108,109], an intermediate layer that contains epoxy group should be coated before polymer brush formation to form strong chemical bonding. To test the adhesion of the PS monolayer, PS monolayer-coated samples were soaked in xylenes, toluene, and tetrahydrofuran solvents for an hour with ultrasonication. The monolayer could not be dissolved after this process, which shows that PS monolayer adhered firmly to the substrate, well enough to be used as a stable monolayer e-beam resist regardless whether it was chemically bonded to the sublayer or not.

When thick PS film is used as resist for EBL, it behaves as a negative resist because cross-linking is induced by electron beam exposure[104,105,106]. Likewise, the PS brush layer may work as a negative resist, yet solvent cannot be used as developer because the firmly grafted brush cannot be dissolved by a solvent. Because cross-linked PS has higher thermal stability against vaporization than linear one[110], thermal development can be used to carry out the development. However, if the development temperature is too high (≥350 °C), even cross-linked areas are decomposed and vaporized. On the other hand, if the development temperature is too low (≤250 °C), the unexposed areas are not fully vaporized. It was found that thermal development at 300 °C for 1 min was the optimal condition. Fig. 6.3 shows the SEM images of the pattern obtained by using the PS brush as a negative resist with thermal development. We have previously precisely demonstrated thermal development of thick polystyrene resist[111]. EBL was carried out with 5 keV at a line dose range of 2.2–3.8 nC/cm. Here low electron energy was selected to minimize proximity effect to achieve better resolution, and the optimum dose was determined experimentally where a range of line arrays with pitches from 50 nm to 1 µm and doses from 1 to 15 nC/cm were exposed. To perform pattern transferring, we etched the underneath Al by very diluted HF (1:500 dilution ratio); otherwise, if less diluted HF was used the remaining PS brush could not protect well the Al film underneath. After pattern transfer by RIE for 2 min, line array in silicon with 110 nm width was obtained at 2.2 nC/cm exposure dose. Fig. 6.3c shows AFM measurement of the line array that gave a 135 nm line height.

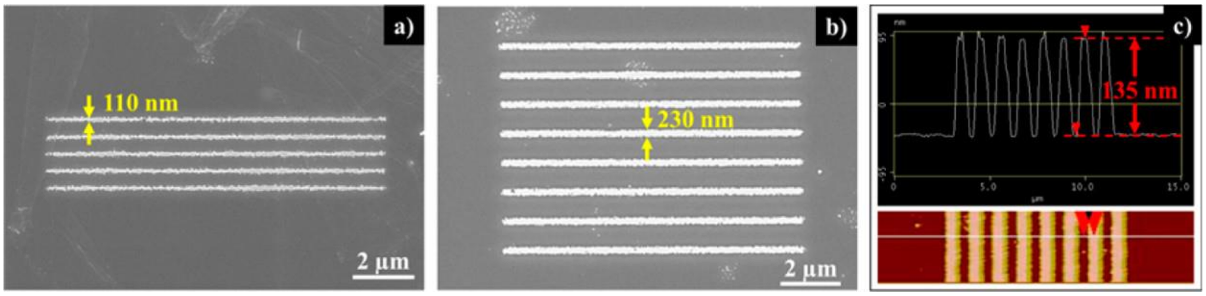

Fig. 6.3: SEM images of the line array pattern obtained by using PS brush as negative resist: (a) 500 nm period, 2.2 nC/cm exposure dose; (b) 1 µm period, 3.8 nC/cm; (c) AFM image of line array presented in (b). Here Al layer was kept for high-contrast SEM imaging, yet its thickness should be under 5 nm[77] (reprinted with permission from American Chemical Society).

Positive behavior of PS brush layer was also achieved by changing the development condition. The SEM images of patterns using PS brush as positive resist are shown in Fig. 6.4. EBL was carried out at 5 keV and a dose range of 0.2–3.8 nC/cm. These electron beam energy and dose values were also determined experimentally. To achieve positive behavior, the sample was developed by HF/H_2O (1:25 volume ratio) for 15 s without thermal development. HF washed away only the exposed area of PS layer together with the underneath aluminum layer, whereas the unexposed area remained. Next, to transfer the pattern into silicon, 2 min RIE has been carried out. AFM measurement of the trench depth resulted in 40 nm as shown in Fig. 6.4d. It should be noted that AFM probe could not reach to the bottom of the trenches, so the measurement is not accurate, yet the trench depth should be approximately the same as the line height mentioned above (135 nm) because the two samples were etched using the same RIE recipe.

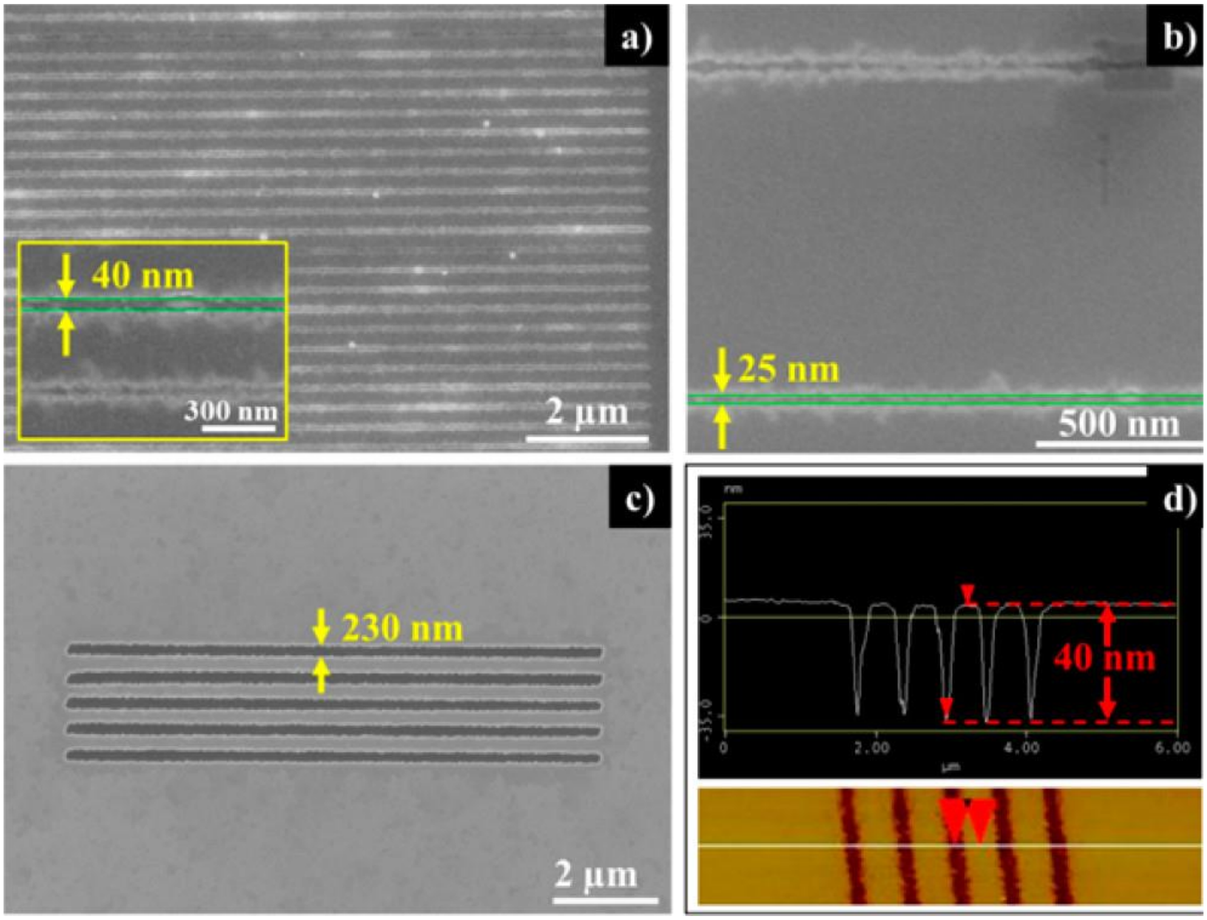

Fig. 6.4: SEM images of the pattern obtained by using PS brush as positive resist: (a) 300 nm period, 0.2 nC/cm, (b) 1 µm period, 0.2 nC/cm, (c) 500 nm period, 3.8 nC/cm, (d) AFM image of line array presented in (c)[77] (reprinted with permission from American Chemical Society).

Although (thick) PMMA can also be used as both positive and negative resist[112], our results indicate that the mechanism that changes the tone behavior of PS brush layer is very different from that for PMMA in which the increase of exposure dose changes the reaction induced by exposure from chain scission to cross-linking. In the case of PS brush, the tone behavior of resist was changed according to the development process even though the exposure dose was the same. Our results implies that, contrary to intuition that exposed thus cross-linked PS would behave as a better mask material, exposure actually made PS a weaker mask against HF etching of the underneath Al film.

Next, the process with positive tone behavior was applied on an AFM probe to demonstrate that PS brush applies to nanofabrication on irregular substrates. Periodic line arrays with 500 nm period were exposed at 5 keV and doses of 2 nC/cm and 6 nC/cm which resulted in 75 and 120 nm wide lines, respectively (Fig. 6.5).

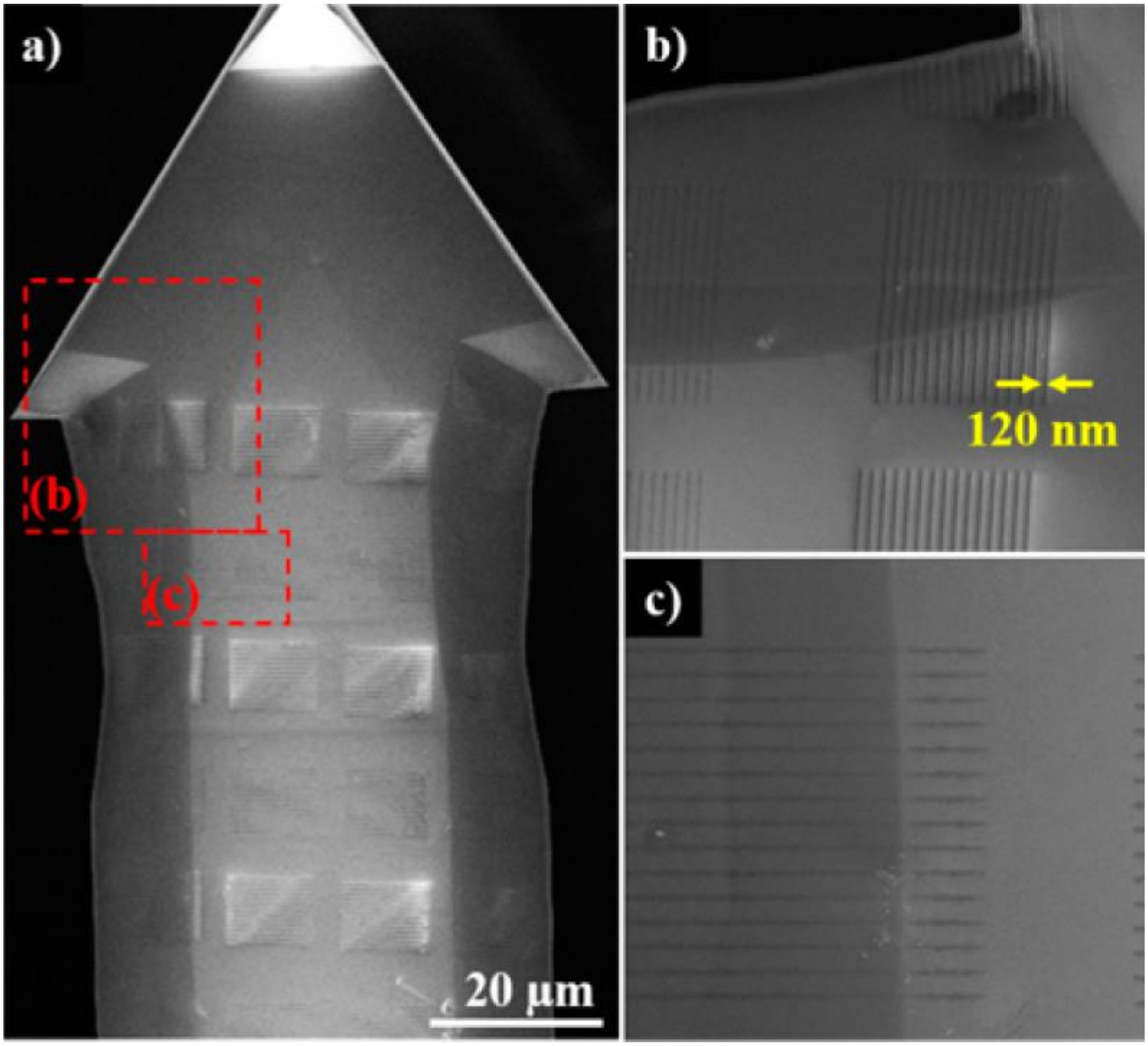

Fig. 6.5: SEM images of grating patterns on AFM probe: (a) top view; (b) close-up view, 500 nm period, 2.6 nC/cm dose; (c) 500 nm period, 1.2 nC/cm dose[77] (reprinted with permission from American Chemical Society).

Fig. 6.6 shows contact angles of bulk (thick) PS, non-cross-linked PS brush, and cross-linked PS brush, as 91°, 91°, and 65°, respectively. The results indicate that the cross-linked brush becomes more hydrophilic that would allow aqueous HF to penetrate through the brush to etch the underneath Al and thus lift-off the brush, so only the cross-linked area is removed, and the resist behaved as positive resist. Similar behavior has been obtained for SAM of octadecyltrichlorosilane on SiO_2 and Cr substrates after electron beam exposure[94,113]. Therefore, it is reasonable to believe that the working mechanism behind the pattern transferring for the positive tone behavior is hydrophilicity of the polymer brush.

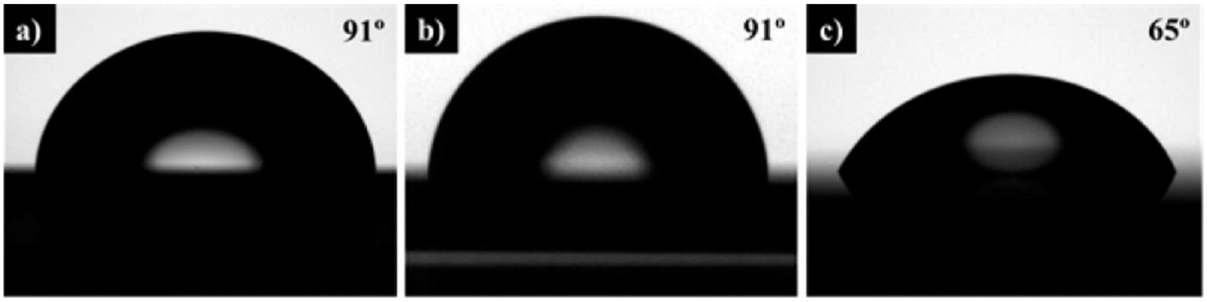

Fig. 6.6: Contact angle measurement of (a) thick PS film, (b) non-cross-linked PS brush, and (c) cross-linked PS brush[77] (reprinted with permission from American Chemical Society).

There might be some concerns regarding usage of HF depending on the application, but it should be noted that for negative tone, different etchants can be used to etch the sacrificial layer. For example, PAN etching (a mixture of phosphoric acid, acetic acid, nitric acid, and water) also worked well for pattern transferring into Al layer. Moreover, we have performed pattern transferring using Cr as the sacrificial layer that does not involve HF. Therefore, the process is not HF dependent. On the other hand, if one wants to avoid the usage of wet etching completely, clean dry etching process can also be carried out. The etching selectivity between Cr and PS is approximately 1:1, so 15 nm PS is enough to etch 15 nm Cr layer that is sufficient for etching 1 µm deep into Si.

The results shows high-resolution capability of 110 nm wide lines for the negative tone and 20 nm wide lines for positive tone. In the case of negative tone, resolution is limited by the random nature of PS brush vaporization (desorption) and proximity effect, and higher resolution could be obtained by reducing the proximity effect, such as by using high energy (e.g., 100 keV) exposure, exposure on thin membranes that are transparent to electrons, or designing very sparse patterns.

Lastly, because the brush layer is thin, there is a certain risk of pinhole formation that may cause unwanted etched holes into the substrate. However, the risk would be far less than the well-known SAM resists, which is commonly used as mask to etch gold layer for microcontact printing, because monolayer brushes are usually around ~10–15 nm thick whereas SAMs are usually only ~1–2 nm thick.

Chapter 7

Conclusions and future directions

To reduce the cost of HAR AFM tips, we have focused on developing a process for batch fabrication. In chapter 4, a process flow including UV lithography and one step hard masking is introduced. As a result, tip apex diameter down to 25 nm was fabricated and tested under AFM. The backside patterning is carried out by DRIE using thick positive photoresist, AZ 4620. There are some photoresist processing parameters needs to be paid extra attention while working on thick photoresists such as rehydration after soft baking, nitrogen outgassing during/after exposure, and reflow while hard baking. Each of the parameters was reviewed briefly.

Our processes involve standard Bosh and non-switching Bosch processes; therefore, each concept is discussed in detail. Structures with negative taper angle up to -10° was achieved which can be benefited as reentrant AFM probe for three-dimensional imaging. Afterward, a fabrication process to fabricate HAR AFM tips using only photoresist is introduces with some preliminary results. The process can be developed with proposed processing steps at the end of chapter 4.

A systematic process to fabricate high aspect ratio AFM tips by one step e-beam lithography is developed by benefiting from different sensitivities of polystyrene and PMMA. Alternatively, a thin layer of polymer that would not attack PMMA can be coated in between PMMA and PS to replace Al to reduce fabrication cost and time. Here, we have also proven that Cr_2O_3 is a better dry etching mask than Cr when pattern transferring from thin resists. By controlling etching parameters, HAR AFM tips down to 9 nm tip apex radius was demonstrated. Furthermore, AFM scanning results showed promising results regarding the performance of the fabricated tips. Although the tips are decent enough for our test sample, sharper tips are required for scanning denser and deeper structures. Therefore, the tip profile can be improved by oxidation sharpening.

When we etched long enough (in case of targeting 9 µm tip), the tip is getting broken at some point close to the top of the tip causing less control in tip profile. To overcome this issue, the etching parameters needs to be optimized. In our experiments, we carried out fabrication on SOI wafer with 13 µm device layer thickness where we kept cantilever thickness around 3.5 µm and targeted 9.5 µm tip height. Alternatively, device layer can be thinned before processing, and shorter tips can be fabricated to overcome tip breakage. This would work because the tips with slightly shorter than 5 µm are fabricated without facing any breakage or deformation problem as shown in Fig. 5.4 and 5.5. Also, the holder part, as a future work, can be etched by KOH instead of DRIE to reduce the overall fabrication cost and overcome the shadowing problem. We introduced a simple and compatible method to carry out KOH etching using an alkaline protective coatings.

We successfully showed that PS brush layer can be grafted on nonflat substrates and used as both positive and negative resist for e-beam lithography. Unlike PMMA which is known for changing its behavior from positive tone to negative tone depending on the exposure dose, the tone behavior of PS brush changes depending on the development conditions. Negative tone was achieved by thermal development, and positive tone was achieved by using diluted HF as a “developer.” After the pattern transferring to the substrate using the thin aluminum layer as an intermediate hard mask layer for dry etch, we obtained well-defined structures for both positive and negative cases on silicon substrates, as well as on an AFM cantilever. Therefore, the process can provide a simple way to fabricate both recessed and protruded structures on those nonflat surfaces which can be applied to tip-enhanced Raman spectroscopy[78] and lab-on-fiber technology[79].

References

[1] Binnig, G., Rohrer, H., Gerber, C. and Weibel, E., 1982. Surface studies by scanning tunneling microscopy. *Physical review letters*, *49*(1), p.57.

[2] Binnig, G., Quate, C.F. and Gerber, C., 1986. Atomic force microscope. *Physical review letters*, *56*(9), p.930.

[3] Eaton, P. and West, P., 2010. *Atomic force microscopy*. Oxford University Press.

[4] Cappella, B. and Dietler, G., 1999. Force-distance curves by atomic force microscopy. *Surface science reports*, *34*(1-3), pp.1-104.

[5] Jalili, N. and Laxminarayana, K., 2004. A review of atomic force microscopy imaging systems: application to molecular metrology and biological sciences. *Mechatronics*, *14*(8), pp.907-945.

[6] Stoffler, D., Goldie, K.N., Feja, B. and Aebi, U., 1999. Calcium-mediated structural changes of native nuclear pore complexes monitored by time-lapse atomic force microscopy1. *Journal of molecular biology*, *287*(4), pp.741-752.

[7] Zhong, Q., Inniss, D., Kjoller, K. and Elings, V.B., 1993. Fractured polymer/silica fiber surface studied by tapping mode atomic force microscopy. *Surface Science Letters*, *290*(1-2), pp.L688-L692.

[8] Sasa, S., Ikeda, T., Akahori, M., Kajiuchi, A. and Inoue, M., 1999. Novel nanofabrication process for InAs/AlGaSb heterostructures utilizing atomic force microscope oxidation. *Japanese journal of applied physics*, *38*(2S), p.1064.

[9] Sugimura, H., Uchida, T., Kitamura, N. and Masuhara, H., 1994. Scanning tunneling microscope tip-induced anodization of titanium: Characterization of the modified surface and application to the metal resist process for nanolithography. *Journal of Vacuum Science & Technology B: Microelectronics and Nanometer Structures Processing, Measurement, and Phenomena*, *12*(5), pp.2884-2888.

[10] Shirakashi, J.I., Matsumoto, K., Miura, N. and Konagai, M., 1997. Single-electron transistors (SETs) with Nb/Nb oxide system fabricated by atomic force microscope (AFM) nano-oxidation process. *Japanese journal of applied physics*, *36*(9A), p.L1257.

[11] "AFM TIP NanoWorld Webinar", P. Russell Appalachian State Univ., 10 November 2008.

[12] Han, J., Li, X., Bao, H., Zuo, G., Wang, Y., Feng, F., Yu, Z. and Ge, X., 2005. AFM probes fabricated with masked–maskless combined anisotropic etching and p+ surface doping. *Journal of Micromechanics and Microengineering*, *16*(2), p.198.

[13] Burt, D.P., Dobson, P.S., Donaldson, L. and Weaver, J.M.R., 2008. A simple method for high yield fabrication of sharp silicon tips. *Microelectronic Engineering*, *85*(3), pp.625-630.

[14] Li, J.D., Xie, J., Xue, W. and Wu, D.M., 2013. Fabrication of cantilever with self-sharpening nano-silicon-tip for AFM applications. *Microsystem technologies*, *19*(2), pp.285-290.

[15] Brugger, J., Buser, R.A. and De Rooij, N.F., 1992. Silicon cantilevers and tips for scanning force microscopy. *Sensors and Actuators A: Physical*, *34*(3), pp.193-200.

[16] Fasching, R.J., Tao, Y. and Prinz, F.B., 2005. Cantilever tip probe arrays for simultaneous SECM and AFM analysis. *Sensors and actuators B: Chemical*, *108*(1-2), pp.964-972.

[17] Villanueva, G., Plaza, J.A., Sánchez-Amores, A., Bausells, J., Martínez, E., Samitier, J. and Errachid, A., 2006. Deep reactive ion etching and focused ion beam combination for nanotip fabrication. *Materials Science and Engineering: C*, *26*(2-3), pp.164-168.

[18] Villanueva, G., Plaza, J.A., Sanchez, A., Zinoviev, K., Perez-Murano, F. and Bausells, J., 2007. DRIE based novel technique for AFM probes fabrication. *Microelectronic engineering*, *84*(5-8), pp.1132-1135.

[19] Akiyama, K., Eguchi, T., An, T., Fujikawa, Y., Yamada-Takamura, Y., Sakurai, T. and Hasegawa, Y., 2005. Development of a metal–tip cantilever for noncontact atomic force microscopy. *Review of scientific instruments*, *76*(3), p.033705.

[20] Cockins, L., Miyahara, Y., Stomp, R. and Grutter, P., 2007. High-aspect ratio metal tips attached to atomic force microscopy cantilevers with controlled angle, length, and radius for electrostatic force microscopy. *Review of Scientific Instruments*, *78*(11), p.113706.

[21] Fu, Y., Zhou, W., Lim, L.E., Du, C., Luo, X., Dong, X., Shi, H. and Wang, C., 2006. Geometrical characterization issues of plasmonic nanostructures with depth-tuned grooves for beam shaping. *Optical Engineering*, *45*(10), p.108001.

[22] Matsui, S., 1997. Nanostructure fabrication using electron beam and its application to nanometer devices. *Proceedings of the IEEE*, *85*(4), pp.629-643.

[23] van Kouwen, L., Botman, A. and Hagen, C.W., 2009. Focused electron-beam-induced deposition of 3 nm dots in a scanning electron microscope. *Nano letters*, *9*(5), pp.2149-2152.

[24] Van Dorp, W.F., Hagen, C.W., Crozier, P.A. and Kruit, P., 2008. Growth behavior near the ultimate resolution of nanometer-scale focused electron beam-induced deposition. *Nanotechnology*, *19*(22), p.225305.

[25] Randolph, S.J., Fowlkes, J.D. and Rack, P.D., 2006. Focused, nanoscale electron-beam-induced deposition and etching. *Critical reviews in solid state and materials sciences*, *31*(3), pp.55-89.

[26] Nanda, G., van Veldhoven, E., Maas, D., Sadeghian, H. and Alkemade, P.F., 2015. Helium ion beam induced growth of hammerhead AFM probes. *Journal of Vacuum Science & Technology B, Nanotechnology and Microelectronics: Materials, Processing, Measurement, and Phenomena*, *33*(6), p.06F503.

[27] Wang, X., Li, Q., Xie, J., Jin, Z., Wang, J., Li, Y., Jiang, K. and Fan, S., 2009. Fabrication of ultralong and electrically uniform single-walled carbon nanotubes on clean substrates. *Nano letters*, *9*(9), pp.3137-3141.

[28] Torres-Dias, A.C., Cerqueira, T.F., Cui, W., Marques, M.A., Botti, S., Machon, D., Hartmann, M.A., Sun, Y., Dunstan, D.J. and San-Miguel, A., 2017. From mesoscale to nanoscale mechanics in single-wall carbon nanotubes. *Carbon*, *123*, pp.145-150.

[29] Dai, H., Hafner, J.H., Rinzler, A.G., Colbert, D.T. and Smalley, R.E., 1996. Nanotubes as nanoprobes in scanning probe microscopy. *Nature*, *384*(6605), p.147.

[30] Hall, A., Matthews, W.G., Superfine, R., Falvo, M.R. and Washburn, S., 2003. Simple and efficient method for carbon nanotube attachment to scanning probes and other substrates. *Applied physics letters*, *82*(15), pp.2506-2508.

[31] Nguyen, C.V., Stevens, R.M., Barber, J., Han, J., Meyyappan, M., Sanchez, M.I., Larson, C. and Hinsberg, W.D., 2002. Carbon nanotube scanning probe for profiling of deep-ultraviolet and 193 nm photoresist patterns. *Applied Physics Letters*, *81*(5), pp.901-903.

[32] Tang, J., Yang, G., Zhang, Q., Parhat, A., Maynor, B., Liu, J., Qin, L.C. and Zhou, O., 2005. Rapid and reproducible fabrication of carbon nanotube AFM probes by dielectrophoresis. *Nano letters*, *5*(1), pp.11-14.

[33] Larsen, T., Moloni, K., Flack, F., Eriksson, M.A., Lagally, M.G. and Black, C.T., 2002. Comparison of wear characteristics of etched-silicon and carbon nanotube atomic-force microscopy probes. *Applied physics letters*, *80*(11), pp.1996-1998.

[34] Dey, R., 2015. Nanofabrication and its application in atomic force microscopy (AFM).

[35] *https://microchemicals.com/*

[36] Kayes, B.M., Atwater, H.A. and Lewis, N.S., 2005. Comparison of the device physics principles of planar and radial p-n junction nanorod solar cells. *Journal of applied physics*, *97*(11), p.114302.

[37] Singh, N., Agarwal, A., Bera, L.K., Liow, T.Y., Yang, R., Rustagi, S.C., Tung, C.H., Kumar, R., Lo, G.Q., Balasubramanian, N. and Kwong, D.L., 2006. High-performance fully depleted silicon nanowire (diameter/spl les/5 nm) gate-all-around CMOS devices. *IEEE Electron Device Letters*, *27*(5), pp.383-386.

[38] Sainiemi, L., Keskinen, H., Aromaa, M., Luosujärvi, L., Grigoras, K., Kotiaho, T., Mäkelä, J.M. and Franssila, S., 2007. Rapid fabrication of high aspect ratio silicon nanopillars for chemical analysis. *Nanotechnology*, *18*(50), p.505303.

[39] Welch, C.C., Goodyear, A.L., Wahlbrink, T., Lemme, M.C. and Mollenhauer, T., 2006. Silicon etch process options for micro-and nanotechnology using inductively coupled plasmas. *Microelectronic Engineering*, *83*(4-9), pp.1170-1173.

[40] Yu, Z., Gao, H., Wu, W., Ge, H. and Chou, S.Y., 2003. Fabrication of large area subwavelength antireflection structures on Si using trilayer resist nanoimprint lithography and liftoff. *Journal of Vacuum Science & Technology B: Microelectronics and Nanometer Structures Processing, Measurement, and Phenomena*, *21*(6), pp.2874-2877.

[41] Saffih, F., Con, C., Alshammari, A., Yavuz, M. and Cui, B., 2014. Fabrication of silicon nanostructures with large taper angle by reactive ion etching. *Journal of Vacuum Science & Technology B, Nanotechnology and Microelectronics: Materials, Processing, Measurement, and Phenomena*, *32*(6), p.06FI04.

[42] Ayari-Kanoun, A., Aydinoglu, F., Cui, B. and Saffih, F., 2016. Silicon nanostructures with very large negatively tapered profile by inductively coupled plasma-RIE. *Journal of Vacuum Science & Technology B, Nanotechnology and Microelectronics: Materials, Processing, Measurement, and Phenomena*, *34*(6), p.06KD01.

[43] Susarrey-Arce, A., Marín, Á.G., Schlautmann, S., Lefferts, L., Gardeniers, J.G. and van Houselt, A., 2012. One-step sculpting of silicon microstructures from pillars to needles for water and oil repelling surfaces. *Journal of micromechanics and microengineering*, *23*(2), p.025004.

[44] Dahlen, G., Osborn, M., Okulan, N., Foreman, W., Chand, A. and Foucher, J., 2005. Tip characterization and surface reconstruction of complex structures with critical dimension atomic force microscopy. *Journal of Vacuum Science & Technology B: Microelectronics and Nanometer Structures Processing, Measurement, and Phenomena*, *23*(6), pp.2297-2303.

[45] Walavalkar, S., Latawiec, P. and Scherer, A., 2013. Coulomb blockade in vertical, bandgap engineered silicon nanopillars. *Applied Physics Letters*, *102*(18), p.183101.

[46] Zheng, S., Dey, R.K., Aydinoglu, F. and Cui, B., 2016. Mixture of ZEP and PMMA with varying ratios for tunable sensitivity as a lift-off resist with controllable undercut. *Journal of Vacuum Science & Technology B, Nanotechnology and Microelectronics: Materials, Processing, Measurement, and Phenomena*, *34*(6), p.06K603.

[47] Liu, Z., Wu, Y., Harteneck, B. and Olynick, D., 2012. Super-selective cryogenic etching for sub-10 nm features. *Nanotechnology*, *24*(1), p.015305.

[48] De Boer, M.J., Gardeniers, J.G., Jansen, H.V., Smulders, E., Gilde, M.J., Roelofs, G., Sasserath, J.N. and Elwenspoek, M., 2002. Guidelines for etching silicon MEMS structures using fluorine

high-density plasmas at cryogenic temperatures. *Journal of microelectromechanical systems*, *11*(4), pp.385-401.

[49] Jiang, F., Keating, A., Martyniuk, M., Prasad, K., Faraone, L. and Dell, J.M., 2012. Characterization of low-temperature bulk micromachining of silicon using an SF6/O2 inductively coupled plasma. *Journal of Micromechanics and Microengineering*, *22*(9), p.095005.

[50] Min, J.H., Lee, G.R., Lee, J.K., Moon, S.H. and Kim, C.K., 2004. Dependences of bottom and sidewall etch rates on bias voltage and source power during the etching of poly-Si and fluorocarbon polymer using SF 6, C 4 F 8, and O 2 plasmas. *Journal of Vacuum Science & Technology B: Microelectronics and Nanometer Structures Processing, Measurement, and Phenomena*, *22*(3), pp.893-901.

[51] Blauw, M.A., Zijlstra, T. and Van der Drift, E., 2001. Balancing the etching and passivation in time-multiplexed deep dry etching of silicon. *Journal of Vacuum Science & Technology B: Microelectronics and Nanometer Structures Processing, Measurement, and Phenomena*, *19*(6), pp.2930-2934.

[52] Ouyang, Z., Ruzic, D.N., Kiehlbauch, M., Schrinsky, A. and Torek, K., 2014. Etching mechanism of the single-step through-silicon-via dry etch using SF6/C4F8 chemistry. *Journal of Vacuum Science & Technology A: Vacuum, Surfaces, and Films*, *32*(4), p.041306.

[53] Aydinoglu, F., Saffih, F., Dey, R.K. and Cui, B., 2017. Chromium oxide as a hard mask material better than metallic chromium. *Journal of Vacuum Science & Technology B, Nanotechnology and Microelectronics: Materials, Processing, Measurement, and Phenomena*, *35*(6), p.06GB01.

[54] Rangelow, I.W., 2003. Critical tasks in high aspect ratio silicon dry etching for microelectromechanical systems. *Journal of Vacuum Science & Technology A: Vacuum, Surfaces, and Films*, *21*(4), pp.1550-1562.

[55] Henry, M.D., Walavalkar, S., Homyk, A. and Scherer, A., 2009. Alumina etch masks for fabrication of high-aspect-ratio silicon micropillars and nanopillars. *Nanotechnology*, *20*(25), p.255305.

[56] Liu, Z., Gu, X., Hwu, J., Sassolini, S. and Olynick, D.L., 2014. Low-temperature plasma etching of high aspect-ratio densely packed 15 to sub-10 nm silicon features derived from PS-PDMS block copolymer patterns. *Nanotechnology*, *25*(28), p.285301.

[57] Abbas, A.S., Alqarni, S., Shokouhi, B.B., Yavuz, M. and Cui, B., 2014. Water soluble and metal-containing electron beam resist poly (sodium 4-styrenesulfonate). *Materials Research Express*, *1*(4), p.045102.

[58] Zhang, J., Cao, K., Wang, X.S. and Cui, B., 2015. Metal-carbonyl organometallic polymers, PFpP, as resists for high-resolution positive and negative electron beam lithography. *Chemical Communications*, *51*(99), pp.17592-17595.

[59] Con, C., Zhang, J. and Cui, B., 2014. Nanofabrication of high aspect ratio structures using an evaporated resist containing metal. *Nanotechnology*, *25*(17), p.175301.

[60] Yamazaki, T., Suzuki, Y. and Nakata, H., 1980. Gas plasma etching of ion implanted chromium films. *Journal of Vacuum Science and Technology*, *17*(6), pp.1348-1350.

[61] Nakata, H., Nishioka, K. and Abe, H., 1980. Plasma etching characteristics of chromium film and its novel etching mode. *Journal of Vacuum Science and Technology*, *17*(6), pp.1351-1357.

[62] Abe, H., Nishioka, K., Tamura, S. and Nishimoto, A., 1976. Microfabrication of anti-reflective chromium mask by gas plasma. *Japanese Journal of Applied Physics*, *15*(S1), p.25.

[63] Bell, G. and Spierer, H., 1990, June. Plasma etching of chrome masks using PBS resist. In *Optical/Laser Microlithography III* (Vol. 1264, pp. 446-452). International Society for Optics and Photonics.

[64] Mulloni, A., Seichter, H. and Schmalstieg, D., 2011, August. Handheld augmented reality indoor navigation with activity-based instructions. In *Proceedings of the 13th international conference on human computer interaction with mobile devices and services* (pp. 211-220). ACM.

[65] Tonotani, J., Ohmi, S.I. and Iwai, H., 2005. Dry etching of Cr2O3/Cr stacked film during resist ashing by oxygen plasma. *Japanese journal of applied physics*, *44*(1R), p.114.

[66] Tsai, J.W., Huang, C.Y., Tai, Y.H., Cheng, H.C., Su, F.C., Luo, F.C. and Tuan, H.C., 1997. Reducing threshold voltage shifts in amorphous silicon thin film transistors by hydrogenating the gate nitride prior to amorphous silicon deposition. *Applied physics letters*, *71*(9), pp.1237-1239.

[67] Chiang, C.S., Chen, C.Y., Kanicki, J. and Takechi, K., 1998. Investigation of intrinsic channel characteristics of hydrogenated amorphous silicon thin-film transistors by gated-four-probe structure. *Applied physics letters*, *72*(22), pp.2874-2876.

[68] Oguchi, K., Sanui, K., Ogata, N., Takahashi, Y. and Nakada, T., 1990. Relationship between electron sensitivity and chemical structures of polymers as electron beam resist. VII: Electron sensitivity of vinyl polymers containing pendant 1, 3-dioxolan groups. *Polymer Engineering & Science*, *30*(8), pp.449-452.

[69] Dey, R.K. and Cui, B., 2013. Effect of molecular weight distribution on e-beam exposure properties of polystyrene. *Nanotechnology*, *24*(24), p.245302.

[70] Bruce, R.L., Engelmann, S., Lin, T., Kwon, T., Phaneuf, R.J., Oehrlein, G.S., Long, B.K., Willson, C.G., Végh, J.J., Nest, D. and Graves, D.B., 2009. Study of ion and vacuum ultraviolet-induced effects on styrene-and ester-based polymers exposed to argon plasma. *Journal of Vacuum Science & Technology B: Microelectronics and Nanometer Structures Processing, Measurement, and Phenomena*, *27*(3), pp.1142-1155.

[71] Koshelev, K., Ali Mohammad, M., Fito, T., Westra, K.L., Dew, S.K. and Stepanova, M., 2011. Comparison between ZEP and PMMA resists for nanoscale electron beam lithography experimentally and by numerical modeling. *Journal of Vacuum Science & Technology B, Nanotechnology and Microelectronics: Materials, Processing, Measurement, and Phenomena*, *29*(6), p.06F306.

[72] Nishida, T., Notomi, M., Iga, R. and Tamamura, T., 1992. Quantum wire fabrication by e-beam elithography using high-resolution and high-sensitivity e-beam resist ZEP-520. *Japanese journal of applied physics*, *31*(12S), p.4508.

[73] Wu, B., 2006. Photomask plasma etching: A review. *Journal of Vacuum Science & Technology B: Microelectronics and Nanometer Structures Processing, Measurement, and Phenomena*, *24*(1), pp.1-15.

[74] Hossain, M.N., Justice, J., Lovera, P., McCarthy, B., O'Riordan, A. and Corbett, B., 2014. High aspect ratio nano-fabrication of photonic crystal structures on glass wafers using chrome as hard mask. *Nanotechnology*, *25*(35), p.355301.

[75] https://www.nanoworld.com/pointprobe-seiko-instruments-super-sharp-silicon-afm-tip-sss-seih

[76] Marcus, R.B., Ravi, T.S., Gmitter, T., Chin, K., Liu, D., Orvis, W.J., Ciarlo, D.R., Hunt, C.E. and Trujillo, J., 1990. Formation of silicon tips with< 1 nm radius. *Applied Physics Letters*, *56*(3), pp.236-238.

[77] Aydinoglu, F., Yamada, H., Dey, R.K. and Cui, B., 2017. Grafted Polystyrene Monolayer Brush as Both Negative and Positive Tone Electron Beam Resist. *Langmuir*, *33*(20), pp.4981-4985.

[78] Yeo, B.S., Stadler, J., Schmid, T., Zenobi, R. and Zhang, W., 2009. Tip-enhanced Raman Spectroscopy–Its status, challenges and future directions. *Chemical Physics Letters*, *472*(1-3), pp.1-13.

[79] Consales, M., Ricciardi, A., Crescitelli, A., Esposito, E., Cutolo, A. and Cusano, A., 2012. Lab-on-fiber technology: toward multifunctional optical nanoprobes. *ACS nano*, *6*(4), pp.3163-3170.

[80] King, G.M., Schürmann, G., Branton, D. and Golovchenko, J.A., 2005. Nanometer patterning with ice. *Nano letters*, *5*(6), pp.1157-1160.

[81] Han, A., Kuan, A., Golovchenko, J. and Branton, D., 2012. Nanopatterning on nonplanar and fragile substrates with ice resists. *Nano letters*, *12*(2), pp.1018-1021.

[82] Zhang, J., Con, C. and Cui, B., 2014. Electron beam lithography on irregular surfaces using an evaporated resist. *ACS nano*, *8*(4), pp.3483-3489.

[83] Linden, J., Thanner, C., Schaaf, B., Wolff, S., Lägel, B. and Oesterschulze, E., 2011. Spray coating of PMMA for pattern transfer via electron beam lithography on surfaces with high topography. *Microelectronic Engineering*, *88*(8), pp.2030-2032.

[84] Yamazaki, K. and Yamaguchi, H., 2010. Resist coating on vertical side faces using conventional spin coating for creating three-dimensional nanostructures in semiconductors. *Applied physics express*, *3*(10), p.106501.

[85] Yamazaki, K. and Yamaguchi, H., 2012. Electron beam lithography on vertical side faces of micrometer-order Si block. *Journal of Vacuum Science & Technology B, Nanotechnology and Microelectronics: Materials, Processing, Measurement, and Phenomena*, *30*(4), p.041601.

[86] Zhou, H., Chong, B.K., Stopford, P., Mills, G., Midha, A., Donaldson, L. and Weaver, J.M.R., 2000. Lithographically defined nano and micro sensors using “float coating” of resist and electron beam lithography. *Journal of Vacuum Science & Technology B: Microelectronics and Nanometer Structures Processing, Measurement, and Phenomena*, *18*(6), pp.3594-3599.

[87] Glass, R., Arnold, M., Bluemmel, J., Kueller, A., Möller, M. and Spatz, J.P., 2003. Micro-nanostructured interfaces fabricated by the use of inorganic block copolymer micellar monolayers as negative resist for electron-beam lithography. *Advanced Functional Materials*, *13*(7), pp.569-575.

[88] Li, Z., Gu, Y., Wang, L., Ge, H., Wu, W., Xia, Q., Yuan, C., Chen, Y., Cui, B. and Williams, R.S., 2009. Hybrid nanoimprint− soft lithography with sub-15 nm resolution. *Nano letters*, *9*(6), pp.2306-2310.

[89] Scheerlinck, S., Taillaert, D., Van Thourhout, D. and Baets, R., 2008. Flexible metal grating based optical fiber probe for photonic integrated circuits. *Applied Physics Letters*, *92*(3), p.031104.

[90] Viheriala, J., Niemi, T., Kontio, J., Rytkonen, T. and Pessa, M., 2007. Fabrication of surface reliefs on facets of singlemode optical fibres using nanoimprint lithography. *Electronics letters*, *43*(3), pp.150-151.

[91] Lipomi, D.J., Martinez, R.V., Kats, M.A., Kang, S.H., Kim, P., Aizenberg, J., Capasso, F. and Whitesides, G.M., 2010. Patterning the tips of optical fibers with metallic nanostructures using nanoskiving. *Nano letters*, *11*(2), pp.632-636.

[92] Smythe, E.J., Dickey, M.D., Whitesides, G.M. and Capasso, F., 2008. A technique to transfer metallic nanoscale patterns to small and non-planar surfaces. *ACS nano*, *3*(1), pp.59-65.

[93] Li, L., Bayn, I., Lu, M., Nam, C.Y., Schröder, T., Stein, A., Harris, N.C. and Englund, D., 2015. Nanofabrication on unconventional substrates using transferred hard masks. *Scientific reports*, *5*, p.7802.

[94] Lercel, M.J., Rooks, M., Tiberio, R.C., Craighead, H.G., Sheen, C.W., Parikh, A.N. and Allara, D.L., 1995. Pattern transfer of electron beam modified self-assembled monolayers for high-resolution lithography. *Journal of Vacuum Science & Technology B: Microelectronics and Nanometer Structures Processing, Measurement, and Phenomena*, *13*(3), pp.1139-1143.

[95] Tiberio, R.C., Craighead, H.G., Lercel, M., Lau, T., Sheen, C.W. and Allara, D.L., 1993. Self-assembled monolayer electron beam resist on GaAs. *Applied physics letters*, *62*(5), pp.476-478.

[96] Ogawa, K., Mino, N., Tamura, H. and Hatada, M., 1990. Reactions of chemically adsorbed monolayers induced by electron beam irradiation in active gas atmosphere and applications for the preparation of multilayers. *Langmuir*, *6*(4), pp.851-856.

[97] Edmondson, S., Osborne, V.L. and Huck, W.T., 2004. Polymer brushes via surface-initiated polymerizations. *Chemical society reviews*, *33*(1), pp.14-22.

[98] Ulman, A., 1996. Formation and structure of self-assembled monolayers. *Chemical reviews*, *96*(4), pp.1533-1554.

[99] Miyake, T., Tanii, T., Kato, K., Hosaka, T., Kanari, Y., Sonobe, H. and Ohdomari, I., 2006. Nanopatterning of hydroxy-terminated self-assembled monolayer taking advantage of terminal group modification. *Chemical physics letters*, *426*(4-6), pp.361-364.

[100] Strulson, M.K., Johnson, D.M. and Maurer, J.A., 2012. Increased stability of glycol-terminated self-assembled monolayers for long-term patterned cell culture. *Langmuir*, *28*(9), pp.4318-4324.

[101] Flynn, N.T., Tran, T.N.T., Cima, M.J. and Langer, R., 2003. Long-term stability of self-assembled monolayers in biological media. *Langmuir, 19*(26), pp.10909-10915.

[102] Yamada, H., Aydinoglu, F., Liu, Y., Dey, R.K. and Cui, B., 2017. Single Layer Surface-Grafted PMMA as a Negative-Tone e-Beam Resist. *Langmuir*, *33*(48), pp.13790-13796.

[103] Dey, R.K., Aydinoglu, F. and Cui, B., 2017. Electron Beam Lithography on Irregular Surface Using Grafted PMMA Monolayer as Resist. *Advanced Materials Interfaces*, *4*(3), p.1600780.

[104] Ma, S., Con, C., Yavuz, M. and Cui, B., 2011. Polystyrene negative resist for high-resolution electron beam lithography. *Nanoscale research letters*, *6*(1), p.446.

[105] Austin, M.D., Zhang, W., Ge, H., Wasserman, D., Lyon, S.A. and Chou, S.Y., 2005. 6 nm half-pitch lines and 0.04 µm2 static random access memory patterns by nanoimprint lithography. *Nanotechnology*, *16*(8), p.1058.

[106] Manako, S., Fujita, J.I., Ochiai, Y., Nomura, E. and Matsui, S., 1997. Nanometer-scale patterning of polystyrene resists in low-voltage electron beam lithography. *Japanese journal of applied physics*, *36*(12S), p.7773.

[107] Keddie, J.L. and Jones, R.A.L., 1995. Glass Transition Behavior in Ultra-Thin Polystyrene Films. *Israel journal of chemistry*, *35*(1), pp.21-26.

[108] Draper, J., Luzinov, I., Ionov, L., Minko, S., Varshney, S.K. and Stamm, M., 2003. Wettability and morphology of a mixed polymer brush prepared by simultaneous polymer addition. *POLYMER PREPRINTS-AMERICA*-, *44*(1), pp.570-571.

[109] Luzinov, I., Julthongpiput, D., Malz, H., Pionteck, J. and Tsukruk, V.V., 2000. Polystyrene layers grafted to epoxy-modified silicon surfaces. *Macromolecules*, *33*(3), pp.1043-1048.

[110] Levchik, G.F., Si, K., Levchik, S.V., Camino, G. and Wilkie, C.A., 1999. The correlation between cross-linking and thermal stability: Cross-linked polystyrenes and polymethacrylates. *Polymer degradation and stability*, *65*(3), pp.395-403.

[111] Con, C., Abbas, A.S., Yavuz, M. and Cui, B., 2013. Dry thermal development of negative electron beam resist polystyrene. *Adv. Nano Res*, *1*, pp.105-109.

[112] Broers, A.N., Harper, J.M.E. and Molzen, W.W., 1978. 250-Å linewidths with PMMA electron resist. *Applied Physics Letters*, *33*(5), pp.392-394.

[113] Hild, R., David, C., Müller, H.U., Völkel, B., Kayser, D.R. and Grunze, M., 1998. Formation and characterization of self-assembled monolayers of octadecyltrimethoxysilane on chromium: Application in low-energy electron lithography. *Langmuir*, *14*(2), pp.342-346.